DEVELOPMENT OF AN ALL-FIBER HOMODYNE QUADRATURE LASER INTERFEROMETER FOR INTEGRATION INTO A COMPACT THERMAL ACTUATOR

by

Cecil D. Hastings, Jr. (D.J.)

A thesis submitted to the faculty of
The University of North Carolina at Charlotte
in partial fulfillment of the requirements
for the degree of Master of Science in
Mechanical Engineering

Charlotte

2021

Approved by:

_____
Dr. Stuart T. Smith

_____
Dr. Russell Keanini

_____
Dr. Jimmie Miller

_____
Dr. Joshua Tarbutton

©2021
D.J. Hastings
ALL RIGHTS RESERVED

ABSTRACT

D.J. HASTINGS. Development of an all-fiber homodyne quadrature laser interferometer for integration into a compact thermal actuator
(Under the direction of DR. STUART T. SMITH)

This thesis presents the development of an all-fiber homodyne quadrature laser interferometer (HQLI) for integration into a newly designed, compact thermal actuator capable of driving loads up to 1000 N in high temperature environments.

The source of the HQLI consists of a commercially available, 635 nm, fiber coupled, single-mode laser diode. Major components of the optical system comprise a two input by two output fiber splitter, two dielectric mirrors, and a photodetector. The two output arms of the HQLI are called the device-under-test (DUT) arm and the Modulation (MOD) arm. The DUT arm will ultimately be integrated into the thermal actuator. The MOD arm is the controlling arm for the quadrature detection. These two arms are the only locations where light from inside the fiber is exposed to the ambient environment. The MOD arm uses a dielectric mirror opposite the standard, single mode FC fiber ferrule. The MOD arm has accommodations for feedback control via a capacitance gage to reduce drift in the modulation displacement of the modulation mirror. The DUT arm was tested with the same single mode fiber type and dielectric mirror as the MOD arm. Future work to install the DUT arm into the thermal actuator will be completed using the same flat polish for the end-face of the fiber. The output arm of the HQLI is called the photodetector (PD) arm and is connected to a commercially available photodetector and photodetector amplifier. The output of the photodetector amplifier is fed to signal conditioning stages to increase the contrast of the fringes. A lock-in amplifier has been employed to determine the first (1f) and second (2f) frequency harmonics of the fringes that form the basis of quadrature detection.

The HQLI has been tested to maintain fringe stability over a time period of thirty minutes, a displacement resolution of 30 nm, and an operating range of 3.0 mm at standard laboratory conditions.

The novel feature of this thesis is the design of a thermal actuator with methods for implementation and control, and materials of construction that can withstand harsh operating environments, mainly temperatures higher than a standard laboratory environment. The thermal actuator has been tested with an applied axial load of 1000 N for an extended period of time without mechanical failure. Open loop time responses have been measured for varying pulse width modulations of a 120 W power supply to a high power induction heater.

ACKNOWLEDGEMENTS

I would like to thank my advisor, Dr. Stuart T. Smith, for his immense support and guidance over the years. Secondly, I would like to send a very special thank you to my wife Jennifer for her unwavering support. Additionally, I would like to thank US Conec, Ltd. for their financial and scheduling support that made this possible. Lastly, there are a number of individuals who helped make this work possible, including Chunjie Fan, Kumar Arumugam, Steve Howard, and Justin Gunter.

TABLE OF CONTENTS

LIST OF FIGURES

LIST OF TABLES

LIST OF EQUATIONS

LIST OF ABBREVIATIONS

AC	Alternating current
APC	Angled polished connector
CAD	Computer aided design
DAQ	Data acquisition device
dB	Decibel
DC	Direct current
DCV	Directional control valve
DSP	Digital signal processing
DUT	Device under test side of interferometer
FC	Ferrule, ceramic, screw on type
FEA	Finite element analysis
GRIN	Gradient index lens
GUI	Graphical user interface
HPF	High pass filter
HQLI	Homodyne quadrature laser interferometer
Hrs	Hours
Hz	Hertz
I1f	Amplitude of the first harmonic
I2f	Amplitude of the second harmonic
kHz	Kilohertz
LPF	Low pass filter
MEMS	Micro-electromechanical system
min	Minutes
MOD	Modulation arm side of interferometer
MPa	Megapascal
mm	Millimeter
mrad	Milliradian
mV	Millivolt

mW	Milliwatt
N	Newton
nm	Nanometer
PC	Flat polished connector
PD	Photodetector
pF	Picofarad
PI	Proportional integral control
PID	Proportional integral derivative control
PWM	Pulse width modulation
PZT	Lead zirconium titanate ceramic piezo electric transducer
RMS	Root mean square
ROI	Region of interest
RTD	Resistance temperature detector
s	Seconds
sfpm	Surface feet per minute
SM	Single mode
TM	Turning mirror
TPI	Threads per inch
USB	Universal serial bus
V	Voltage
VDC	Voltage, Direct Current
VFL	Visual fault locator
V_{pk-pk}	Voltage, peak to peak
µA	Microamp
µm	Micrometer
µW	Microwatt
ZVS	Zero volt switching
1f	First harmonic
2f	Second harmonic

CHAPTER 1: BACKGROUND AND LITERATURE REVIEW

As stated in the summary, this thesis is a study of the design of a compact thermal actuator with an integrated displacement sensor, a homodyne quadrature laser interferometer. An overview of the background literature is presented below.

1.1. ALL-FIBER INTERFEROMETERS

There has been significant research in all-fiber interferometers that utilize frequency modulated coherent laser sources, equidistant fiber lengths, polarization controls, and fiber stretchers. These types of systems have historically been plagued by a host of issues, including: the requirement for identical length fibers, poor operational stability of the system, limited operating range, sensitivity to environmental impacts, and the utilization of infrared laser sources that are invisible to the naked eye (Nowakowski), (Elezov), (Liu). In its simplest form, the all-fiber interferometer is comprised of a laser source, a fiber splitter, at least one mirror and one photodetector. Several modulation techniques are described for generating the required quadrature for displacement metrology. Those techniques include modulating the laser source, utilizing a fiber stretcher to vary the length of the reference arm, and phase modulation at the fiber end face.

To date, there has been no improvement to the requirement for the constraint of the two mirror arms of the interferometer to be the same length. All research to date outlines that constraint. Multiple attempts at improving the operational stability have been attempted with the longest time period being 200 s (Elezov). (Nowakowski) shows stability control for up to 66 hrs using a Fabry-Perot etalon based optical spectrum analyzer that communicates with the laser source in a pseudo-PID control loop inside of a temperature controlled chamber that is maintained within ±0.01°C.

To address the operating range issue, (Liu) implemented a gradient index lens (GRIN) and mentions needing a longer working distance although not specifically mentioning the extents of the working distance. (Nowakowski) mentions having cavity separations of a few micrometers up to tens of millimeters using a bare fiber end face.

Considering the desired application of the compact thermal actuator, several obstacles need to be addressed. First, because of the relatively low bandwidth of thermal actuators of centimeter dimensions (typically measured in Hz), the operational stability of the system needs to be improved from the demonstrated 200 s. Fan et al. (C. H. Fan, Design and control of a thermal actuation system) demonstrate the step responses of the first-generation thermal actuator system with steady-state response settling times up to 60 s per step. Second, there is interest in utilizing a visible wavelength laser in the system for operator safety and resolution improvements. Third, with the end use application being inside an elevated temperature operating environment, there is a need to be able to vary the length of the fibers between the DUT arm and the MOD arm. The sensitivities outlined in the literature suggest the MOD arm needs to have enhanced environmental control for successful operation and thus complicating the design of a system to operate in a hostile environment.

A theoretical model of the operation of this instrument is being developed with other members of the instrumentation group. Relevant theory has been extracted and is presented in this thesis.

1.2. THERMAL ACTUATORS

There is substantial interest in micrometer size micro-electrical mechanical system (MEMS) thermal actuators in the current literature. Some of this literature discusses larger scale thermal actuators, but there is even less discussion to date on centimeter to millimeter size thermal

actuators. Additionally, there is minimal discussion of thermal actuators operating in hostile environments, such as an environment with elevated temperatures. (Lawall) mentions using a 106 mm length of thin-walled aluminum tubing as a thermal actuator for driving a mirror in a custom interferometer application. Little detail is given on the construction and operational details of this design other than the use of a 240 W power supply that is used for heating the insulated copper wire that surrounds the aluminum tube. (Synder) discusses a notch type flexure preloaded by the tension of a fixed length of wire, 127 μm diameter by 2.54 cm length, as the thermal actuator. As current is passed through the wire, the wire increases in both diameter and length. The change in length results in an angular rotation in the flexure. The current required for 1 mrad of rotation is 130 mA, which results in a power dissipation of 33 mW, and a temperature increase of 25 K. Interestingly, in this work the resistance is measured as an indirect measure of the rotation of the notch hinge.

In a general discussion comparing different actuator methods, (Huber) describes actuators as the mechanical driving force and motion for a variety of tasks in response to a control signal. (Huber) discusses different types of actuators and their relative merits to one another (independent of scale and frequency). Scaling effects are discussed in the review by Smith and Suegling (Smith).

Piezoelectric actuators exhibit strain when an external electric field is applied (Huber). These actuators, typically exhibiting a maximum strain of around 0.1%, have a range of displacements dependent upon their physical size, are capable of supporting loads producing compressive stresses up to around 200 MPa, and can operate with a variety of input voltages and frequencies. However, they also have a number of drawbacks. Because of their high losses, a major drawback of piezoelectric actuators is the required heat dissipation if the actuator is to

provide substantial mechanical work or power. In order for the actuator to maintain its piezoelectric behavior, the operating temperature needs to be limited to below the Curie temperature (usually well below). Any heat that is generated, exposed to, or in the vicinity of the actuator, can cause malfunction. In a study of several manufacturers, the safe maximum operating temperature for these actuators is approximately 65°C. Another drawback to these actuators is hysteresis in the motion of the actuator, typically in the range of 15-30% maximum, depending on manufacturer, construction, and operating details.

Hydraulic and pneumatic actuators use compressed fluid flow as the mechanism for both force and displacement. Hydraulic actuators often utilize oil as the compressed fluid. They behave with high stiffness (low compressibility), relatively high speed, and can achieve high levels of strain, depending on the actuator design and the operating pressure of the fluid. Due to materials used in their construction, connection hardware and hoses, and safety concerns over high pressure fluid leakages, operation in hostile, high temperature environments is not usually recommended, although there are some exceptions to this (notably in aerospace and military applications). Pneumatic actuators utilize compressed air as the fluid for the generation of force and motion. These actuators are also plagued by the same issues as the hydraulic actuators, but their stiffness is much lower given the compressibility of air and the lower operating pressures. (Beater) describes the repeatability of pneumatic actuators at a range of ± 0.05 mm in the best case, to ± 0.13 mm in a typical application. Typical pneumatic actuators are machined with an aluminum housing, a round internal bore, and a steel shaft with several seals providing protection against fluid leakage. With high levels of temperature change, the dimensional changes in these different materials can result in fluid leakage (seal failure) and performance degradation.

Thermal actuators use temperature change as their relative mechanism to provide force and motion. They can exhibit higher strain than piezoelectric materials, are relatively simple devices, and can operate in a range of environments. In its simplest form, a thermal actuator may consist of any piece of raw material with an appropriate heating method, recall the examples of (Lawall) and (Synder). The actuation strain of a thermal actuator is proportional to its coefficient of thermal expansion and the temperature change. If a high strain actuator is required, the raw material can be chosen such that the coefficient of the thermal expansion is maximized, thus requiring lower temperature inputs. If a high stress and high strain actuator is required, such as the actuator described in this thesis, then an additional consideration of the modulus of elasticity of the material must be included in the analysis. In these types of applications, metals are typically the material of choice. Metals offer distinct benefits such as the coefficient of thermal expansion is relatively constant over large temperature ranges and the material is capable of high stress / high strain applications without failure.

Due to the lack of available literature for the implementation and operation of thermal actuators, significant work has been conducted prior to the writing of this thesis in Dr. Smith's laboratory to address these issues in a first-generation prototype. Results from these works are summarized in the following papers:

- (C. H. Fan, Aspects of Design and Performance of a thermally actuated linear translation stage)
- (C. H. Fan, Design and Performance of a Thermal Actuator Driving a Preloaded Linear Translation Stage)
- (C. H. Fan, Design and control of a thermal actuation system)
- (C. S. Fan)

1.3. THERMAL ACTUATOR DESIGN AND IMPLEMENTATION CONSIDERATIONS, LESSONS FROM PREVIOUS STUDIES

Regarding operational details of thermal actuators, several areas of discussion are quite relevant – types of heating, cooling, drive electronics, and controller types. In (C. H. Fan, Design and Performance of a Thermal Actuator Driving a Preloaded Linear Translation Stage), the authors describe several different methods of heating thermal actuators and their relative merits and drawbacks. Some of the methods are resistive heating (or i^2R heating), conduction, and radiation. For the first-generation prototype and the application in this thesis, resistive heating in the form of eddy current induction heating has been employed. Circulating water flowing through the coil of the first prototype provided overheating protection for the induction coil during operation. The journal paper provides operational details for these coils, as well as prior work completed by (Dodd, Analytical Solutions to Eddy Current Probe Coil Problems).

The heating for the thermal actuator in the first generation prototype was provided via an induction coil operated using a closed loop PI controller providing feedback to a PWM conversion board. The PWM conversion board provided the control signal to a zero-volt switching circuit (ZVS). This ZVS was connected to large, high wattage power supplies that provided the necessary operational current to the induction coils. The induction coils then applied a fluctuating magnetic field that induced eddy currents inside the thermal actuator. For the actuator to have a fast retract response, a cooling system was required. Due to this and other requirements, the thermal actuator has progressed from a solid piece of metal to a machined cylindrical tube.

The cooling scheme was designed to operate with a mixture of compressed air and a water mist that would flow through the inside of the thermal actuator when the system was in cooling

mode. The heating mode was operated with a PI controller, and the new cooling system was controlled via a separate bang-bang, or digital on / digital off type controller. The modes of heating and cooling are described in (C. H. Fan, Design and Performance of a Thermal Actuator Driving a Preloaded Linear Translation Stage).

Experimental results of this initial prototype revealed differing thermal responses in the heating and cooling processes. Due to the different controller strategies and heating / cooling responses, different thermal time constants were observed in the heating process than was observed in the cooling process. As is discussed in the paper, the time constant for the heating process was limited by the available power of the power supplies, the power limitations of the ZVS circuit, and the maximum temperature of the induction coil. The time constant for the cooling process was limited by the overall bulk temperature of the cooling media. When the actuator was operating at high strain (high temperature), the cooling process was efficient due to a large temperature differential between the cooling fluid and the actuator temperature. However, when operating at low strain, the cooling process became inefficient due to the low temperature differential. Results of this testing are outlined in both (C. H. Fan, Design and control of a thermal actuation system) and (C. H. Fan, Design and Performance of a Thermal Actuator Driving a Preloaded Linear Translation Stage).

The last area of development was the drive electronics. In the first-generation prototype, a commercial off the shelf ZVS switching circuit was purchased and integrated with a Cytron DC motor driver and two 120 W power supplies, totaling 240 W of input power. During testing with the 240 W power supply, limitations were observed in the slew rate of the step responses at the high strain actuations. Due to these slew rate limitations, the power supplies were increased to a total of 480 W of input power. At this point, the actuator exhibited improved performance, but

the ZVS circuits began to fail. Closer examination of the circuits revealed failure of the power MOSFETs and the zener diodes in the drive circuits. A new drive circuit was designed to increase the power handling capabilities of the ZVS and subsequently tested. The data presented in (C. H. Fan, Design and Performance of a Thermal Actuator Driving a Preloaded Linear Translation Stage) show the results of this upgrade. There was an improvement in the heating slew rate, but the controller needed additional help with improvements to the cooling side to reduce the steady state error.

These lessons have resulted in a different actuator implementation and the improved drivers used in this project.

CHAPTER 2: DETAILS OF SUB-SYSTEM DESIGN

This chapter includes discussions concerning design details of both the HQLI and the compact thermal actuator.

2.1. HOMODYNE QUADRATURE LASER INTERFEROMETER

The HQLI consists of a commercially available, fiber coupled, single mode (SM), 635 nm laser diode as the optical source. Figure 1 shows the major optical components of the system, including a two input by two output SM fiber splitter, a dielectric mirror for the modulation (MOD) arm of the splitter, a dielectric mirror for the device under test (DUT) arm of the splitter, and a photodetector (PD).

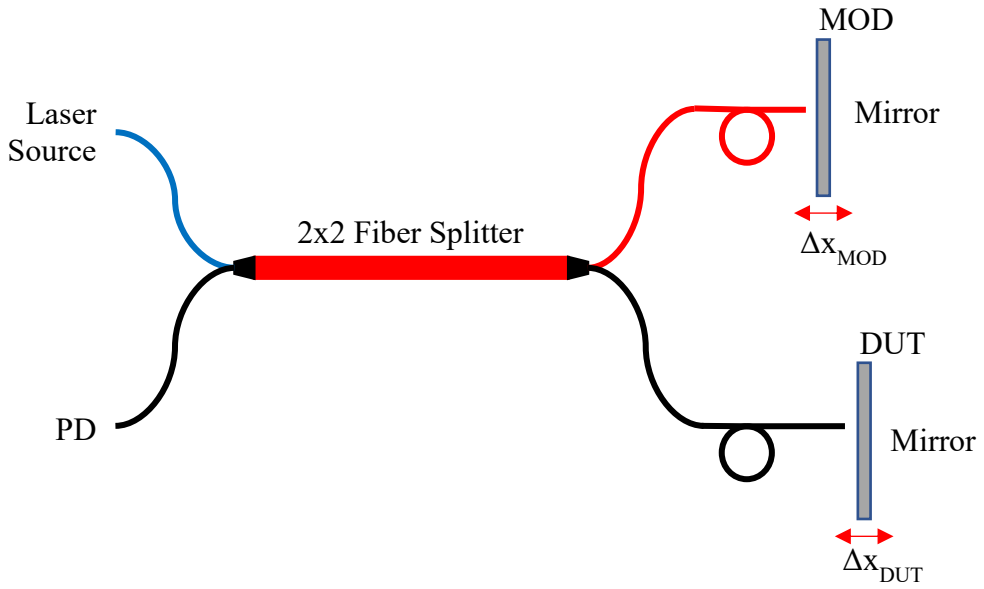

Figure 1. HQLI, schematic view

The output of the laser source is coupled to the fiber splitter via an FC/APC connection. Each of the two output arms of the fiber splitter divide the power from the laser source by half. 50% of the light travels to the MOD arm, experiences an index change at the end face of the fiber (n_{fiber} ~ 1.46147 and n_{air} ~ 1.000) and sends a primary modulation reflection, R_1 (~3.5%), back down the MOD arm. The remaining 96%, T_1, will travel to the mirror and be reflected back to the fiber.

Due to the end face of the fiber being a bare fiber, the beam exits the fiber at a divergence angle proportional to the numerical aperture of the fiber, ~0.1. Assuming the separation distance from the end face of the fiber to the mirror surface to be ~0.1 mm, ~5% of the 96% will couple back into the fiber (T_2). Due to the intensity of R_1 and T_2, only those reflections are considered in the evaluation. Additional reflections are created in the Fabry-Perot cavity but their intensities are not considered in this evaluation.

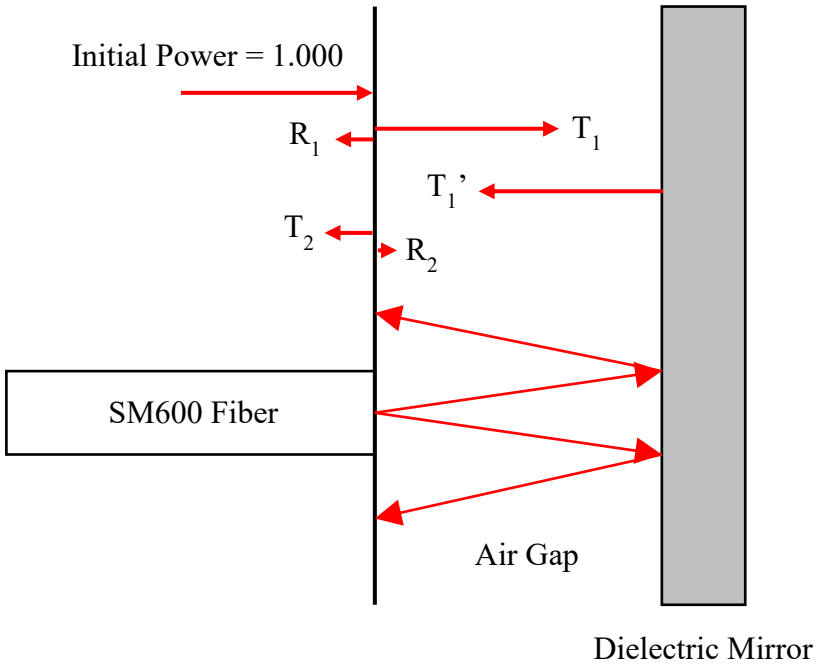

Figure 2. Reflection schematic of MOD arm

The same process happens on the DUT arm of the splitter and the R_1 and T_2 signals from both the DUT arm and the MOD arm are sent back down the splitter. Those two signals are divided by half and are sent back to both the laser source and photodetector. Ideally, a fiber circulator or Faraday isolator would be installed to reduce the reflections traveling back to the laser source and causing potential instability. At the photodetector, the measured intensity is a DC value that is proportional to the mean square of the summation of all the input electric fields, R_1 and T_2

from both arms. There is also an AC component that is sitting on top of the DC offset. This AC part constitutes the fringes that contain the phase, quadrature, and displacement information.

In summation, for a specific power input from the laser diode, the corresponding expected measured power at the photodetector is approximately 4%, given no losses at the fiber to fiber connections, no cross-talk losses in the splitter, and air gaps of 0.1 mm at both the MOD arm mirror and the DUT arm mirror. If the air gap is increased to 1.0 mm, the simulation results show the power at the photodetector is approximately 2% of the input power.

In addition, for the final design there should be additional discussion to the metrology loop differences between the MOD arm and the DUT arm due to the temperature differences that will be encountered when the DUT arm is subjected to the high temperature operating environment. See Section 5.1 for additional discussion.

2.1.1. MODELING THE COUPLING EFFICIENCY OF BARE FIBER

Gaussian beam propagation equations (Optics) were used to determine the laser beam's diameter as a function of the distance away from the end face of the fiber. Assuming the laser beam exiting the fiber follows a Gaussian profile, the intensity of the beam as a function of its radius can be determined from:

$$I(r) = I_0 e^{\left(\frac{-2r^2}{\omega(z)^2}\right)}$$ *Equation 1*

where:

I_0 = peak irradiance at the center of the beam,

r = radial distance from the axis of the beam,

z = propagation distance from the end of the fiber, and

$\omega(z)$ = radius of the laser beam where the irradiance is $1 \cdot e^{-2}$ (~13.5%) of I_0.

And using the total power measurement, Equation 1 becomes

$$I(r) = \frac{2P}{\pi\omega(z)^2} e^{\left(\frac{-2r^2}{\omega(z)^2}\right)}$$ *Equation 2*

where:

P = total power of the laser beam,

r = radial distance from the axis of the beam,

z = propagation distance from the end of the fiber, and

$\omega(z)$ = radius of the laser beam along the propagation axis.

As the beam exits the fiber, the mode field diameter is approximately the beam waist. As the beam propagates through space in the z-direction, the beam will diverge at an angle given by:

$$\theta = \frac{\lambda}{\pi\omega_0}$$ *Equation 3*

where:

θ = divergence angle of the laser beam in the far field,

λ = wavelength of the laser beam, and

ω_0 = radius of the laser beam waist.

The change in the beam radius as a function of z-axis propagation is given by (Optics):

$$\omega(z) = \omega_0 \sqrt{1 + \left(\frac{\lambda z}{\pi\omega_0^2}\right)^2}$$ *Equation 4*

where:

$\omega(z)$ = radius of the laser beam along the propagation axis,

ω_0 = radius of the laser beam waist,

λ = wavelength of the laser beam, and

z = propagation distance from the end of the fiber.

The Rayleigh range is defined as the value of z where the cross-sectional area of the beam has increased by a factor of two.

$$Z_R = \frac{\pi \omega_0^2}{\lambda}$$ *Equation 5*

where:

Z_R = Rayleigh range of the Gaussian beam,

λ = wavelength of the laser beam, and

ω_0 = beam waist of the laser beam.

Substituting Equation 5 into Equation 4,

$$\omega(z) = \omega_0 \sqrt{1 + \left(\frac{z}{Z_R}\right)^2}$$ *Equation 6*

where:

$\omega(z)$ = radius of the laser beam along the propagation axis,

ω_0 = radius of the laser beam waist,

z = propagation distance from the end of the fiber, and

Z_R = Rayleigh range of the Gaussian beam.

The coupling efficiency of two beams can be modeled by

$$T = \left(\frac{2\omega_1\omega_2}{\omega_1^2 + \omega_2^2}\right)^2$$ *Equation 7*

where:

T = coupling efficiency between two laser beams,

ω_1 = radius of the first laser beam, and

ω_2 = radius of the second laser beam.

The beam diameter was calculated as a function of propagation distance for a set of distances from 0 mm up to 6 mm. The far extent is the approximate maximum distance of the fiber end face from the DUT arm mirror. The coupling efficiency was then determined using Equation 7.

Figure 3 below shows the results of those calculations. As the beam propagation distances are increased, the corresponding coupling efficiency drops off quickly around 0.5 mm.

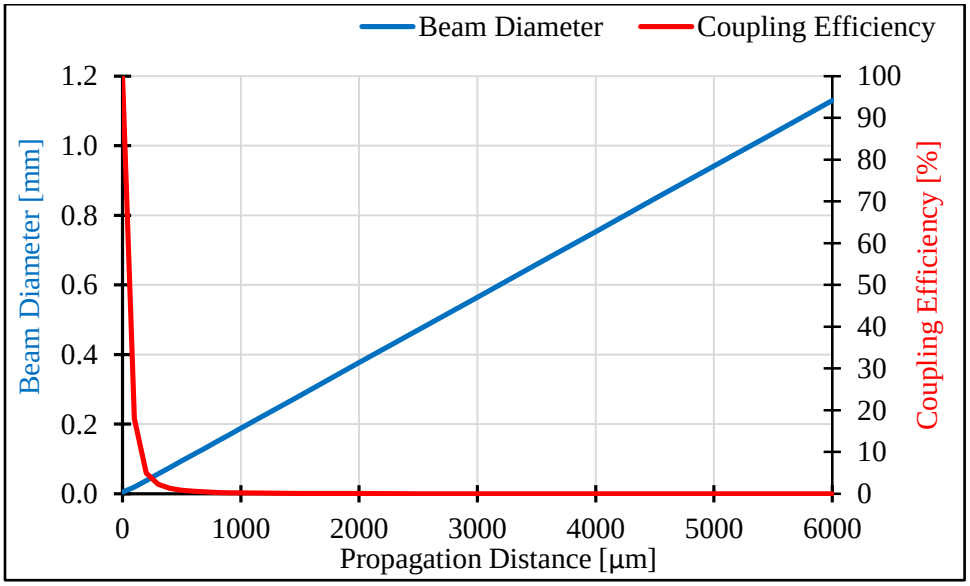

Figure 3. Beam diameter and coupling efficiency as a function of propagation distance

A very basic Zemax model was created to validate the approximate operating range of the bare fiber compared to the above Gaussian beam calculations. A perfect mirror was placed at a specified distance from the fiber end face. No accommodations were made for rotational mis-alignments, only axial translation. Two distances were evaluated, z_1 = 0.1 mm and z_2 = 1.0 mm. Using SM600 fiber, the mode field diameter of the fiber is 4.3 µm, based on the operating wavelength of 635 nm (Thorlabs). The resulting beam diameter returning back to the fiber from each initial displacement is 0.027 mm for z_1 and 0.266 mm for z_2. These resulting beam diameters correspond to a signal attenuation of 13 dB for z_1 and 34 dB for z_2. The results of the Zemax calculation were compared to the results in the Gaussian beam propagation calculations and they were in agreement with each other (at an average deviation of 0.1%) up to a distance of 1.0 mm. After 1.0 mm, Zemax would not evaluate.

2.1.2. MOD ARM MIRROR

While most of the optical system can be housed in an enclosure, the HQLI has two areas open to the environment, the MOD arm and the DUT arm. At the MOD arm, the end face of the SM fiber is located approximately 2.5 mm away from the dielectric mirror. In this space, the end face of the fiber is open to the environment, and has a primary reflection from the first index change at the end face of the fiber and the air gap, and subsequent Fabry-Perot type reflection from the mirror opposite the end face of the fiber, see Figure 2 above. Figure 4 below shows the location of the air gap in the MOD arm flexure.

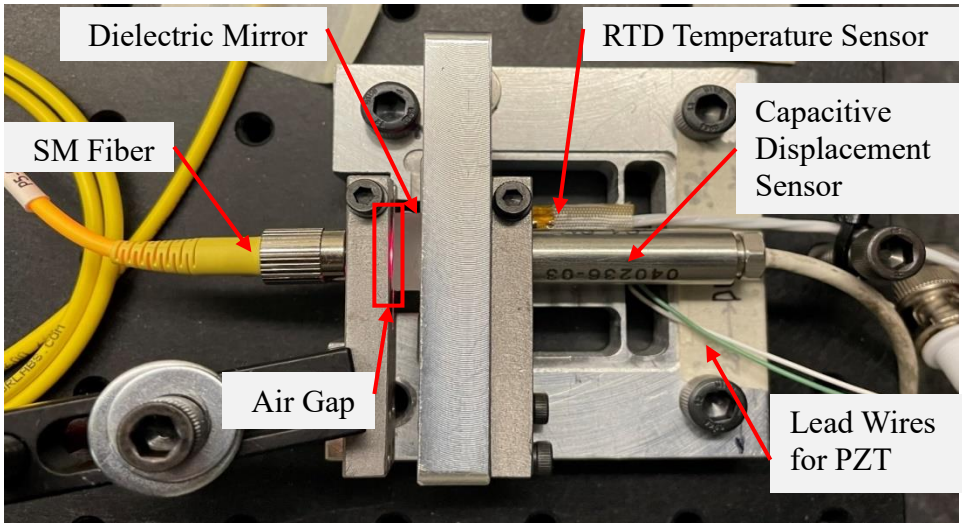

Figure 4. Location of air gap in MOD arm of HQLI

The MOD arm mirror is modulated at a frequency higher than the anticipated operating bandwidth for displacement measurement and an amplitude that is smaller than the optical wavelength. A modulation signal, typically a low amplitude, high frequency sine wave (MOD arm), is superimposed onto the displacement signal (DUT arm) for subsequent use in quadrature detection via a lock-in amplifier. A simplified image of the modulation signal (y2, red trace), a fringe signal (y1, blue trace), and combination of the two (y1+y2, green trace) is shown below in Figure 5. The green trace, y_1 and y_2, is the intended profile of the signal that will be entering the photodetector.

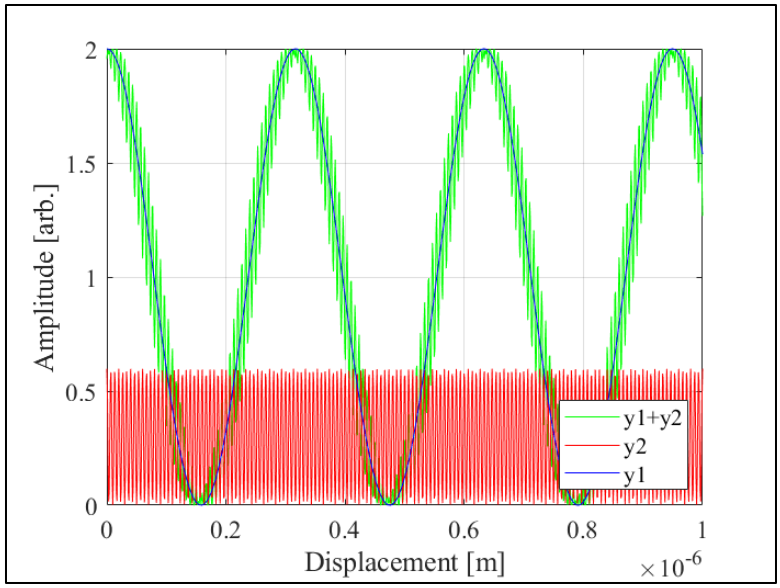

Figure 5. Carrier frequency superimposed on sample fringe signal as a function of displacement

The signal *y1 + y2* in Figure 5 can be calculated from:

$$I = I_0\left[C_0 + \cos\left(\frac{2\pi}{\lambda}2x_D + \frac{2\pi}{\lambda}2x_M\right)\right]$$

Equation 8

DC offset — DUT Arm — MOD Arm

where:

I = Amplitude of the intensity,

I_0C_0 = DC offset of the amplitude of the intensity,

λ = wavelength of the laser,

X_D = displacement of the DUT mirror, and

X_M =displacement of the MOD mirror.

From Equation 8, three components are visible, the DC offset of the intensity, the signal due to the DUT arm mirror, and the signal due to the MOD arm mirror. The frequency of the DUT arm is much lower than the frequency of the MOD arm and will be assumed to be a constant value.

Let:

$$X_M = A_M \sin(\omega_M t)$$ *Equation 9*

where:

X_M =displacement of the MOD mirror,

A_M =amplitude of the displacement of the MOD mirror,

ω_M =angular frequency of the MOD mirror, and

t = time.

Therefore, inserting Equation 9 into Equation 8:

$$I = I_0\left\{C_0 + \cos\left[\frac{2\pi}{\lambda}2X_D + \frac{2\pi}{\lambda}2[A_M \cos(\omega_M t)]\right]\right\}$$ *Equation 10*

Equation 10 is used to model the signals shown above in Figure 5.

Then, let $k^* = \frac{4\pi}{\lambda}$ and $\phi = k^* X_D$:

$$I = I_0\{C_0 + \cos[\phi + k^* A_M \cos(\omega_M t)]\}$$ *Equation 11*

Then, let $\delta = k^* A_M$:

$$I = I_0\{C_0 + \cos[\phi + \delta \cos(\omega_M t)]\}$$ *Equation 12*

Using the trigonometric identity $\cos(\alpha + \beta) = \cos\alpha \cos\beta - \sin\alpha \sin\beta$ in Equation 12, $\alpha = \phi$ and $\beta = \delta \cos(\omega_M t)$.

$$\cos(\alpha + \beta) = \cos\phi \cos[\delta \cos(\omega_m t)] - \sin\phi \sin[\delta \cos(\omega_M t)]$$ *Equation 13*

Thus, the Jacobi-Anger expansion will be used in the $\cos[\delta \cos(\omega_m t)]$ and the $\sin[\delta \cos(\omega_M t)]$.

The Jacobi-Anger expansion for the cosine-cosine term is:

$$\cos(z \cos\theta) = J_0(z) + 2\sum_{n=1}^{\infty}(-1)^n J_{2n}(z) \cos(2n\theta)$$ *Equation 14*

where:

$J_0(z)$ = Bessel function of the first kind where 0 is the primary harmonic,

z = position of interest in the Bessel function, and

n = harmonic of interest in the Bessel function.

Following Equation 14, $z = \delta$ and $\theta = \omega_M t$. Thus, the cosine-cosine term in Equation 13 applied to Equation 14 is:

$$\cos(z\cos\theta) = J_0(\delta) + 2\sum_{n=1}^{\infty}(-1)^n J_{2n}(\delta)\cos[2n\omega_M t] \qquad \textit{Equation 15}$$

Then the Jacobi-Anger Expansion for the sine-cosine term is:

$$\sin(z\cos\theta) = -2\sum_{n=1}^{\infty}(-1)^n J_{2n-1}(z)\cos[(2n-1)\theta] \qquad \textit{Equation 16}$$

Same as before, $z = \delta$ and $\theta = \omega_M t$. Thus, the sine-cosine term in Equation 13 applied to Equation 16 is:

$$\sin(z\cos\theta) = -2\sum_{n=1}^{\infty}(-1)^n J_{2n-1}(\delta)\cos[(2n-1)\omega_M t] \qquad \textit{Equation 17}$$

Now, substitute Equation 15 and Equation 17 into Equation 13:

$$\cos(\alpha+\beta) = \cos\phi\left[J_0(\delta) + 2\sum_{n=1}^{\infty}(-1)^n J_{2n}(\delta)\cos(2n\omega_M t)\right] - sin\phi\left[(-2)\sum_{n=1}^{\infty}(-1)^n J_{2n-1}(\delta)\cos[(2n-1)\omega_M t]\right] \qquad \textit{Equation 18}$$

Equation 18 needs to be substituted back into Equation 12:

$$\mathrm{I} = I_0\left\{C_0 + \cos\phi\left[J_0(\delta) + 2\sum_{n=1}^{\infty}(-1)^n J_{2n}(\delta)\cos(2n\omega_M t)\right] - sin\phi\left[(-2)\sum_{n=1}^{\infty}(-1)^n J_{2n-1}(\delta)\cos[(2n-1)\omega_M t]\right]\right\}$$

Equation 19

In Equation 19, only $n = 1$ will be used due to the requirement of using the first and second harmonics for quadrature detection. In addition, $\cos\phi$ and $\sin\phi$ are considered constants since their change is much lower than ω_M. The I_0C_0 and $J_0(\delta)$ are considered to be zero due to the utilization of a high pass filter. Following these changes, Equation 19 simplifies to:

$$\mathrm{I} = I_0\{\cos\phi\,[2(-1)J_2(\delta)\cos(2\omega_M t)] - sin\phi[(-2)(-1)J_1(\delta)\cos(\omega_{Mt})]\}$$

Equation 20

Simplifying Equation 20:

$$\mathrm{I} = I_0\{\cos\phi\,[2J_2(\delta)\cos(2\omega_M t)] + sin\phi[2J_1(\delta)\cos(\omega_{Mt})]\}$$

Equation 21

Equation 21 now shows the amplitude of the 1f and 2f intensities. The 1f signal will be obtained in the $I_0 2J_1(\delta)$ and the 2f signal will be obtained in the $I_0 2J_2(\delta)$. Given the depth of modulation and the wavelength of the laser used in this thesis, the ratio of J_1 to J_2 is approximately 0.715. This difference in amplitude of the frequency harmonics is shown in the graph of the Bessel function, shown below in Figure 6. Inside the red box shows the amplitude of the J_1 solution (the red curve) and the J_2 solution (the yellow curve) at the modulation value for this thesis ($\delta \sim 3.0$). Two potential locations are outlined in green circles in Figure 6 where the amplitudes of the 1f and 2f harmonic signals are approximately equal. The leftmost potential solution of the two has the other harmonics at a lower value than the rightmost potential solution. In order to shift to

either of these locations, a change in the modulation depth (A_m) would be required. This is an area that will be studied in future works.

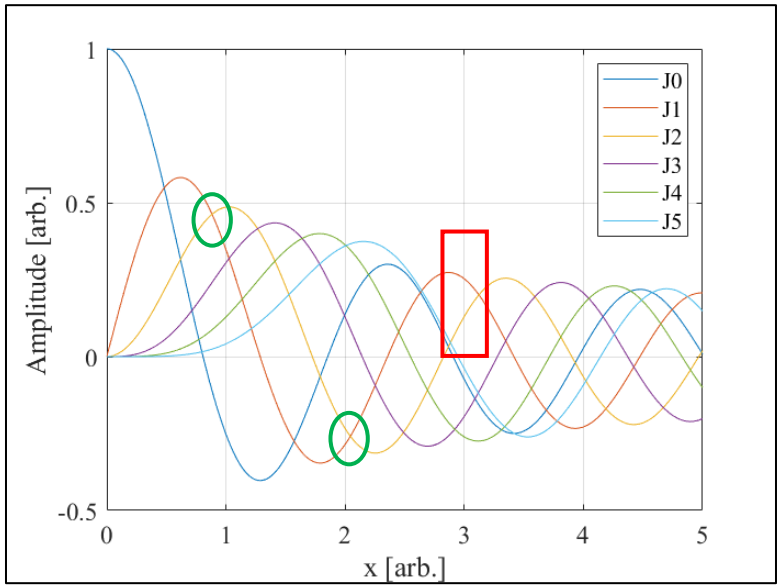

Figure 6. Bessel function of the first kind for the modulation depth and wavelength of the HQLI system

To further simplify Equation 21, now let $I1f_{in} = 2I_0J_1(\delta)$ and $I2f_{in} = 2I_0J_2(\delta)$.

$$\mathrm{I} = I_{1f\_in}\sin\phi\cos(\omega_M t) + I_{2f\_in}\cos\phi\cos(2\omega_M t) \qquad \textit{Equation 22}$$

The output of the two lock-in amplifiers after extracting the first and second harmonics is now:

$$I_{1f} = \frac{I_{1f\_in}}{\sqrt{2}}\sin\phi \qquad \textit{Equation 23}$$

$$I_{2f} = \frac{I_{2f\_in}}{\sqrt{2}}\cos\phi \qquad \textit{Equation 24}$$

Thus, the unequal amplitudes of I1f and I2f will result in an elliptical shape at the output of the lock-in amplifier when viewed as a Lissajous diagram, as shown in Figure 7 below. This shape will require some type of balancing to achieve a circular Lissajous for quadrature detection.

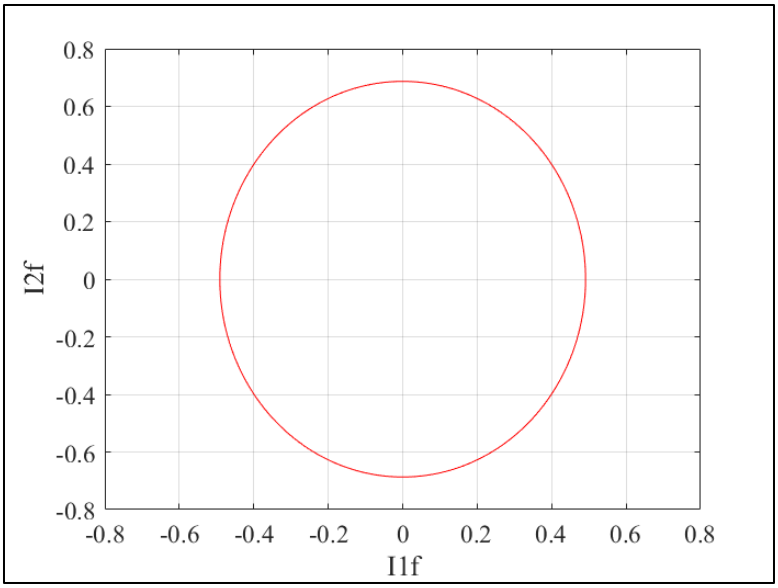

Figure 7. Ideal Lissajous diagram showing the I1f and I2f signals being unequal in amplitude

According to (Nowakowski), the corresponding depth of modulation (or amplitude of modulation) is desired to be as small as possible in cavities up to a thickness of a few millimeters to aid in faster system response. In (Nowakowski), wavelength modulation of the laser sources corresponds to a significant phase change for large cavity lengths (relative to the wavelength of the laser). (Nowakowski) used a wavelength modulation depth of 0.5 nm and frequency of 1.2 kHz. In this thesis, the laser wavelength was kept constant and a frequency modulation depth of 150 nm in the displacement of the MOD arm mirror at a frequency of 2.5 kHz was used.

2.1.3. QUADRATURE DETECTION

Quadrature detection for the HQLI is accomplished using a lock-in amplifier to remove the modulation frequency from the photodetector signal and determine the first (1f) and second (2f) harmonics of the remaining signal. The original signal from the photodetector is composed of an infinite number of individual harmonics, example shown below in Figure 8, of the modulation frequency such that $I = J_0 + J_1(\delta)\cos(\phi) + J_2(\delta)\cos(\phi) + \cdots$. The amplitude of

the harmonics has a dependency on the position of the DUT mirror where $\phi = \frac{4\pi}{\lambda} X_D$, i.e., the amplitudes of the harmonics are not constant values.

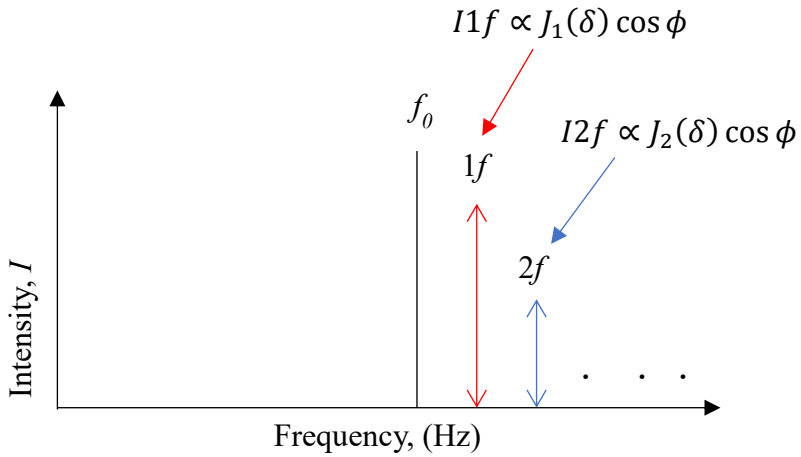

Figure 8. Harmonics generated by the lock-in amplifier

As mentioned earlier, the first (I1f) and second (I2f) harmonics are then balanced to achieve approximately the same output amplitude using the output sensitivity feature of the lock-in amplifier. The harmonics are then extracted from the lock-in and sent to the DAQ device via the lock-in amplifier's DAC and are then plotted against one another to create a Lissajous signal that shows the ninety-degree phase shift between the first and second harmonics, Figure 9.

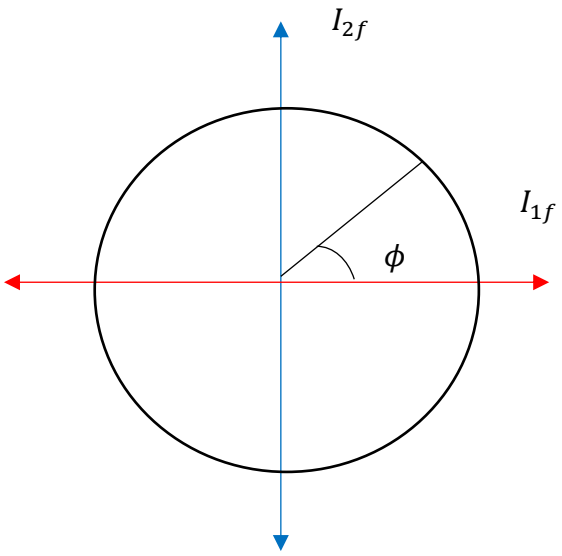

Figure 9. Ideal Lissajous figure of the I2f vs. I1f

Prior to phase unwrapping, the peak-to-valley amplitudes of the intensity are measured as a function of displacement. The intensity values are scaled (normalized) to span a range of ±1. Using these normalized intensities, the corresponding output equations to unwrap the phase are:

$$\phi = \tan 2^{-1}\left(\frac{I2f}{I1f}\right)$$ *Equation 25*

where:

ϕ = phase angle between the *I2f* and *I1f* signals,

I1f = amplitude of the first harmonic signal, and

I2f = amplitude of the second harmonic signal.

$$X_{wrap} = \frac{\lambda}{4\pi}\tan 2\left(\frac{I2f}{I1f}\right)$$ *Equation 26*

where:

X_{wrap} = the wrapped displacement value,

λ = wavelength of the laser source,

I1f = measured amplitude of the first harmonic signal, and

I2f = measured amplitude of the second harmonic signal.

In Equation 25 and Equation 26 above, the I1f and I2f are the signals after the signal conditioning electronics, not the original intensity measurement from the photodetector. Following Equation 26, the unwrapping of the displacement can be implemented to remove any of the 2π jumps in the data. The algorithm for unwrapping the phase is shown in Appendix 12. MATLAB® Program for Evaluating HQLI. In practice, the initial value and the second value of the wrapped displacement are first compared to one another. If the absolute value of the difference between the second value and the first value is above a threshold value, the difference is subtracted from an addition term (this addition term is zero at the beginning of the loop and updates on each loop iteration to be the previous loop iteration's value). The sum of the addition term and the second value now become the unwrapped phase. The unwrapped phase has the 2π discontinuities or jumps in the measurement data removed resulting in a smooth, continuous function.

2.1.4. SIGNAL TO NOISE, FRINGE CONTRAST, AND DISPLACEMENT RESOLUTION

The signal to noise (SN) ratio of a system is used to characterize the amplitude of a signal relative to the noise in that signal. The higher the SN ratio, the more signal fidelity. Consider the graphs shown in Figure 10 and Figure 11 that show normalized plots of the I1f and I2f signals as the DUT mirror is displaced. The blue dots are representative data points of the I1f and I2f signal from the lock-in amplifier. The red ellipse is representative of the magnitude of noise in that particular harmonic.

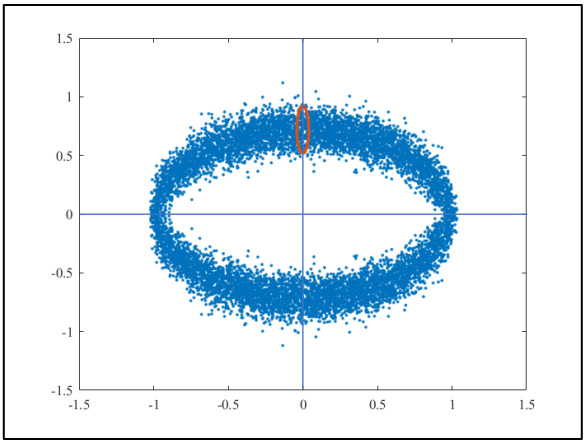

Figure 10. Lissajous signal with noise ellipse at I2f

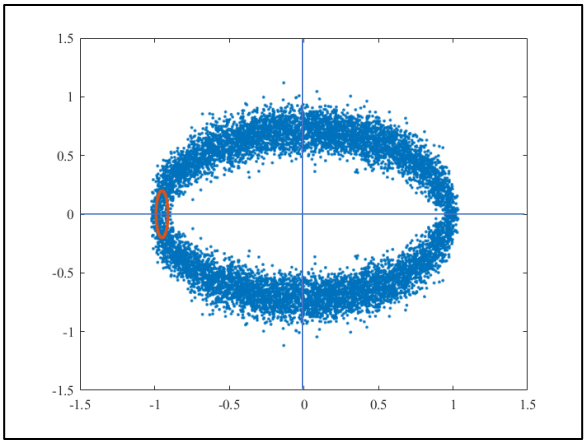

Figure 11. Lissajous signal with noise ellipse at I1f

For example, the major axis of the ellipse represents the noise in the I2f signal and the minor axis of the ellipse represents the noise in the I1f signal. If a mean line is drawn into the center of the blue dots, such as in Figure 12, this would be representative of the amplitude of the signal from the lock-in amplifiers for the I1f and I2f harmonics. From the diagram, it can be shown that two system performance indices need to be considered. First, the signal to noise of the I1f signal and second, the signal to noise of the I2f signal. Using Figure 12 and Figure 13, the signal amplitudes (S) and the corresponding noise amplitudes (N) are different for each case.

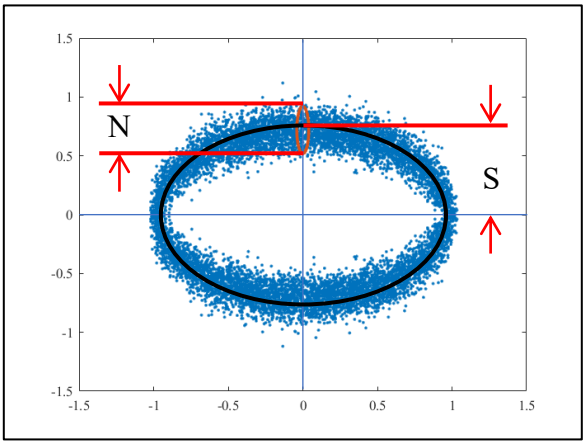

Figure 12. Lissajous signal with mean signal added, I2f

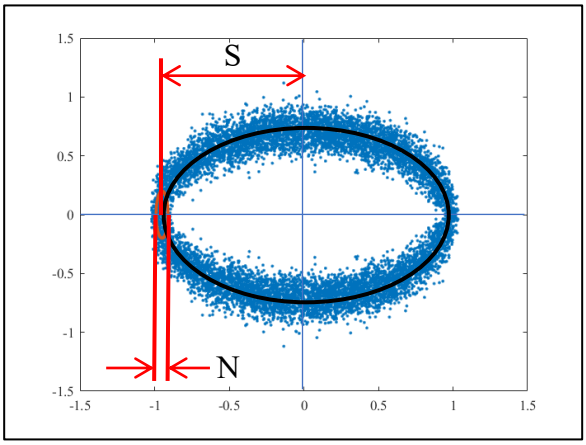

Figure 13. Lissajous signal with mean signal added, I1f

In the case of I2f, the amplitude of the signal can be much lower than the I1f's amplitude and the noise amplitude in the I2f is larger than the I1f's noise amplitude. In a case like this, attention should be given to improving the I2f signal such to increase the signal to noise. Following the

discussion, the minimum value of the signal to noise over a complete fringe measurement is reported as the signal to noise of the system, corresponding to the case illustrated in Figure 15 below.

(Ellis) mentions that fringe contrast, or visibility, is a measure of the interfering signal's range of intensity divided by its average intensity, a normalized value between zero and one. If a system has zero contrast, there is no data to be collected due to poor performance. If a system has a contrast of one, the ratio of the amplitudes is said to be in perfect fringe contrast. In the case of the HQLI, this can be equated to using the signal to noise ratio, described above. The signal, S, is the average amplitude of the measured signal. The noise, N, is the range of that measured signal at a given phase. Considering that contrast is scaled between zero and one; signal to noise is calculated such that a high value means the signal is much higher than the noise; a measure needs to be determined to scale the signal to noise between zero and one.

$$FC = 1 - \frac{1}{SN}$$ *Equation 27*

where:

FC = fringe contrast of the HQLI and

SN = signal to noise ratio of the HQLI.

Equation 27 above describes the fringe visibility such that a high value of the signal to noise will keep the fringe contrast close to one, suggesting close to perfect fringe contrast. In a case where there is a low signal to noise, the fringe contrast will approach zero (unusable). When describing the overall performance of the HQLI, the minimum fringe contrast value will be quoted.

The displacement resolution of the system is a measure of the smallest displacement the HQLI can determine given the system's signal and noise in both the I1f and I2f axes. Consider Figure 14 and Figure 15 below. The arc length of a circle of radius *R* subtended by a small angle

θ is given by $S = R\theta$. Using the terminology of the arc length and placing those terms into the figures, the relationship between the signal to noise and the corresponding arc length can be realized.

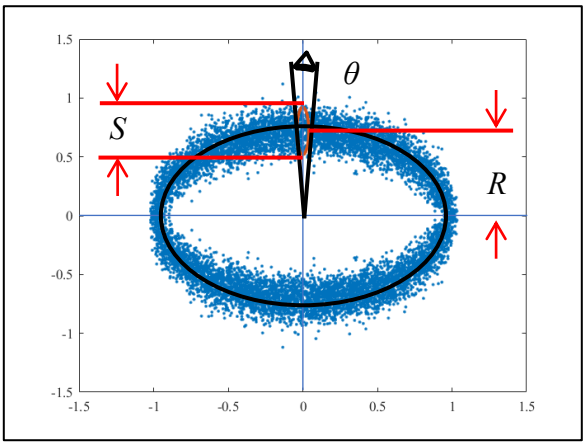

Figure 14. Lissajous signal with I2f small angle approximation

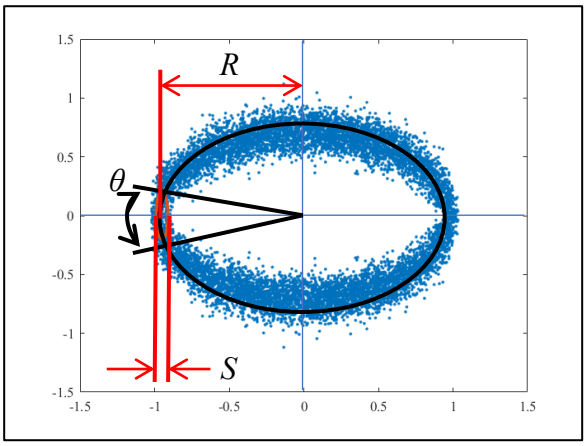

Figure 15. Lissajous signal with I1f small angle approximation

In small angles, the arc length *S* becomes *dS*, the angle θ becomes $d\theta$, and the radius of the circle remains *R*. Re-arranging the equation for small angles, $dS = Rd\theta$. Solving for the minimum resolvable angle, $d\theta = \frac{dS}{R}$. Using the signal to noise relationship, $d\theta \approx \frac{N}{S}$, where *N* equals the noise amplitude in the harmonic and *S* equals the signal amplitude in the harmonic. For small displacements,

$$dx = \frac{\lambda}{2\pi SN} \qquad \textit{Equation 28}$$

where:

dx = resolution of the interferometer,

λ = wavelength of the laser, and

SN = the minimum value of the I1f or I2f signal to noise ratio.

To summarize, the signal to noise ratio of the HQLI is an important parameter that can be used to determine the system's fringe contrast (Equation 27) and the interferometer displacement resolution (Equation 28).

2.2.THERMAL ACTUATOR

The compact thermal actuator is a millimeter scaled actuator that has overall dimensions of 12 mm x 12 mm x 43 mm, similar in size to a standard AA battery. The design below outlines key performance parameters such as a maximum displacement of 75 μm, a lifting force of 1000 N, induction heating for the heating process, standard compressed air for the cooling media, positional feedback via an integrated HQLI, and the ability to operate in harsh, high temperature environments.

The basic concept and theory of operation of the thermal actuator is very simple. The core mechanical design is simply a precisely machined cylindrical aluminum tube with a nominal outside diameter of 4 mm, inside diameter of 2 mm, and length of 27 mm. By heating and cooling this tube, high loads can be moved in both the expansion and contraction directions. Because of the simplicity in design and materials, this device can be operated in environments with harsh operating conditions, such as high temperature environments.

An overview of the thermal actuator is shown below in Figure 16. The main components are the induction coil that provides the heat input, the cooling pipes that remove the heat, the HQLI fiber and reflection rod that provide the displacement feedback, and the actual thermal actuator tube.

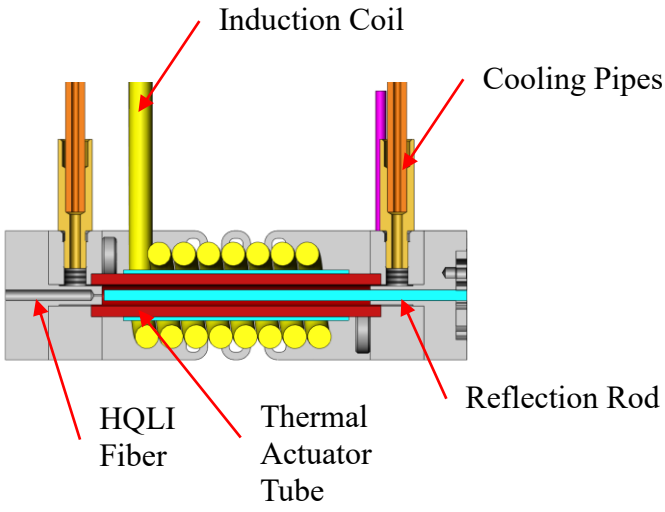

Figure 16. Overview of the compact thermal actuator

To evaluate the performance of the thermal actuator, a frame structure was built around the actuator that will support the high loads and provide necessary facility support to secure the different subsystems.

Referencing the HQLI section (Section 2.1) above, the HQLI fiber in Figure 16 is equivalent to the DUT fiber in Figure 1 and the reflection rod is equivalent to the DUT mirror in Figure 1. These two components comprise the implementation of the DUT side of the HQLI into the thermal actuator.

2.2.1. FRAME / SYSTEM APPARATUS

To begin, the overall outline of the thermal actuator system is shown below in Figure 17. For the remainder of this thesis, the color of the different sub-systems shown in Figure 17 are carried out:

- Compressed air cooling system is shown in purple.
- Electronic circuits are shown in green.
- Optical circuits and systems are shown in red.
- Water cooling circuits are shown in yellow.

- Mechanical displacements are shown in blue.

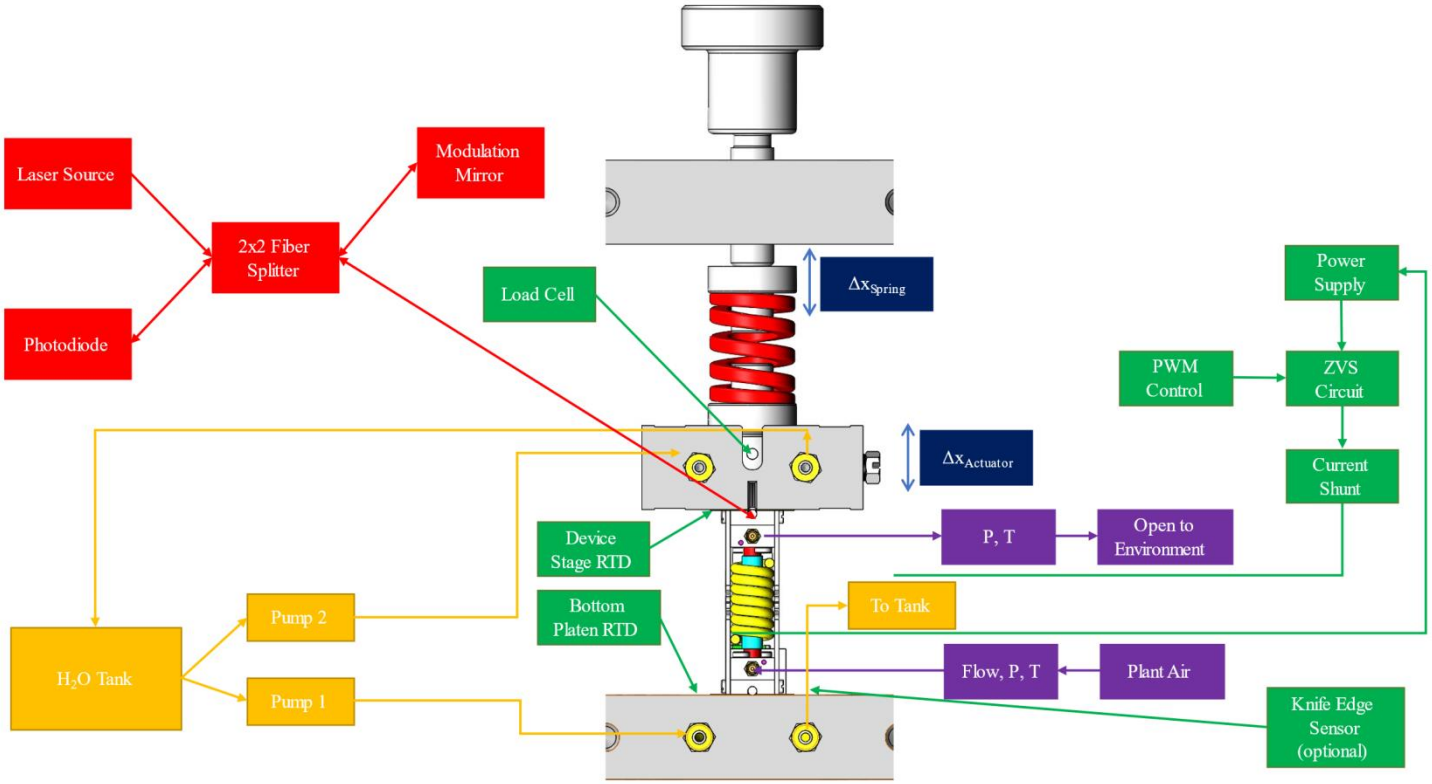

Figure 17. Block diagram of the supporting systems for the thermal actuator

The images in Figure 18 and Figure 19 below show the CAD design for the frame structure and a photograph of the actual implementation of the design respectively. Starting at the top of the system in these two figures, there is a screw handle on the top of the frame provides the ability to vary the magnitude of the preload by rotating the screw handle and displacing the compression spring. A compression spring sitting atop the device stage provides a preload force to the thermal actuator underneath. A load cell is placed between the compression spring and the thermal actuator to provide feedback for the applied load.

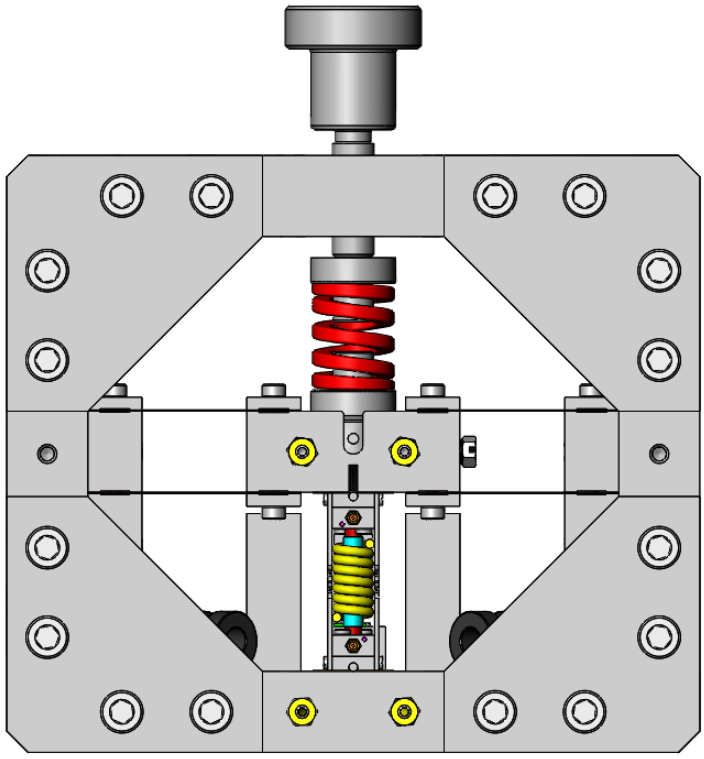

Figure 18. CAD model of frame structure

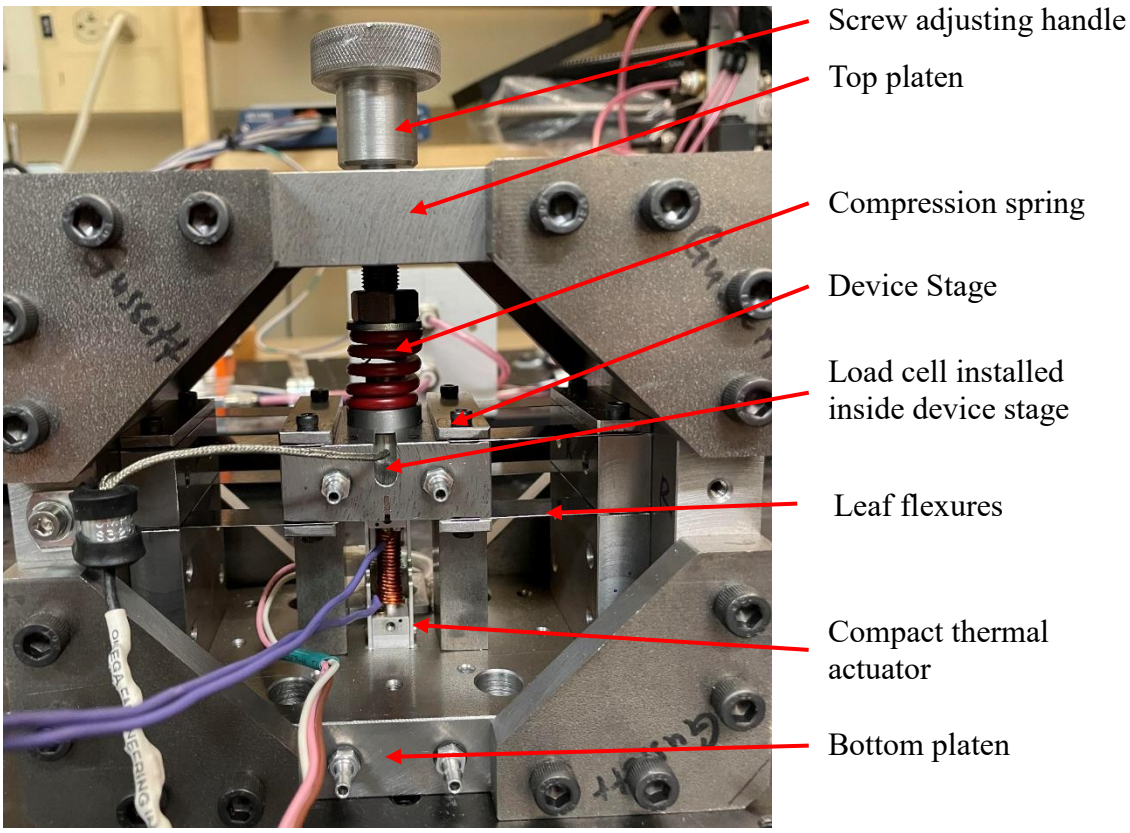

Figure 19. Implementation of the CAD design for the frame structure

Directly below the compression spring is the device stage. The device stage is the interface between the spring and the compact thermal actuator. Cooling water can flow through this plate if needed. Two RTDs (not shown in Figure 19) are mounted close to the compact thermal actuator to determine if there is any convective heat transfer from the compact thermal actuator to its surroundings. One RTD is mounted at the bottom of the thermal actuator on the bottom platen and a second RTD is mounted at the top of the thermal actuator on the device stage. In operation, it would not be desirable to have heat from the thermal actuator enter the device stage (or the bottom platen). The device stage could be considered to be a piece of apparatus the actuator is responsible for positioning.

The device stage is supported by leaf type flexure arms manufactured from blue tempered spring steel (McMaster Carr 9075K47, 1095 spring steel, hardness of Rockwell C50). These

arms, eight in total, provide low stiffness (1200 $N \cdot m^{-1}$ per arm) in the vertical direction and allow smooth, friction free travel for the compact thermal actuator. In the lateral direction, they provide a much higher stiffness due to the number of flexures present and the width versus the thickness of the flexures. Under the device stage are two steel blocks that protect the system in the event of a failure of the compact thermal actuator, i.e., they prevent overtravel if a collapse occurs. Between the over-travel stops is the compact thermal actuator. At the base of the compact thermal actuator is a second RTD that is to be used to measure any temperature change conducted to the surroundings.

2.2.2. MECHANICAL

One of the initial design constraints was that the system needed to be able to handle an applied load of 1000 N. With the compact thermal actuator being a simple aluminum tube with an outside diameter of 4 mm and inside diameter of 2 mm, FEA analysis of the actuator was completed to determine the maximum applied load. Results from Ansys show a maximum applied load of 4750 N with a safety factor of one (considering the yield strength of aluminum to be 503 MPa), well above the required 1000 N.

When considering the strain due to the temperature change of the actuator tube, the estimated strain in the actuator tube was calculated to be 0.0037 $\mu m \cdot \mu m^{-1}$ with a temperature increase of 160°C. This results in a maximum stress of approximately 260 MPa. Considering the yield strength of the 7075 aluminum, the safety factor was determined to be approximately 1.9 (considering the yield strength).

Adding fatigue of the actuator tube into the analysis, the above two design points were considered. The ultimate strength of the 7075 aluminum was used in the fatigue analysis (572 MPa). For a 10^3 cycle strength, the failure strength was calculated to be 429 MPa. For a 10^6

cycle strength, a failure strength of 123 MPa was calculated. Considering the results from the applied load (~110 MPa) and the thermal strain (~260 MPa), there does appear to be a failure life associated with the actuator, especially if full actuation lengths, or maximum displacements, are required. Results from these analyses are shown below in Table 1.

Table 1. Estimated safety factors for actuator tube based on loading conditions calculated at room temperature and maximum actuator temperature

Stress Condition (1000 N applied load)	Calculated Stress [MPa]	Static Load	10^3 Cycle Strength	10^6 Cycle Strength
		S_y = 503 MPa	S_f = 429 MPa	S_f = 123 MPa
Room Temperature	110	4.6	3.9	1.1
Maximum Actuator Temperature	260	1.9	1.7	0.5

To aid in handling of the actuator when assembled, a spring flexure was designed to provide a small amount of preload to the actuator. Figure 20 and Figure 21 below show the CAD model and the implementation of the design into the actuator. The spring flexure was designed to have an initial displacement of 0.1 mm, resulting in an applied load of 8 N to the actuator. FEA analysis of the design was performed to determine if a displacement of 0.3 mm (initial preload + actuator final position + elevated temperature amount) would result in failure of the spring. This 0.3 mm displacement results in an applied load of 20 N and a safety factor of 1.2, considering the yield strength of aluminum.

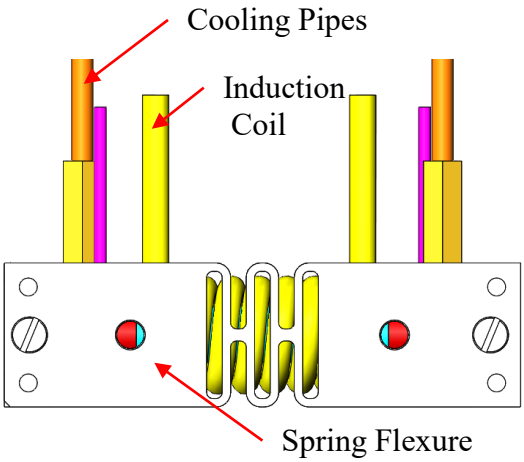

Figure 20. CAD model of spring flexure for assembly preload

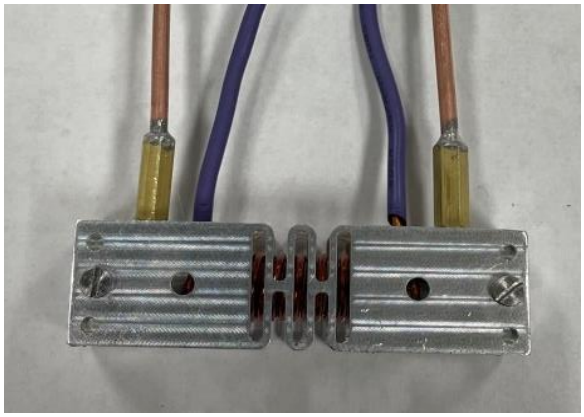

Figure 21. Implementation of the CAD model for the spring flexure

Using the section view shown in Figure 22, the thermal expansion of the actuator and the change in length of the air gap for the HQLI is discussed below.

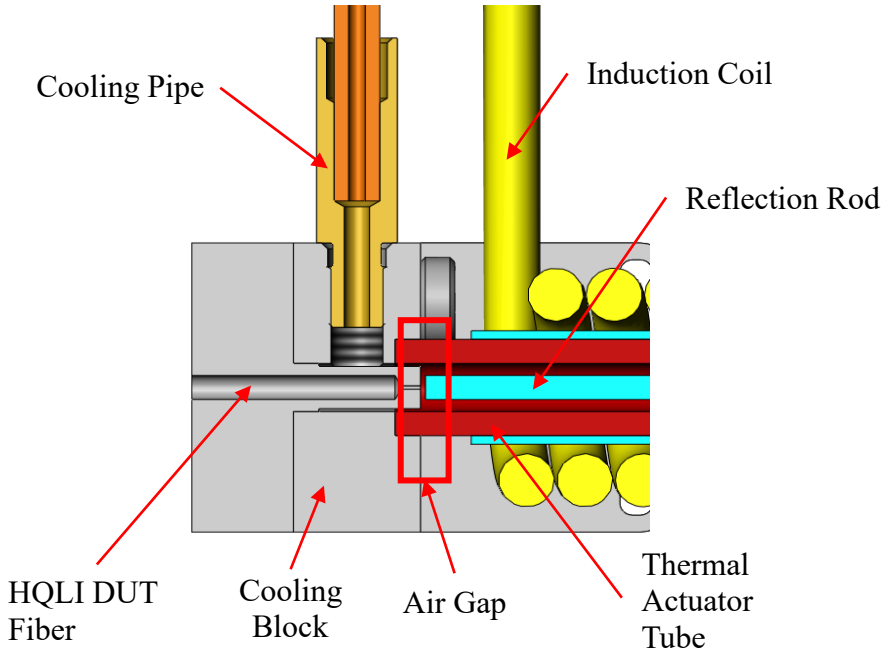

Figure 22. Cross sectional view of the air gap for the thermal actuator

Assuming static conditions with no loading, when heat is applied to the thermal actuator, the overall length (and diameter) of the thermal actuator tube will increase proportionally to the length of the actuator and its resulting temperature change. While this is occurring, the reflection

rod, which is made from a fused quartz glass, has an almost negligible change in overall length due to its very low coefficient of thermal expansion (the reflection rods extends by 0.003 mm if its temperature is increased by 150°C). The fiber that is opposite the end of the reflection rod is isolated from the actuator tube via a cooling block. Therefore, the fiber's position will change in direct relationship to the change in length of the thermal actuator. With an initial air gap of 0.3 mm, a final desired displacement of 0.1 mm, the final air gap will increase to approximately 0.4 mm.

When the operating temperature is changed from room temperature to 150°C, the initial air gap (at room temperature) is 0.3 mm plus the expansion due to the new operating temperature (0.083 mm), and a final desired displacement of 0.1 mm, the final resulting air gap is approximately 0.5 mm.

The reflection rod shown in Figure 16 and Figure 22 presented several challenges with respect to its very low coefficient of thermal expansion in comparison to the high coefficient of thermal expansion of the aluminum actuator components. As large temperature changes (and thus large displacement deviations) were expected, a compliant mechanism was required to maintain the reflection rod's stability both radially and axially.

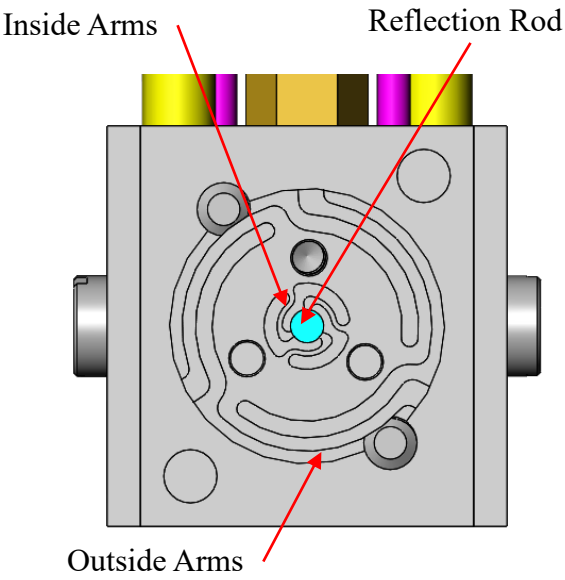

Figure 23. CAD model of reflection rod flexure to maintain reflection rod stability

Figure 24. After manufacturing, reflection rod flexure to maintain reflection rod stability

The reflection rod has an outside diameter of 1.000 mm, an overall length of 33.500 mm, and a coefficient of thermal expansion of 0.55 $\mu m \cdot m^{-1} \cdot °C^{-1}$. The bottom platen that houses the reflection rod, shown below in Figure 25, has an internal diameter of 1.02 mm, an overall length of 9.00 mm, and a coefficient of thermal expansion of 23.6 $\mu m \cdot m^{-1} \cdot °C^{-1}$.

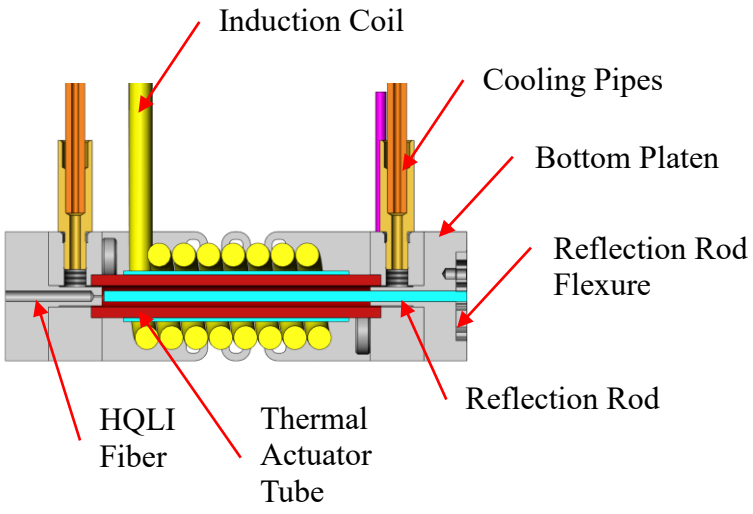

Figure 25. CAD section view of reflection rod, bottom platen, and flexure to maintain reflection rod position.

If high temperature deviations were not to be expected, an epoxy could be used to secure the location of the reflection rod to the bottom platen. However, with the planned high temperatures, the epoxy would need to be radially compliant to allow for the bottom platen's inside diameter to expand by approximately 0.003 mm and the reflection rod to stay approximately the same diameter. Thus, the radial consideration is a minor influence and was not the major factor for implementing the reflection rod flexure, but it was a design consideration.

Second, due to the high operating temperature, the bottom platen will extend axially (approximately 28 μm). This expansion is problematic in that the reflection rod needed to maintain its original position throughout operation. The flexure shown in Figure 24 above helps to resolve this issue. There are two sets of fingers in the flexure, one set on the inside of the flexure known as inside arms and a second set on the outside diameter known as outside arms (see Figure 23). The inside arms grip the reflection rod with a preload of 1.5 N per arm. With the dimensional changes (due to temperature), this preload is approximately 0.05 mm per arm. Considering the change in diameter of the reflection rod (less than 0.05 μm at final temperature), this preload should remain constant throughout the complete temperature profile.

The outside arms grip the inside diameter of the bottom platen with a preload of 1.1 N per arm with a displacement of 0.13 mm per arm. Since the bottom platen is aluminum and the reflection rod flexure is aluminum, this force and displacement should be maintained with the temperature change.

The thickness of this flexure has been reduced to 1.000 mm. This thickness results in the reflection rod's axial position changing by around 3 μm at final operating temperature in comparison to around 28 μm if the reflection rod is epoxied to the bottom platen. As stated above, the inside diameter of the bottom platen is 0.020 mm larger than the outside diameter of

the reflection rod. This increase in diameter should provide adequate radial clearance to allow the bottom platen to expand axially and not influence the original position of the reflection rod.

2.2.3. ELECTRICAL

The electrical system for the thermal actuator, shown below in Figure 26, consists of a PWM signal sent from a DAQ device, a motor controller board that switches the main power from the high wattage power supply using the PWM signal from the DAQ, a ZVS circuit that provides the high frequency output for the LC oscillator and high power MOSFETs, and a high wattage power supply.

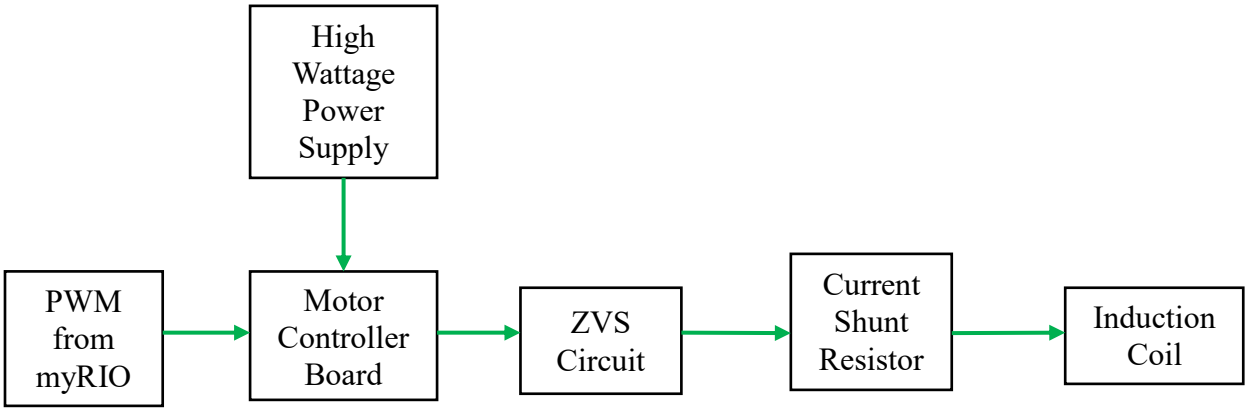

Figure 26. Block diagram of the electrical system for the thermal actuator

The work that was completed on the electronics for the initial prototype, (C. H. Fan, Design and Performance of a Thermal Actuator Driving a Preloaded Linear Translation Stage), were integrated into the compact thermal actuator.

Also included in the electrical system are the various sensors that are used throughout the system. These sensors include a strain gauge type load cell that is used to verify the applied load to the actuator, surface mount RTDs with pressure sensitive adhesive that are mounted to the device stage and the frame's bottom platen, and a backup knife edge displacement sensor (Lin) for use at room temperature. Additional details for each of these sensors is included in Appendix

7. Pneumatic and Electrical Schematic for DCVs, Appendix 8. Electrical Schematic for RTD on Thermal Actuator Circuit Board, and Appendix 9. Electrical Schematic for the ZVS Circuit.

2.2.4. THERMAL

As mentioned before, the compact thermal actuator in its simplest form is a machined aluminum tube. Aluminum is the best choice thermally for the actuator due to optimization of the induction heating circuit and the skin depths for the eddy currents. The design goal was to achieve a minimum of 75 μm of axial displacement during operation. The actuator has an overall length of 27 mm which results in a required temperature change of 157°C. Using these parameters, the maximum tensile stress due to this amount of temperature increase results in a safety factor of 1.9 (compared to yield stress). In (C. H. Fan, Design and Performance of a Thermal Actuator Driving a Preloaded Linear Translation Stage), equations were developed to determine the eddy currents in the complete coil as well as the skin depth and the thermal analysis that was completed for the initial prototype. The same procedure will be utilized for the thermal actuator presented in this thesis. For this actuator, 111 A of eddy current and a skin depth of 175 μm are used in the simulation, with a given input current of 68 A and frequency of 205 kHz (experimental results, see Figure 80). The resistance to current flowing through the actuator can be determined using the electrical resistivity of aluminum, the skin depth of the eddy current, and the physical dimensions of the actuator tube. The resulting resistance was calculated to be approximately 315 μΩ. Twenty-three coils (using 20 gauge solid copper wire) were designed to be used with the actuator. The total heat input to the actuator using the induction coil and the induced eddy currents is approximately 90 W. Given the mass of the actuator (636 mg), the calculated final temperature of the actuator is approximately 168°C. The requirement for the 0.1 mm of displacement results in a final temperature of approximately

177°C. Due to the estimated maximum temperature, the target maximum axial displacement was reduced from 100 μm to 75 μm. Thus, the overall design of the actuator is approximately in line with the calculations developed using the initial prototype.

Sensors have been integrated into the cooling system (purple blocks in Figure 17) to help determine the optimum cooling parameters as well as verify the model that was developed with the initial prototype. RTD temperature sensors have also been integrated into the frame's bottom platen and the device stage to determine the magnitude of heat being conducted to these components during operation. These measurements will help determine the requirements for the water cooling (yellow blocks in Figure 17) in the frame and device stage.

CHAPTER 3: EXPERIMENTAL APPARATUS AND RESULTS

This chapter discusses the chronological progression of the experimental apparatus for both the HQLI (Section 3.1) and the compact thermal actuator (Section 3.2).

3.1. HOMODYNE QUADRATURE LASER INTERFEROMETER

A block diagram of the optics that comprise the HQLI is shown below in Figure 27 and a top-down picture of the optical test apparatus is shown in Figure 28. For the outlines shown, red lines will typically indicate optical components and green will indicate electronic components. The HQLI has evolved from a free space laser device to an all-fiber interferometer with dielectric mirrors opposing the MOD arm fiber and the DUT arm fiber.

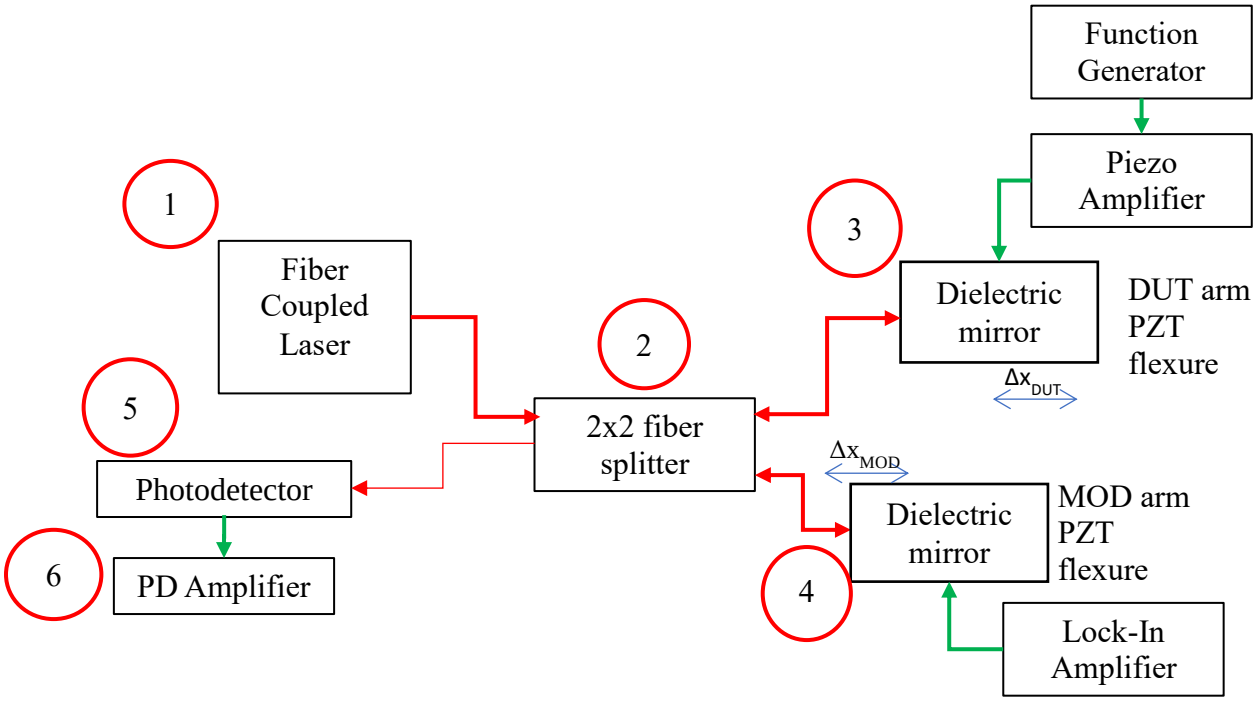

Figure 27. Block diagram of the optics for the HQLI

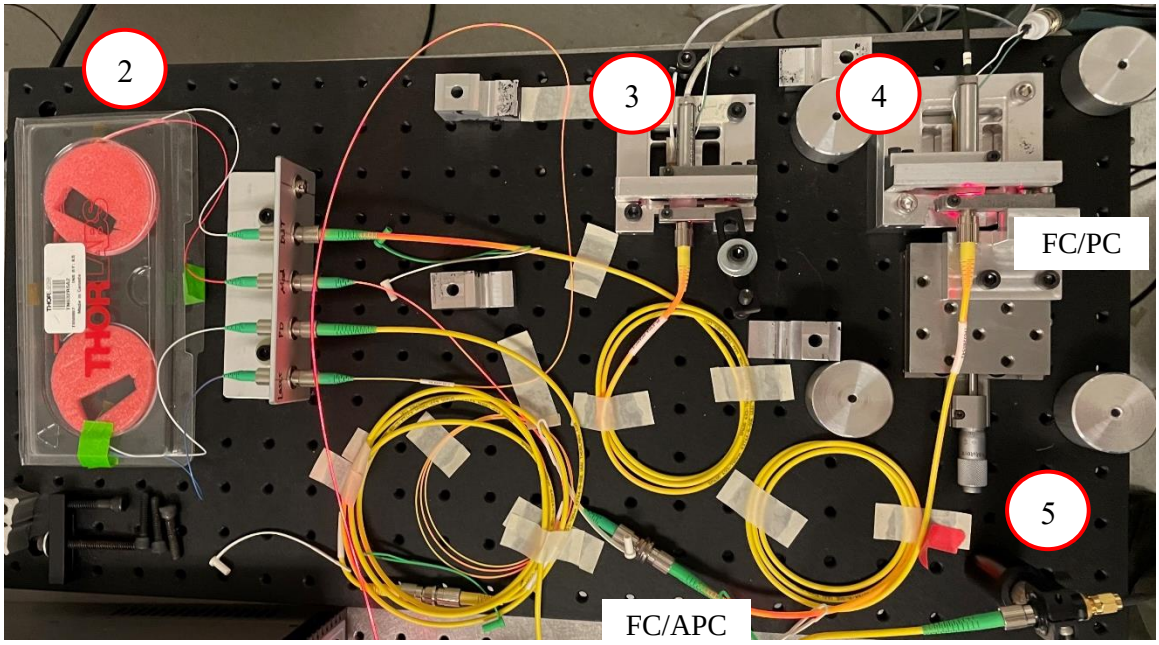

Figure 28. Optical test apparatus for the HQLI

From Figure 28, the type of fiber optic connectors used throughout the apparatus can be observed. In areas where no reflections are desired, FC/APC connectors (green boots) are used. These connectors have an 8° angle on the fiber end face. This angle directs the reflected light into the cladding and prevents it from traveling back down the length of fiber. All fiber-to-fiber connections utilize APC connectors, as well as the connection to the PD. In areas where reflections are desired, FC/PC connectors (yellow boots) are used. These connectors have a flat polish, no angle polished onto the end face (the end face is normal to the propagation axis of the fiber). The two areas where reflections are desired are at the MOD arm mirror (position 4) and the DUT arm mirror (position 3). All fibers are taped down using generous loop radii to avoid optical power loss in the fiber.

3.1.1. INITIAL TEST APPARATUS – FREE-SPACE HQLI

The initial test apparatus for the free-space HQLI consisted of a commercially available, fiber coupled, 635 nm laser diode, collimating lens, fiber coupling lens, and two turning mirrors. These components were configured with a long optical path length to enable easier alignment of

the laser beam to the collimating lens on the fiber coupling side. Figure 29 shows a picture of the initial test apparatus. Starting on the bottom right-hand side, the laser diode, the initial collimating lens (installed in a five-axis kinematic mount), and a Faraday isolator convert the diverging light from the laser diode into a collimated laser beam. Note, the beam exiting the laser diode is elliptical in shape and there are no beam shaping optics in the initial setup.

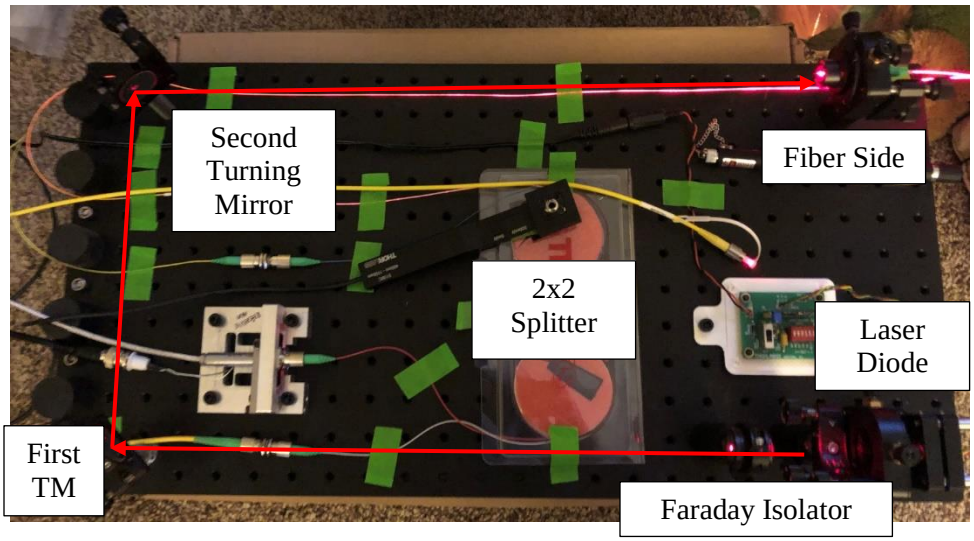

Figure 29. Initial HQLI test apparatus

After exiting the Faraday isolator, the beam travels to the first turning mirror (TM), (mounted in a two-axis kinematic mount) and is turned 90°. The beam then travels to a second TM and is turned another 90° such that the beam has completed a 180° directional change. Lastly, the beam enters a fiber coupling lens that is mounted in a five-axis kinematic mount. The fiber coupling lens has a plano-convex lens assembled at the focal point of the fiber to focus the collimated light from the laser onto the core of the SM fiber. Due to the wavelength of the laser beam, the mode field diameter of the SM fiber was calculated to be 4.3 μm. The kinematic adjusting mechanisms have 80 TPI adjusting screws (resulting in approximately 0.5° per turn) and were not sensitive enough to align the laser beam to the fiber to achieve better than 50% coupling efficiency.

Testing continued with the transmission of the free-space laser to the actual HQLI comprising – the two input by two output fiber splitter, the DUT arm, the MOD arm, and the photodetector. Figure 30 shows the integration of the free-space laser into the HQLI.

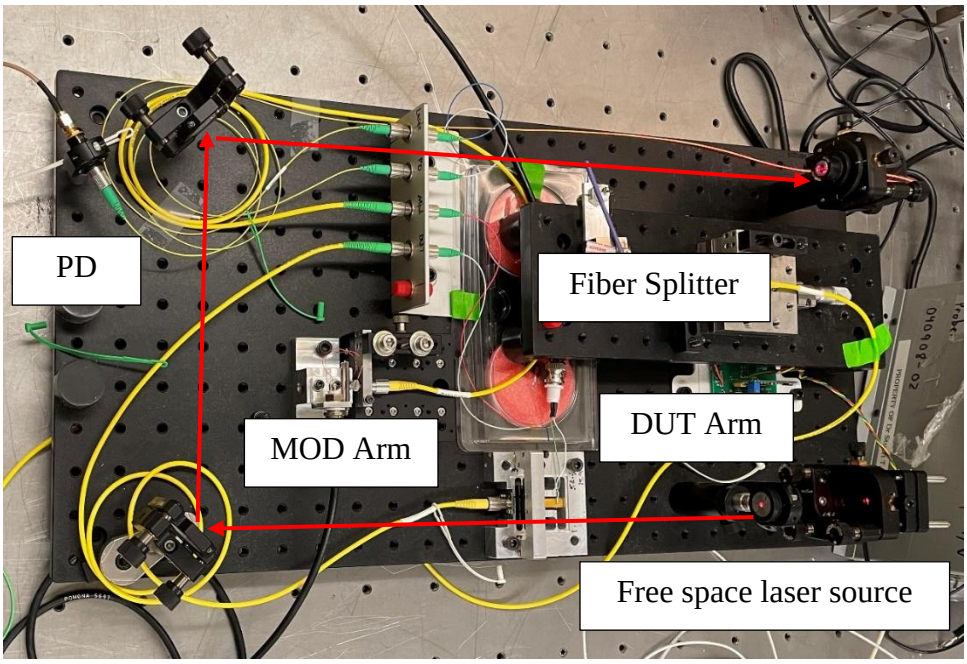

Figure 30. Free space laser installed into HQLI

Given the low coupling efficiency of the laser to the fiber, the photodetector was still able to collect fringes in the optical signal, see Figure 31 below. The oscilloscope was able to measure the fringes in the photodetector's signal, but the amplitude was too low for the lock-in amplifier to provide reliable detection. In Figure 31, note that channel two has a peak-to-peak voltage of approximately 40 mV.

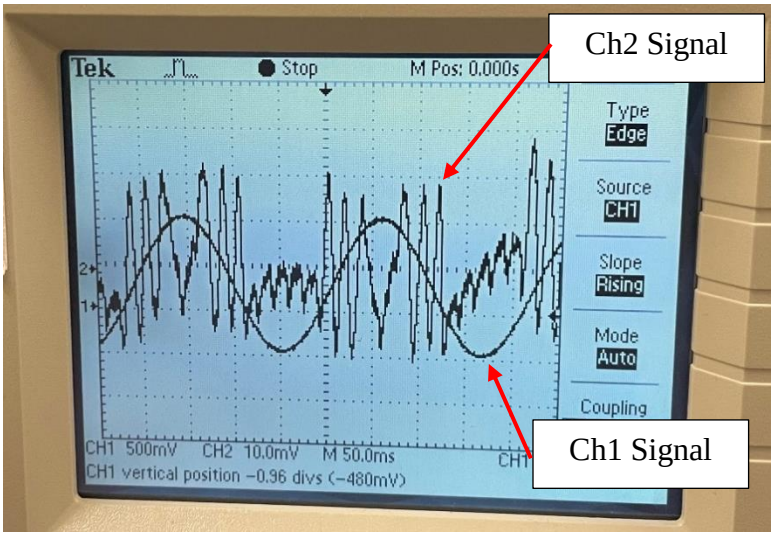

Figure 31. Photograph of PD amplifier output showing a fringe pattern and drive signal corresponding to a motion of 2 µm in the DUT arm of HQLI

3.1.2. PZT / MIRROR CONFIGURATION

The initial DUT arm and MOD arm PZT assemblies consisted of an aluminum flexure, a PZT actuator, a gage block to use as a target for the capacitance gage, and a quartz glass microscope slide. The assembly of one arm is shown below in Figure 32 and Figure 33.

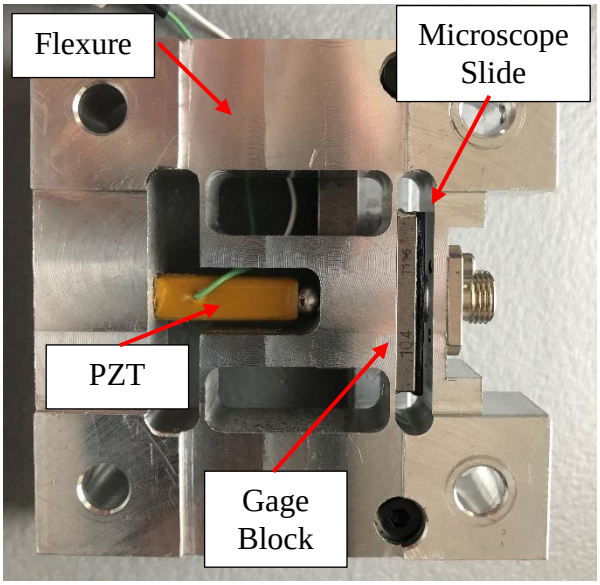

Figure 32. DUT and MOD arm PZT assembly, shown upside down

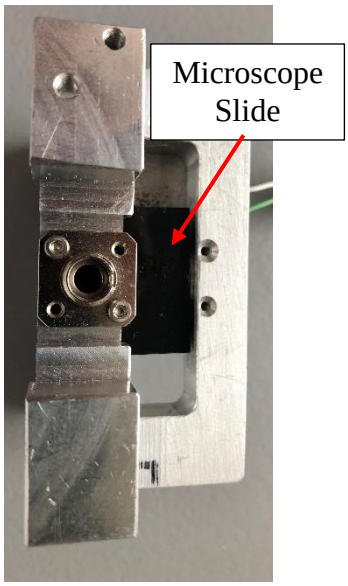

Figure 33. DUT and MOD arm PZT assembly, front view

The microscope slides that serve as the external mirror surface of the Fabry-Perot cavity were cut to an overall size of 24 mm x 25 mm x 1.00 mm thick from a stock microscope slide

using a resin bonded diamond wheel and a surface grinder with flood coolant, see Figure 34 for an example of the grinding setup with the flood coolant turned off. A technique called "waxing in" was used to temporarily bond the microscope slide to a piece of sacrificial float glass underneath. The grinding wheel was taken to full depth and the cross slide was slowly advanced through the microscope slide, otherwise known as creep feed grinding. The original width and thickness of the microscope slides were maintained, only the length of each sample was cut to the appropriate dimension. See Appendix 1. Grinding Glass Plates and Reflection Rods for additional details on this procedure and materials.

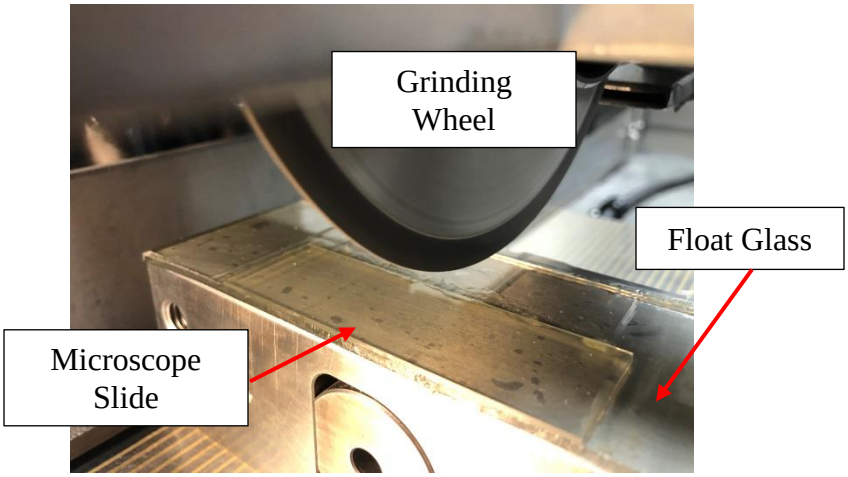

Figure 34. Grinding the microscope slides to size

Following grinding to final size, the microscope slides had a coating of absorptive chalkboard paint (Valspar Black Chalkboard Paint, SKU number 042397588297) applied to one surface in three layers to minimize reflections from the back side of the slide. Eliminating the reflection from the back side of the microscope slide was important to only have the primary surface reflection coming back to the HQLI.

The optical performance of each coating was verified using a measurement technique that measures the incident optical power through each microscope slide. Figure 35 below shows a schematic of the first step in the test setup. An optical fiber will launch 635 nm light onto a large

area photodetector without a microscope slide in between; this is the reference or baseline measurement. The average baseline power measured was 2.065 mW.

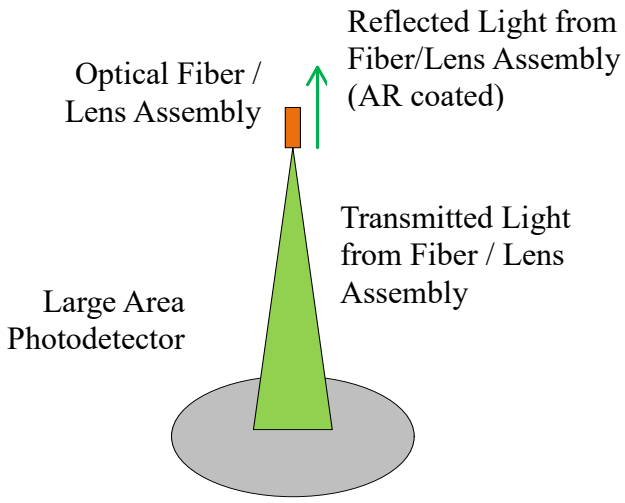

Figure 35. Microscope slide characterization, step 1

The second step was to place a standard, uncoated microscope slide between the fiber and the photodetector. Figure 36 below shows the test setup. Given the microscope slides have an index of refraction such that a back reflection of ~4% for each surface, there should be an approximate 8% drop in the initial power measurement. After inserting the uncoated microscope slide, the measured power was approximately 1.886 mW, a change of approximately 8.8% as expected. Assuming the material is consistent and the primary and secondary reflections are equal, the average reflection per surface is 4.4%.

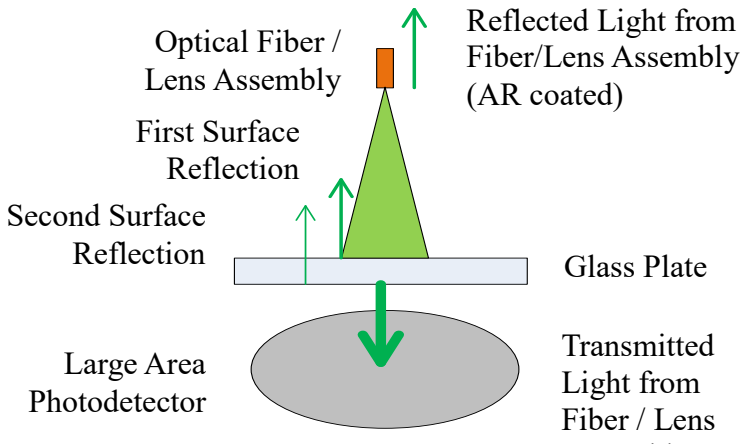

Figure 36. Microscope slide characterization, step 2

The third step was to replace the uncoated microscope slide with a coated microscope slide, coating side down, see Figure 37 below. The incident power was once again measured.

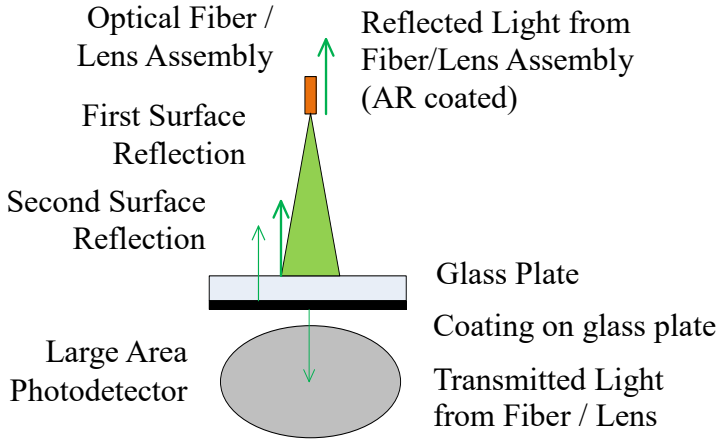

Figure 37. Microscope slide characterization, step 3

The final step was to rotate the microscope slide such that the coated side was the first side incident to the optical source, see Figure 38 below.

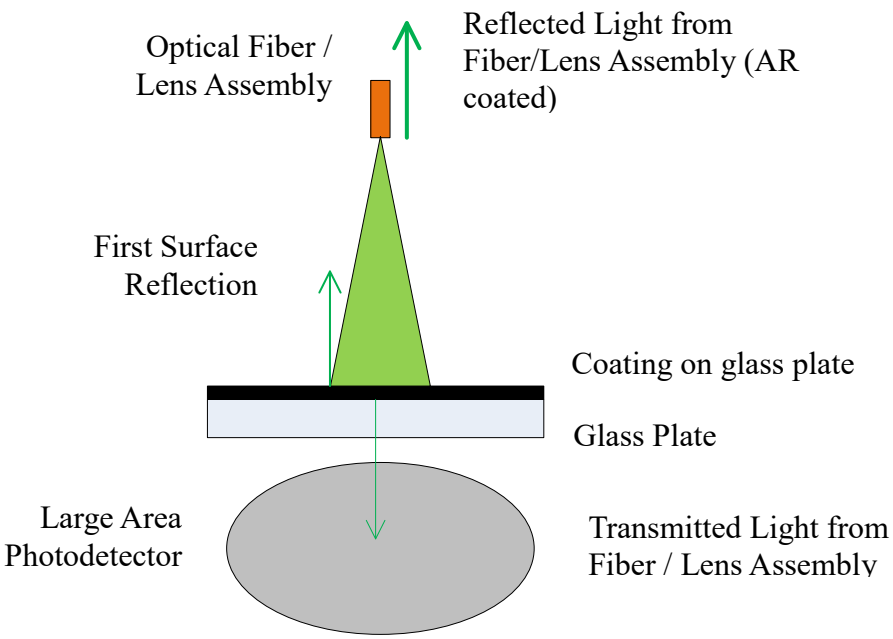

Figure 38. Microscope slide characterization, step 4

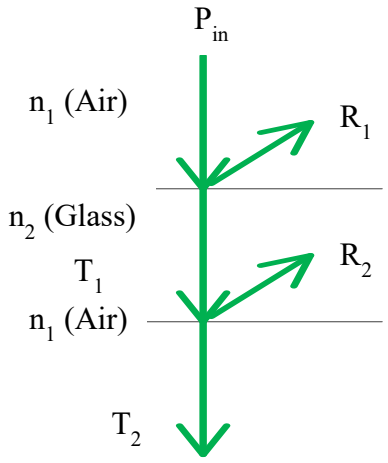

Figure 39. Schematic of transmission and reflections for microscope slide characterizations

Using Figure 39 as a guide, equations were developed to characterize the coating. To begin, the incident power on the system is labeled P_{in}. The light is traveling through air which has an index of refraction, n_1. At the first interface, there is a material change that results in an index change from n_1 to n_2. This index change causes some portion of the light to be reflected (R_1), some portion to be transmitted (T_1), and some to be absorbed (Fresnel Equations and Conservation of

Energy). The microscope slides are produced with a fused silica glass that has almost negligible light absorption at visible wavelengths, enabling the absorption component to be neglected. As such, all light incident on a surface must equal the portion transmitted plus the portion reflected. After the first interface, the light travels through the microscope slide and interacts with the second interface and once again, some portion is transmitted and some is reflected (and a negligible amount is absorbed).

The equations to describe the system at the first interface is:

$$T_1 = P_{in}(1 - R_1) \qquad \textit{Equation 29}$$

where

T_1 = transmitted power at the first interface [mW],

P_{in} = input power to the system [mW], and

R_1 = reflected power at the first interface [%].

Equation for the second interface is:

$$T_2 = T_1(1 - R_2) \qquad \textit{Equation 30}$$

where

T_2 = transmitted power at the second interface [mW],

T_1 = input power from the first interface [mW], and

R_2 = reflected power at the second interface [%].

Putting Equation 29 into Equation 30 and solving for T_2:

$$T_2 = P_{in}(1 - R_1)(1 - R_2) \qquad \textit{Equation 31}$$

For step 2, the reflection at the first interface should be the same as the reflection at the second interface, let $R_1 = R_2 = R$ and solve Equation 31:

$$T_2 = P_{in}(1 - R)^2$$ *Equation 32*

Using Equation 32 and solving for *R*, *R* was determined to be 4.43% using the experimental measurements.

Moving to step 3, the chalkboard paint has a small amount of transmission but is mostly absorptive, per prior experiments conducted by Dr. Smith. Note, this experiment did not use a second power meter to measure the return signal to verify the power of the reflected signal. Referencing Figure 39, replace R_2 with A_2 for absorption. Going back to Equation 31 and rewriting:

$$T_2 = P_{in}(1 - R)(1 - A_2)$$ *Equation 33*

where:

A_2 = the absorption of the paint at the second interface [%].

Solving Equation 33 for A_2 and using the known parameters from the previous test, A_2 was determined to be 99.2% absorptive. The last step was to flip the microscope slide over and perform the test to determine A_2 from the front side. A_2 when measured from the front side was approximately 99.6% absorptive. Averaging these two values, the chalkboard paint is approximately 99.4% absorptive when applied in three layers. Results from each test are summarized below in Table 2.

Table 2. Microscope slide coating test results

Measurement Step	Measured Power [mW]	Transmitted Power to PD [%]	Reflection or Absorption [%]
1	2.065		
2	1.886	91.3	4.4 R
3	0.015	0.8	99.2 A
4	0.0085	0.4	99.6 A
R	4.4% (measured)		
A	99.4% (measured)		

The high absorption value at the back interface of the microscope slide will reduce any secondary reflections coming back onto the fiber to insignificant levels, thus the only reflection to the fiber can be considered to be from the primary interface.

After the initial testing was complete and the fringe contrast was not sufficient for reliable phase extraction, the decision was made to switch from a low reflective mirror (the microscope slide was the mirror with a 4% reflection) to a dielectric mirror with a 99% reflection. The new dielectric mirrors were epoxied onto the gage blocks in both the MOD arm and DUT arm PZT actuators, see Figure 40 below. The results discussed in Section 4.1 utilize these mirrors.

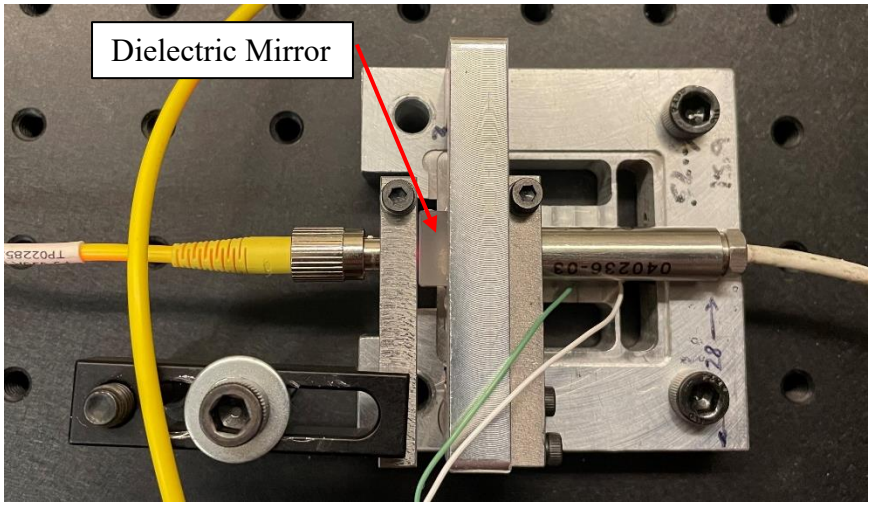

Figure 40. Modified MOD arm and DUT arm PZT actuators with dielectric mirrors

3.1.3. PERFORMANCE TESTING OF LASER DIODES

Due to the low amplitude of the fringes, subsequent testing was performed to quantify specific performance characteristics, such as the average power fringe, the laser source output power and stability over time, of several commercially available lasers and laser diodes. A major goal of this task was to identify the best available source preferably having a higher output

power to increase the amplitude of the interference fringes. Results from this study are summarized in Table 3.

Several different brands of laser diodes, visual fault locators (VFL's), and a new fiber coupled laser were characterized. The laser used in the initial testing was the Thorlabs HL6312G laser diode. This laser diode, coupled with the EK1101 laser diode controller operating in power control mode, gave the highest ranking in signal to noise ratio of all sources. The main down-side with this unit was the low output power.

The second ranked unit was the VLM-6500003-LPA2 laser diode. To integrate this laser into the test setup, a new alignment technique was designed to attempt to reduce the overall size of the system. A tip-tilt flexure was designed to be able to accept either the VLM laser or the US Laser (third ranked unit). However, due to scheduling conflicts in the machine shop, the tip-tilt flexure was not manufactured in time to evaluate.

Table 3. Performance metrics of several commercially available laser sources

Laser Description	Average Power [mW]	Power Fluctuation [μW]	Signal to Noise [-]	Signal to Noise Ranking
Thorlabs HL6312G	0.847	1.82	465	1
VLM-6500003-LPA2	2.078	7.1	293	2
Ebay Dot Laser	35.98	318	113	4
VFL_2	9.5	307	31	6
US Laser M635-5I	3.92	20.2	194	3
Q-Photonics QFLD-635-40S (100 mA drive current, 25°C)	11.65	144	81	5

The fourth ranked laser was accidentally destroyed during testing and could not be evaluated in the test apparatus. The last laser to be tested was the Q-Photonics fiber coupled laser with integrated thermo-electric cooling and current control. This laser is currently operational in the system.

3.1.4. FIBER COUPLED LASER TEST APPARATUS

The fiber coupled laser from Q-Photonics was tested and has approximately thirteen times the power of the Thorlabs HL6312G laser diode when operated with a drive current of 100 mA and a temperature of 25°C. Given this amount of power, the fringes were still not reliably visible to the lock-in amplifier. From Figure 41, the amplitude of the fringes (cyan colored trace) has increased from 40 mV using the Thorlabs HL6312G laser diode to approximately 300 mV using the Q-Photonics fiber coupled laser diode. The green trace is the displacement of the DUT mirror measured with a capacitance gage and the purple trace is the drive signal of the DUT arm PZT transducer. In this instance, the drive signal was a 1.2 $V_{pk\text{-}pk}$ signal at a frequency of 2 Hz, the resulting displacement was approximately 1.5 μm.

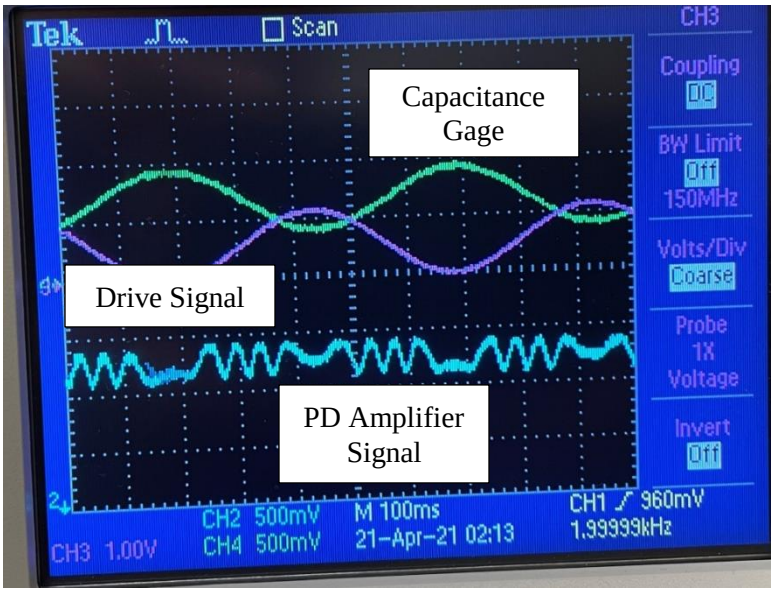

Figure 41. Fringe pattern of the fiber coupled laser

One additional area that was tested with the implementation of the fiber coupled laser was the ability to change the length of the DUT and MOD arm fibers. From the literature review, several sources specify that these arms need to be identical in length. In this thesis, this constraint was not observed. In fact, there was a deviation in the fiber length of 0.5 m between

the DUT arm and the MOD arm. When operating with the arms at approximately the same length, more difficulty was experienced in obtaining good quality fringes.

3.1.5. SIGNAL CONDITIONING ELECTRONICS

Following initial testing, the need for additional signal conditioning electronics to enable the lock-in amplifier to lock onto the carrier frequency was realized. (Ellis) discusses an approach to improving the fringe contrast by implementing a high pass filter (HPF) and an amplifier to maximize the fringe contrast. In the field of optics, the fringe contrast I_{FC} (or Michelson contrast or visibility) is defined as:

$$I_{FC} = \frac{I_{Max} - I_{Min}}{I_{Max} + I_{Min}} \qquad \textit{Equation 34}$$

where:

I_{FC} is the fringe intensity contrast [$\propto$ to $V \cdot V^{-1}$],

I_{Max} is the maximum observed fringe amplitude [$\propto$ to V], and

I_{Min} is the minimum observed fringe amplitude [$\propto$ to V].

In this thesis, because fringe phase is extracted from the extraction of modulation harmonics amplitudes, this definition is expanded to include the electronic signal conditioning circuit consisting of a buffer amplifier, an offset amplifier, a gain amplifier, a high pass filter, and a voltage divider for integration with a lock-in amplifier. A block diagram indicating major components of the signal conditioning electronics is shown below in Figure 42 and an image of the circuit implementation is shown in Figure 43. Additional details concerning the construction of each of the blocks is shown in Appendix 2. Electrical Schematic for Signal Conditioning Electronics.

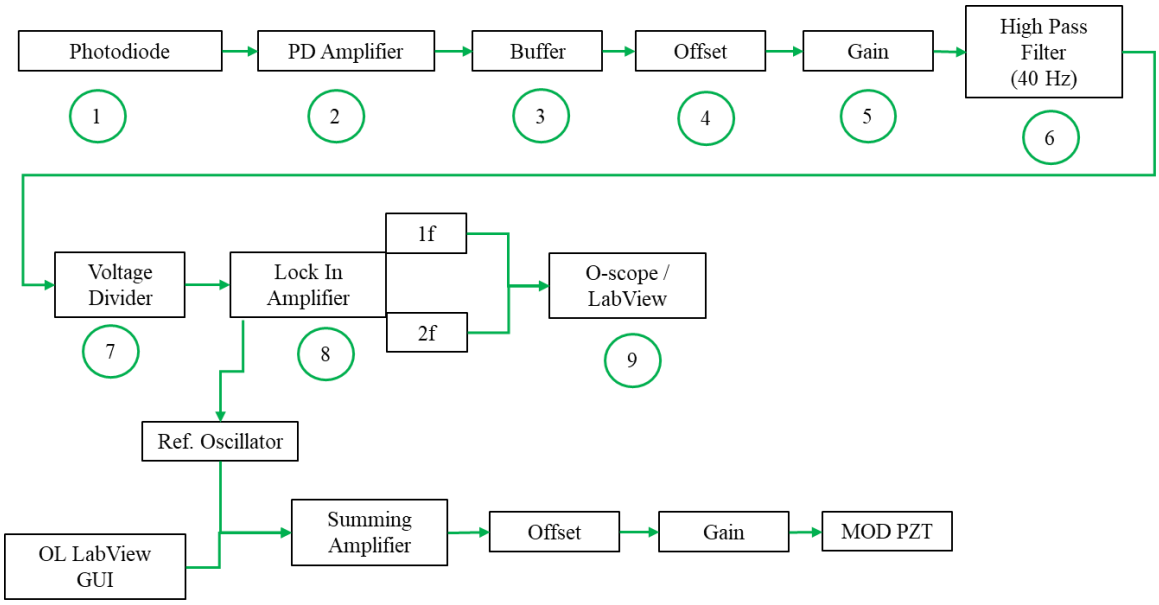

Figure 42. Signal conditioning electronics for HQLI

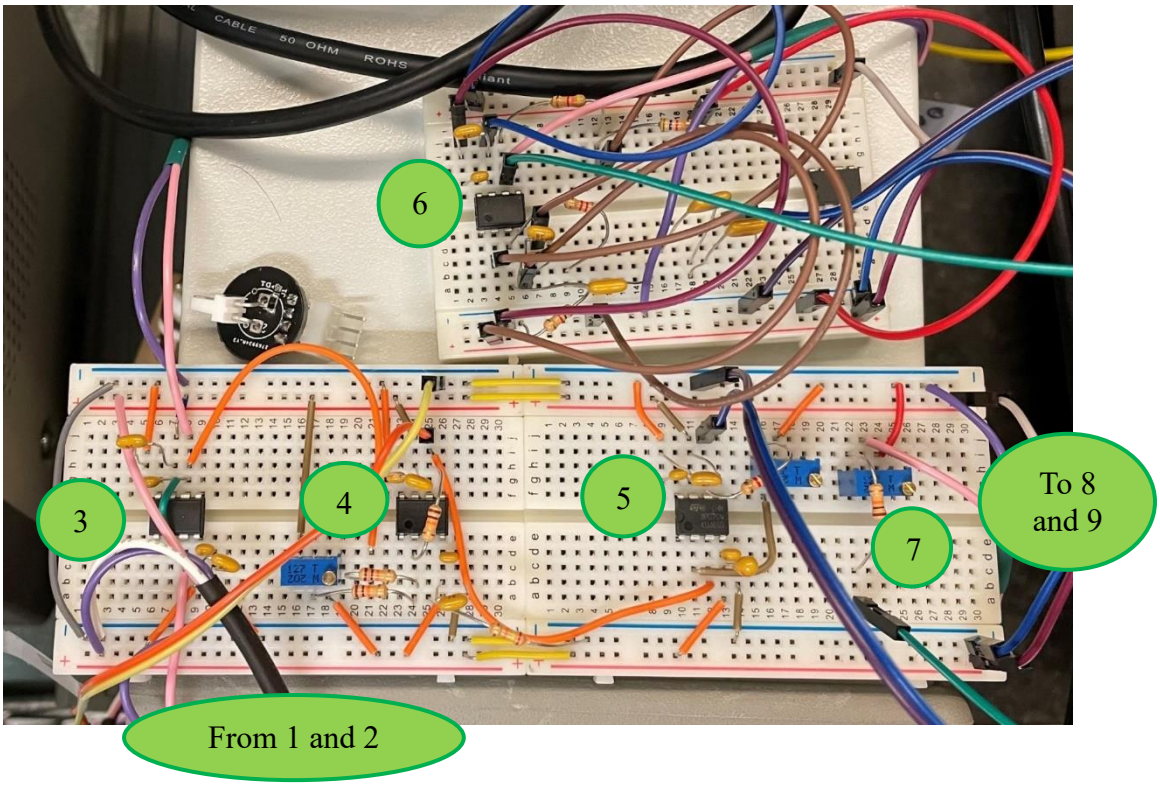

Figure 43. Implementation of signal conditioning electronics

Following the implementation of the signal conditioning electronics into the system, a large change in signal strength was observed. Figure 44 shows the output signal of the PD amplifier in

green and the signal following the buffer amplifier in purple; this corresponds to the component three outlined in the signal conditioning scheme shown in Figure 43. Restating one of the original issues, the fringe amplitude is very small (~400 mV) sitting on top of a very high DC offset (~4.0 V).

Figure 44. PD Signal and Post Buffer Signal (sinusoidal motion of the DUT mirror with amplitude of 1 µm and cycle time of 2 s)

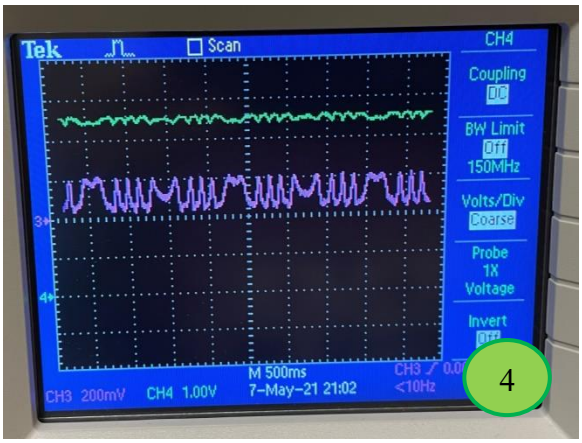

Figure 45. PD Signal and Post Offset Signal (sinusoidal motion of the DUT mirror with amplitude of 1 µm and cycle time of 2 s)

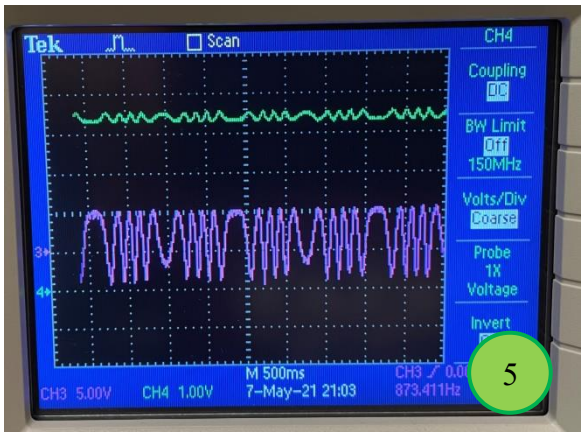

Figure 46. PD Signal and Post Gain Amplifier Signal (sinusoidal motion of the DUT mirror with amplitude of 1 µm and cycle time of 2 s)

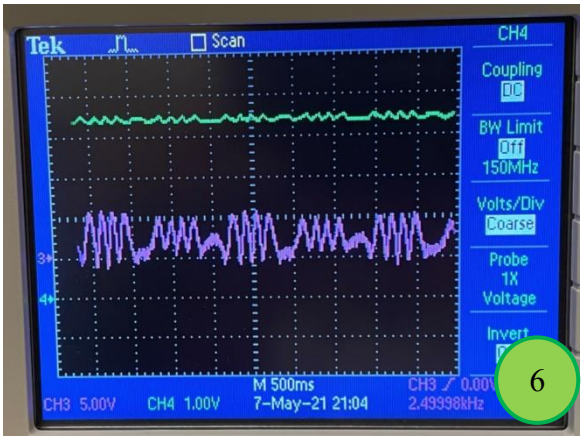

Figure 47. PD Signal and Post High Pass Filter Signal (sinusoidal motion of the DUT mirror with amplitude of 1 µm and cycle time of 2 s)

Figure 45 shows the original PD signal in green and the offset amplifier signal in purple. Note at this stage the scale for the purple signal has decreased by five and the previous high DC offset is now ~0.05 V. Also, the signals represent a sinusoidal motion of the DUT mirror with a displacement of approximately 2 µm and a frequency of approximately 0.5 Hz. This results in the fringe contrast increasing from ~0.04 after component three to ~0.69 after component four in

the signal conditioning circuit. The ability to adjust the offset is provided by the 2 kΩ potentiometer, shown on the left side of the offset amplifier in Appendix 2. Electrical Schematic for Signal Conditioning Electronics.

The signal following component five is shown in green in Figure 46 (compare to original PD signal in green). Now, the signal has a peak-to-peak voltage of ~10 V and an offset of 0.05 V. The ability to adjust the gain of the amplifier is accomplished using a second 2 kΩ potentiometer, shown on the left side of the gain amplifier in Appendix 2. Electrical Schematic for Signal Conditioning Electronics.

The last stage of signal conditioning, step six, is to run through the active high pass filter. This particular design has a passband of approximately 42 Hz. This passband needs to be low enough to accept the modulation frequency, which is 2.5 kHz. The 42 Hz initial value was chosen when testing the electronics with very low modulation frequencies.

Appendix 2. Electrical Schematic for Signal Conditioning Electronics has additional details on the construction of this amplifier and the values chosen. At the end of the signal conditioning process, the fringe contrast is ~1.00 before being sent into the lock-in amplifier. The last stage of signal conditioning is to pass the signal from component six through a voltage divider to reduce the 10 V amplitude to the maximum 1 V amplitude of the lock-in amplifier.

Following the implementation of the signal conditioning electronics, the lock-in amplifier was able to lock onto the 2.5 kHz reference frequency and send the first and second frequency harmonics to the oscilloscope, see Figure 48 and Figure 49 below.

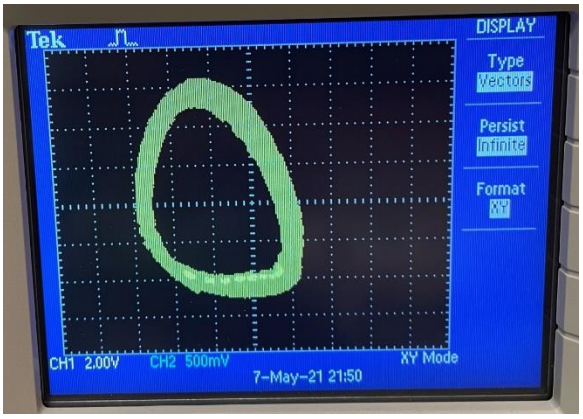

Figure 48. Initial Lissajous pattern observed on oscilloscope

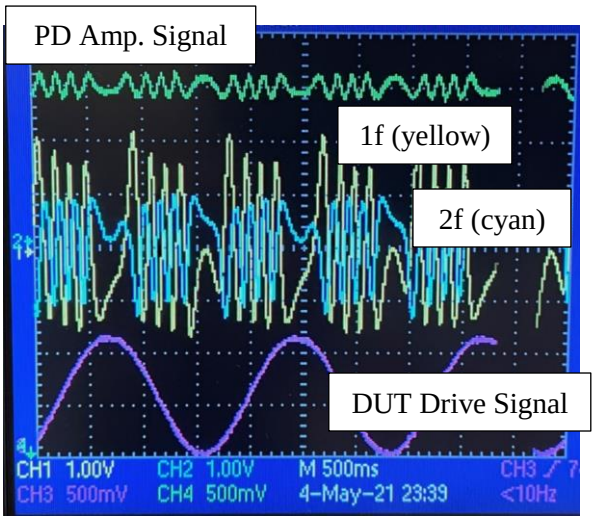

Figure 49. All signals captured following implementation of signal conditioning electronics (sinusoidal motion of the DUT mirror with amplitude of 1 μm and cycle time of 0.5 s)

In Figure 49, the green trace is the original signal from the PD amplifier, the purple trace is the drive signal for the DUT arm PZT from the function generator, the yellow trace is the first harmonic from the lock-in amplifier, and the cyan trace is the second harmonic trace from the lock-in amplifier. Figure 48 shows the Lissajous diagram for the 1f and 2f signals shown in Figure 49.

3.1.6. MOD ARM MIRROR

During initial testing and before the addition of the signal conditioning electronics, there was little to no observed modulation present in the fringes. The modulation frequency was initially set at 10 kHz and a depth of 25 nm. The initial MOD arm PZT actuator was similar in design to the DUT arm PZT actuator. The modulation was not visible in the fringes and a design change was made to address the high drive frequency (10 kHz).

A new MOD arm system was designed, built, and assembled, see Figure 50 below. The new system was designed with a single crystal piezo chip that could be actuated with up to a 1000 V signal and a resulting maximum displacement of 1.2 μm. The piezo element has a capacitance of

125 pF and a resonant frequency of 185 kHz. With a desired operating frequency of 10 kHz, the resulting impedance would require an operating current of 65 µA. Calculating the slope of voltage per displacement for the new single crystal piezo chip, to operate with approximately 20 nm of modulation depth would require an input voltage of approximately 17 V and minimal current (65 µA). These values are within the operating range of a high output impedance function generator, and thus the function generator is capable of directly driving the crystal.

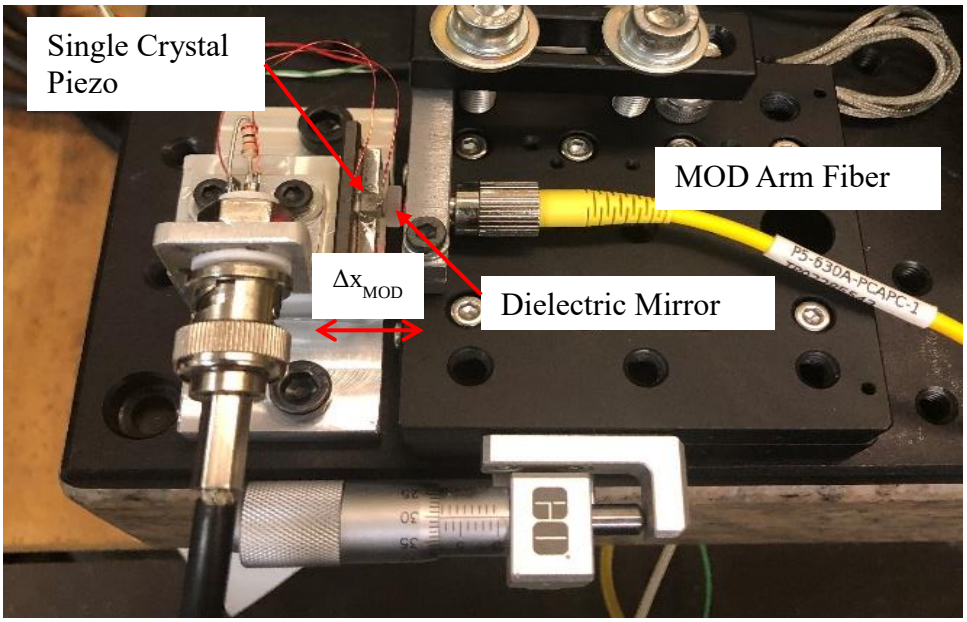

Figure 50. MOD Arm mirror, v2

MOD arm mirror displacements with the new mechanical setup were measured using Kumar Arumugam's custom built confocal probe and recorded an estimated modulation depth of 17 nm. This displacement was observed using several operating frequencies ranging from 10 Hz up to the target frequency of 10 kHz. The new MOD arm mirror was installed in the HQLI and modulation was still not present on the fringes. When reviewing the HQLI electronics system as a whole, the PD amplifier had bandwidth limits based on the power being measured. When the input power was very low, the bandwidth of the PD amplifier was reduced to 5 kHz due to the amplifier's increase in gain. Thus, the MOD arm frequency of 10 kHz was not visible to the

electronics. The MOD arm frequency was then reduced from 10 kHz to 500 Hz to enable sampling of the modulation depth. Figure 51 and Figure 52 show an example of the modulation not being present in the fringes and an example with the modulation present in the fringes. In Figure 52, the modulation has a depth of approximately 150 nm.

Figure 51. Fringe pattern with modulation not present

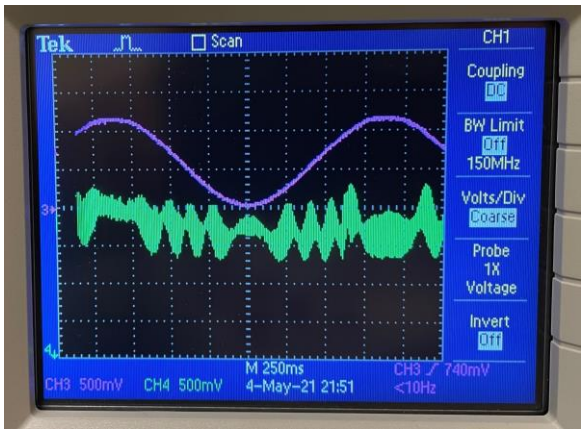

Figure 52. Fringe pattern modulation present

Continuing to use the second version of the MOD mirror resulted in additional issues that needed to be addressed. The desire to operate with a higher modulation frequency meant the input signal to the PD needed to be increased by at least a factor of ten. Several changes were then made that included switching both the DUT mirror and the MOD mirror from coated microscope slides to dielectric mirrors, switching the laser source from an open, free space laser diode to a commercially available fiber coupled laser diode, and the addition of a capacitance gage to monitor the position of the MOD mirror. One additional change was the switch from using a function generator as the reference for the modulation frequency and starting to use the lock-in amplifier as the reference source. These changes resulted in use of the initial MOD arm mirror PZT actuator (Figure 32). With the above changes implemented, the system could then be operated with a MOD frequency of 2.5 kHz, and the output power was sufficiently high that the lock-in amplifier was able to reliably lock onto the modulation signal. Table 11 in Appendix

3. Lock-In Amplifier Settings lists the settings that were used in the final tests after the system was stabilized.

During stability testing of the new MOD arm PZT actuator, the PZT drive signal was plotted against the capacitance gage on the oscilloscope and the Lissajous figure was observed, see Figure 53 and Figure 54 below. The drive signal for the modulation arm is on the x-axis and the capacitance gage feedback is shown on the y-axis. Figure 53 shows the instability in the MOD arm position after approximately 5 min of operation and Figure 54 shows the instability after 120 min of operation. Instability in both figures is shown via cascaded plots of the Lissajous signal via 'persist' settings on the oscilloscope. As a result of this test, it was clear the displacement of the MOD arm mirror needed to be stabilized.

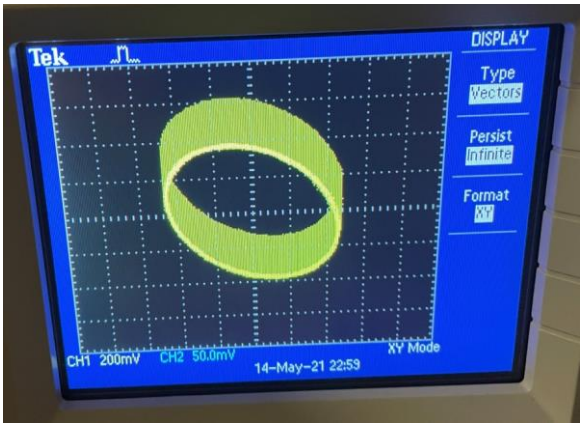

Figure 53. Lissajous figure of the MOD arm mirror over a five minute measurement time

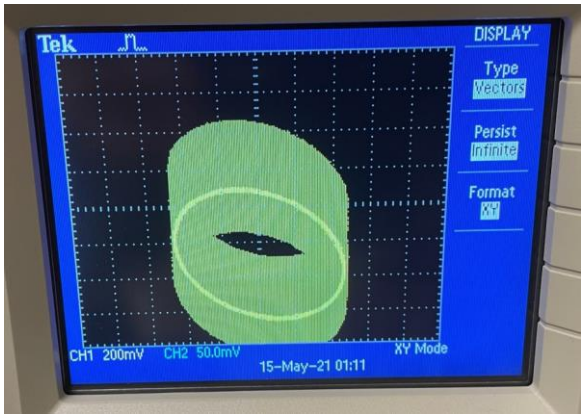

Figure 54. Lissajous figure of the MOD arm mirror, after 120 minutes

The MOD arm mirror was operated in open loop with a DC offset from the myRio (myRio is a DAQ device sold by National Instruments that is programmed via LabVIEW®) being added to the modulation output from the lock-in amplifier. A schematic of the electronics for this circuit can be found in Appendix 4. Electrical Schematic for Open Loop Control of MOD Arm Mirror. The DC offset was chosen by the operator to try and stabilize the Lissajous. This resulted in the mirror being stable for short periods of time (less than 5 min), but still showing

signs of instability (greater than 5 min). The next attempt was to close loop control the MOD mirror using the capacitance gage and this was somewhat successful but there was still an outside influence acting on the system that the controller could not over-ride. Figure 55 below shows the instability of the first and second harmonics after 5 min of operation when the MOD mirror was closed loop controlled. While the system was under closed loop control, attempts were made to vary the phase of each harmonic to achieve a stable elliptical shaped Lissajous, but those attempts were only successful for a short period of time.

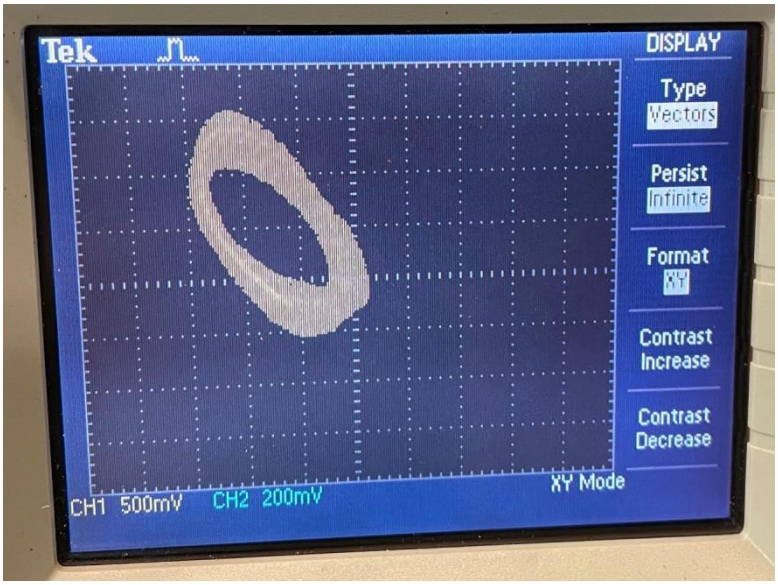

Figure 55. I1f and I2f instability after five minutes under closed loop control

A second technique was explored where the I2f was monitored and controlled in both open loop and closed loop. The electronics for the closed loop control were based on the same circuit as the capacitance gage control, but the feedback was the I2f signal running through a low pass filter (f_c = 0.01 Hz) that created a DC value. The myRio provided a signal that was proportional to the I2f DC value and that signal was added to the initial reference signal from the lock-in amplifier (oscillator settings in lock-in amplifier). This control scheme (both open loop and closed loop) was largely unsuccessful as well.

Additional testing was completed where the polarization of the DUT arm optical signal was controlled using a linear polarizer to review the impacts on the stability. The technique was also largely unsuccessful, as polarization was not the primary contributing source of instability.

When brainstorming other causes that could potentially influence the signal changes, an RTD was added to the MOD arm PZT flexure to monitor the temperature of the flexure during operation, the RTD can be seen in Figure 56 below.

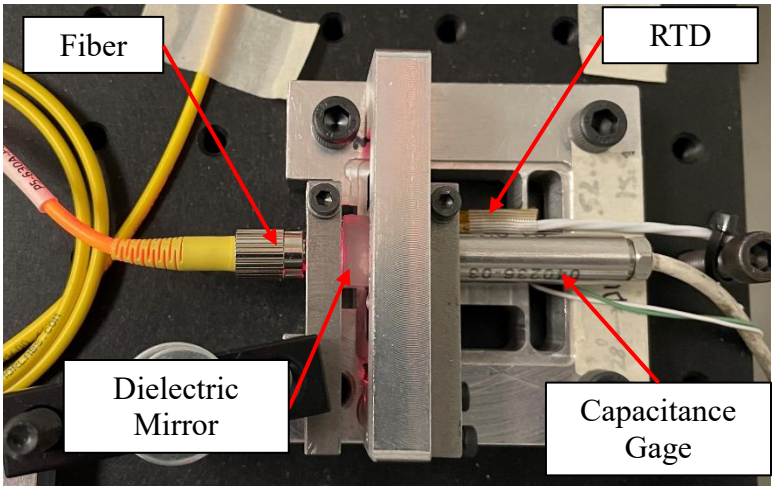

Figure 56. MOD arm PZT flexure with RTD added

Temperature monitoring of the MOD arm PZT flexure revealed cyclical temperature swings inside the Duke 120 laboratory of 0.3°C peak to peak with a time period of the temperature oscillations at approximately 15 min. The change in position of the MOD arm mirror was evaluated during these temperature fluctuations. The distance between the leaf arms on the flexure was measured to be 26.5 mm. With a flexure material of 7075-T6 aluminum, (coefficient of thermal expansion of 23.6 $\mu m \cdot m^{-1} \cdot °C^{-1}$), and temperature change of 0.3°C, this results in a theoretical positional change of 240 nm due to temperature alone, which is almost one and a half times the depth of the initial modulation.

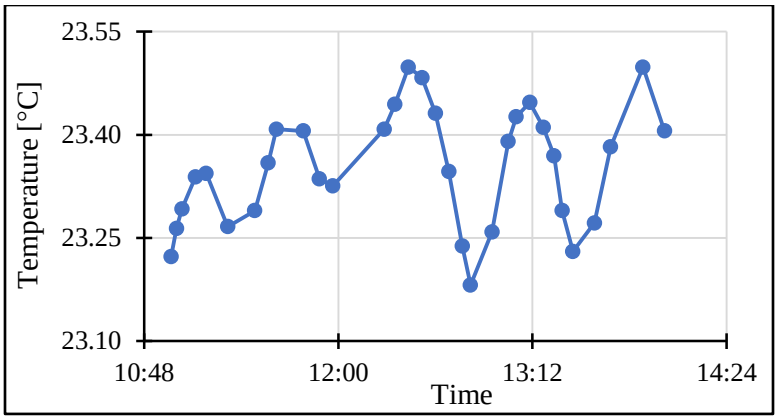

Figure 57. MOD arm temperature in Duke 120 laboratory

After observing the temperature swings in the Duke 120 laboratory, the complete apparatus was moved from Duke 120 to Duke 140, a metrology laboratory with a temperature control system specified to maintain a constant temperature within ±0.1°C. Figure 58 below shows the temperature of the Duke 140 lab during one testing interval of around 2 hrs. The measured temperature range during this test was 0.05°C which resulted in a predicted change in displacement of the MOD mirror of 30 nm.

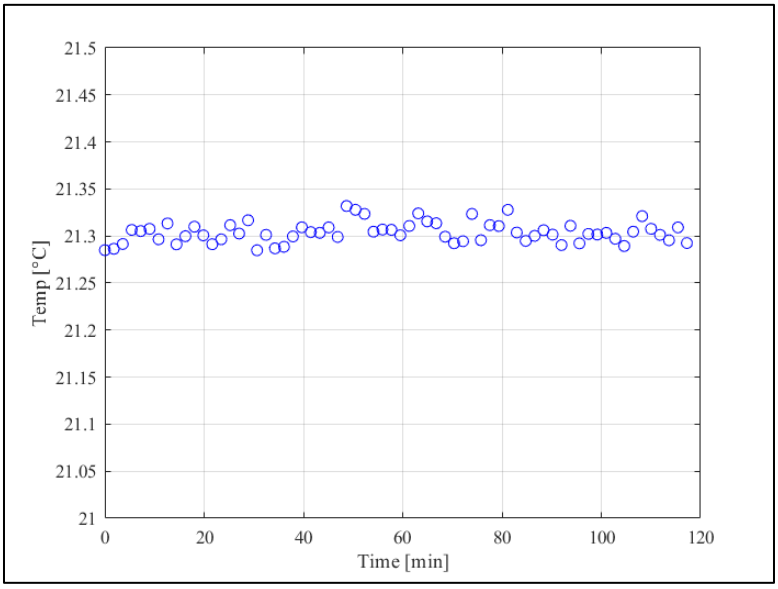

Figure 58. Duke 140 Laboratory temperature during testing

Following the move to Duke 140, the temperature stability of the MOD arm mirror was improved by a factor of eight. Subsequent testing of the HQLI showed improvement to the stability of the system.

After moving into Duke 140, after initial testings, it was observed that the phase of the first and second harmonics of the signal were not changing as significantly as was occurring in Duke 120. At this point, the reference phase of the two harmonics were both set to 0°. The settings for the lock-in amplifier (after moving into Duke 140) are listed in Table 11 in Appendix 3. Lock-In Amplifier Settings. The lock-in amplifier was configured to provide the X_1 and X_2 harmonics to the DAC1 and DAC3 outputs, respectively. Using the X_1 and X_2 resulted in the output voltage of the DACs spanning ± 10 V. Due to the elliptical shape of the Lissajous, the output sensitivities of the lock in amplifier were chosen to maximize the output of each DAC without overloading as well as attempting to as much as possible normalize the shape of the Lissajous before any post signal processing occurred.

3.1.7. FINAL TEST APPARATUS – ALL-FIBER HQLI

The previous sections have outlined the changes that have been made to the system in an effort to achieve a stable, low noise, HQLI and the evolution from a free-space design to an all-fiber implementation. An updated block diagram of Figure 27 is shown below in Figure 59 that outlines the complete revised optical system, the addition of the signal conditioning electronics, and the interface with the operator via a LabVIEW® GUI. The laser source was operated with a drive current of 85 mA at a control temperature of 25°C. This resulted in an average power of 6.2 mW measured directly at the output of the laser. Figure 60 and Figure 61 below show the actual implementation of the optical setup. Figure 60 shows the implementation with covers installed over the MOD arm and DUT arm and Figure 61 shows without the covers installed.

(Elezov) mentioned the need for adding shielding / covers to eliminate outside influence from ambient light and thermal influences. The covers proved to be another additional improvement in performance of the system. The ambient lighting in the laboratories do have an impact on the system due to their broadband visible wavelengths interfering with the wavelength of the optical source. The covers also help to maintain the thermal stability of the MOD arm when operators are in close proximity to the system. The data presented in Figure 58 was collected with the cover over the MOD arm.

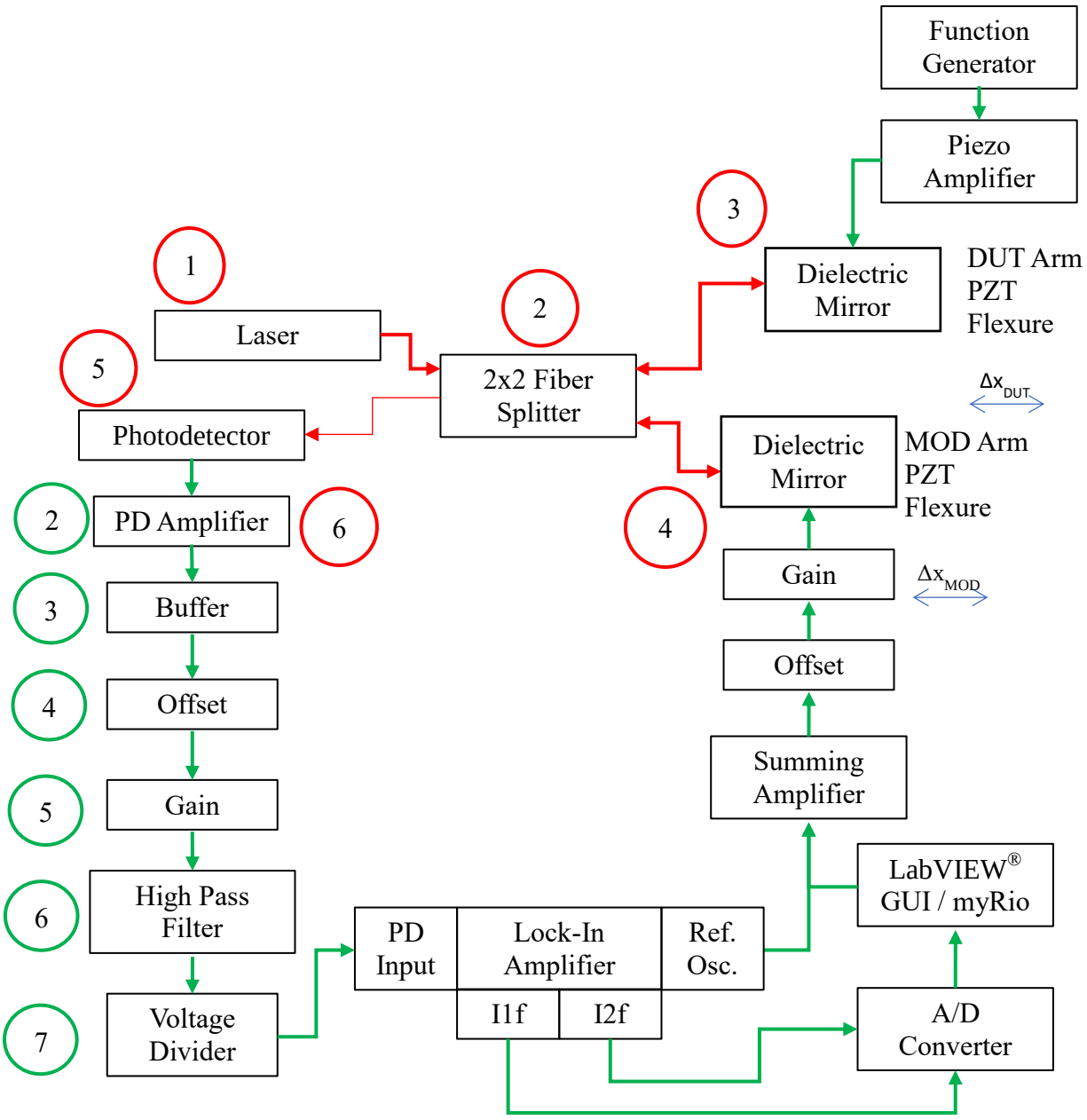

Figure 59. Updated block diagram of HQLI

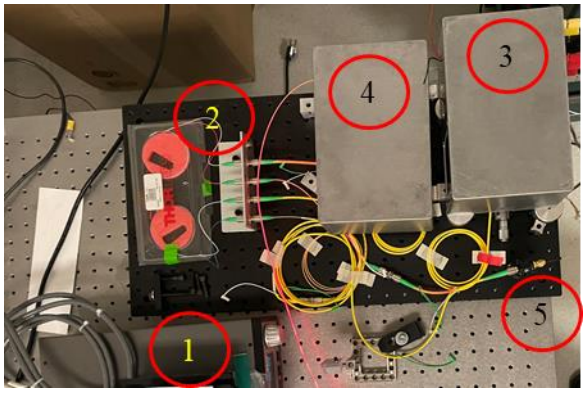

Figure 60. Final implementation of optical setup

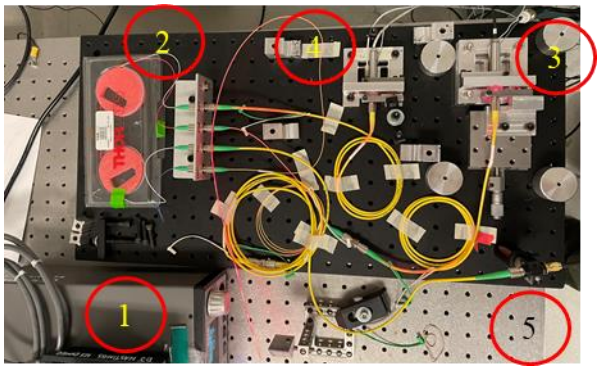

Figure 61. Final implementation of optical setup with covers removed

The implementation of all electronics is shown below in Figure 62. The signal conditioning electronics for the HQLI are shown under the oscilloscope and on the first shelf of the cart. The RTD signal conditioning electronics are shown on the first shelf of the cart. Also shown are the capacitance gages that will be used for calibration of the HQLI and the 16 Bit analog to digital converter that was developed by Chunjie Fan for integration with the myRio.

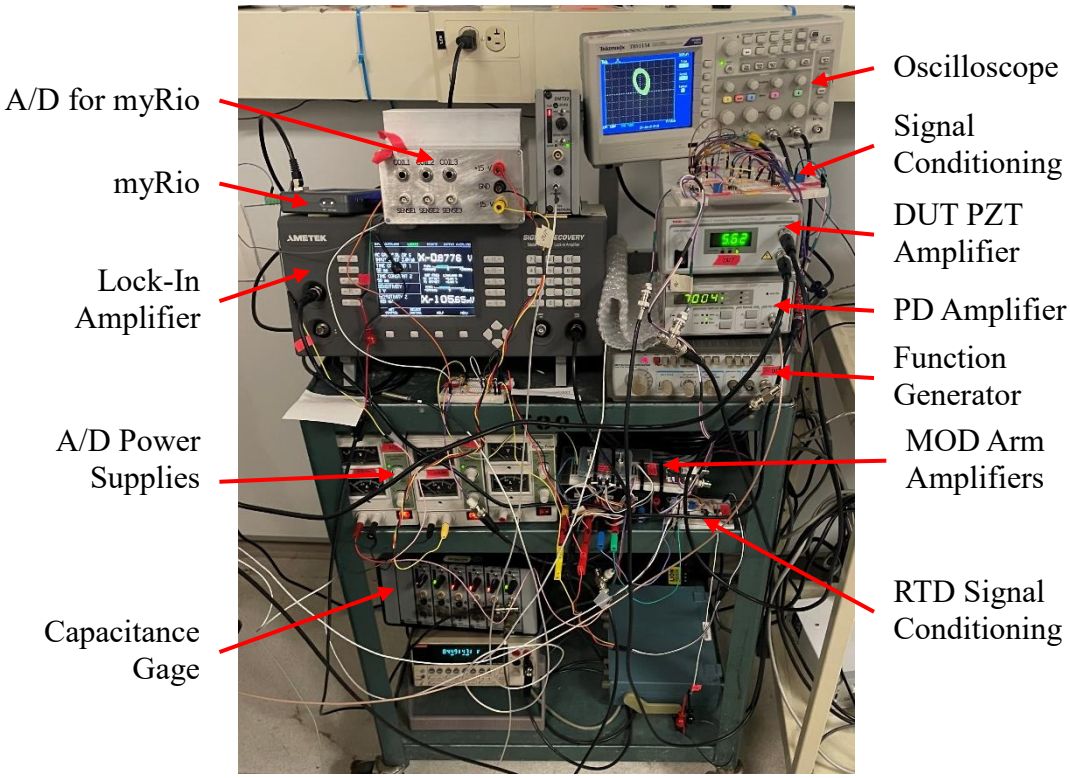

Figure 62. Final implementation of electronics for the HQLI

An image of the LabVIEW® GUI can be seen below in Figure 63. The I1f and I2f graphs are the voltage outputs of the lock-in amplifier for the amplitudes of the first and second harmonics, the Cap Gage graph is the measured voltage of the capacitance gage on the DUT arm PZT, and RTD graph is the measured temperature in volts of the MOD arm PZT. There are also accommodations for changing the filename of the saved data, a start/stop button for saving data, a stopwatch timer, computation loop period, and lost frame counter. As it turns out, the controller can operate much faster in monitoring mode alone than it can when saving data. The saving data function is accomplished by writing directly to a USB flash drive on the myRio versus writing to a drive on the host computer. There is a significant amount of time required for saving data at high loop rates and that time results in some lost frames to occur. Missing frames was not a major issue in development because as system evaluation was carried out with data being logged to USB. When later implementation of the thermal actuator in this system is done, consideration to the lost frames will need to be made so there is no lost information during operation of the HQLI. In most cases, the phase unwrapping and subsequent calibration conversions will occur in LabVIEW® and will not need to be dealt with externally.

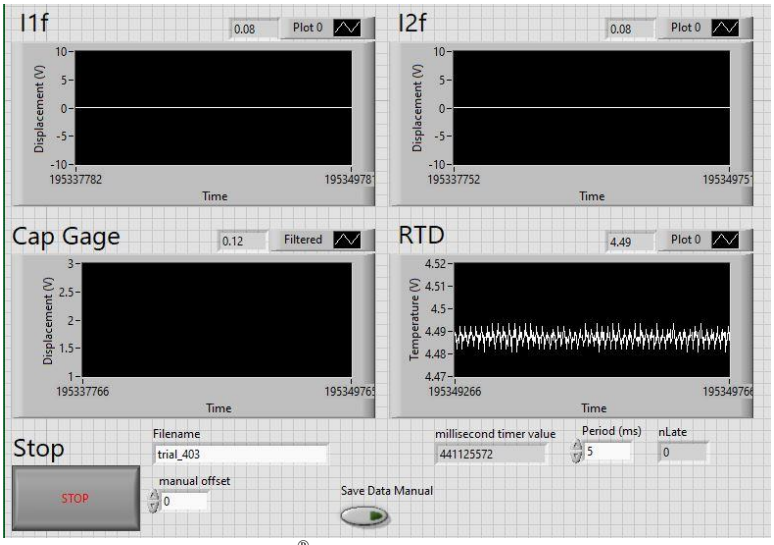

Figure 63. LabVIEW® GUI of the open loop control program

3.1.8. ALGORITHMS

After the implementation of the signal conditioning electronics, switching to a more thermally stable metrology lab, and initial testing, a data processing methodology was developed. Two broad parameters needed to be addressed – the displacement calibration / phase unwrapping and the signal to noise which includes the fringe contrast and displacement resolution. A comprehensive signal to noise flow chart is shown in Figure 64 and the phase unwrapping and displacement calibration flow chart is in Figure 65. In each step passing through both flow charts, a corresponding graph of the data from the previous step is included to aid in visualization of each function during the execution of the algorithms. Both flow charts also outline the necessary equations for each step in the algorithm. Appendix 12. MATLAB® Program for Evaluating HQLI has a copy of the MATLAB® m file that is used to evaluate the measured data.

The first step for both cases is to extract and record the elapsed time, I1f data, I2f data, capacitance gage data, and the RTD data. Since there were cases where missed frames were encountered, the first step was to look for repeat elapsed time data and discard the second data point that was the same as the previous data point.

To reduce storage of large amounts of data, when processing the signal to noise data, a loop was created that would divide the measured files into a specific number of integer multiple values across the total evaluation period. The specific value for the loop length is the period of the DUT arm. The period was determined experimentally in a separate step and was maintained throughout all testing. The capacitance gage signal was converted from volts to displacement by using a previous calibration sensitivity value provided by Chunjie Fan.

To unwrap phase, the second step was to fit an eight term Fourier series (Equation 35) to both the I1f and I2f versus the capacitance gage signal for each of the loop iterations. The resultant of the fit is known as $I1f_{fit}$ (as well as $I2f_{fit}$).

$$I1f_{fit} = a_0 + \sum_{n=1}^{N} a_n cos(n\omega t) + b_n sin(n\omega t) \qquad \textit{Equation 35}$$

where:

$I1f_{fit}$ = Fourier series fit to the first harmonic signal [V],

a_0 = DC offset of the first harmonic [V],

a_i = amplitude of the cosine function at that particular iteration [V],

b_i = amplitude of the sine function at that particular iteration [V],

ω = fundamental frequency of the system [rad·s^{-1}],

n = number of terms in the series [-], and

t = the displacement of the capacitance gage [μm].

The difference between the measured value (I1f) and the fitted value ($I1f_{fit}$) was then calculated using Equation 36. If the difference was greater than three standard deviations, that data point was then removed from the data set, along with each corresponding I2f, capacitance gage, and RTD data point. This step was completed for both I1f and I2f.

$$Diff_1 = I1f - I1f_{fit} \qquad \textit{Equation 36}$$

where:

$Diff_1$ = difference in the fitted value of the I1f and the measured value of I1f [V],

$I1f$ = measured value of I1f [V], and

$I1f_{fit}$ = fitted value of I1f [V].

New arrays were compiled and the new $I1f_{fit}$ and $I2f_{fit}$ were offset shifted (Equation 37) and normalized (Equation 38) (this is still the first loop iteration).

$$I1f_{offset} = I1f_{fit} - \overline{I1f_{fit}} \quad \textit{Equation 37}$$

where:

$I1f_{offset}$ = $I1f_{fit}$ that has been translated by the mean value of the $I1f_{fit}$ [V],

$I1f_{fit}$ = fitted value of I1f [V], and

$\overline{I1f_{fit}}$ = mean value of the $I1f_{fit}$ [V].

$$I1f_{norm} = \frac{I1f_{fit} - \overline{I1f_{fit}}}{\max(I1f_{fit}) - \min(I1f_{fit})} \quad \textit{Equation 38}$$

where:

$I1f_{norm}$ = normalized value of the fitted I1f [V],

$I1f_{fit}$ = fitted value of I1f [V],

$\overline{I1f_{fit}}$ = mean value of the $I1f_{fit}$ [V]

Max($I1f_{fit}$) = maximum value of the $I1f_{fit}$ [V], and

Min($I1f_{fit}$) = minimum value of the $I1f_{fit}$ [V].

The mean of the absolute value of the $I1f_{norm}$ and $I2f_{norm}$ signals was then determined (Equation 39) (for the first loop iteration). This value is the Signal for the first loop iteration.

$$S = \overline{|I1f_{norm}|} \quad \textit{Equation 39}$$

where:

S = absolute value of the average amplitude of the $I1f_{norm}$ signal [V].

The standard deviation of the noise after the outliers were removed was then divided by the range of the $I1f_{fit}$ to determine the normalized noise of the first loop iteration (Equation 40).

$$N = \frac{\sigma(diff_{1OR})}{\max(I1f_{fit}) - \min(I1f_{fit})}$$ *Equation 40*

where:

N = noise of the measured loop [V],

$\sigma(diff_{1OR})$ = the standard deviation of the $diff_1$ values after the outliers have been removed [V],

Max($I1f_{fit}$) = maximum value of the $I1f_{fit}$ [V], and

Min($I1f_{fit}$) = minimum value of the $I1f_{fit}$ [V].

The signal to noise was then calculated using Equation 41 and the fringe contrast using Equation 42 for the first loop iteration.

$$SN_1 = \frac{S_1}{N_1}$$ *Equation 41*

where:

SN_1 = signal to noise ratio of the first harmonic [$V \cdot V^{-1}$],

S_1 = normalized amplitude of the first harmonic signal [V], and

N_1 = RMS amplitude of the noise of the first harmonic [V].

$$FC_1 = 1 - \frac{1}{SN_1}$$ *Equation 42*

where:

FC_1 = fringe contrast of the first harmonic [-] and

SN_1 = signal to noise ratio of the first harmonic [$V \cdot V^{-1}$].

The signal to noise and fringe contrast for each loop iteration was stored for evaluation later and this process was repeated for the total number of loops. The final step was to determine the minimum signal to noise in the evaluation period followed by the displacement resolution of the system during the evaluation period using Equation 43.

$$dx = \frac{\lambda}{2\pi(\min(SN))}$$ *Equation 43*

where:

dx = displacement resolution of the HQLI [nm],

λ = wavelength of the laser source [nm], and

SN = minimum signal to noise ratio that was observed during all tests [-].

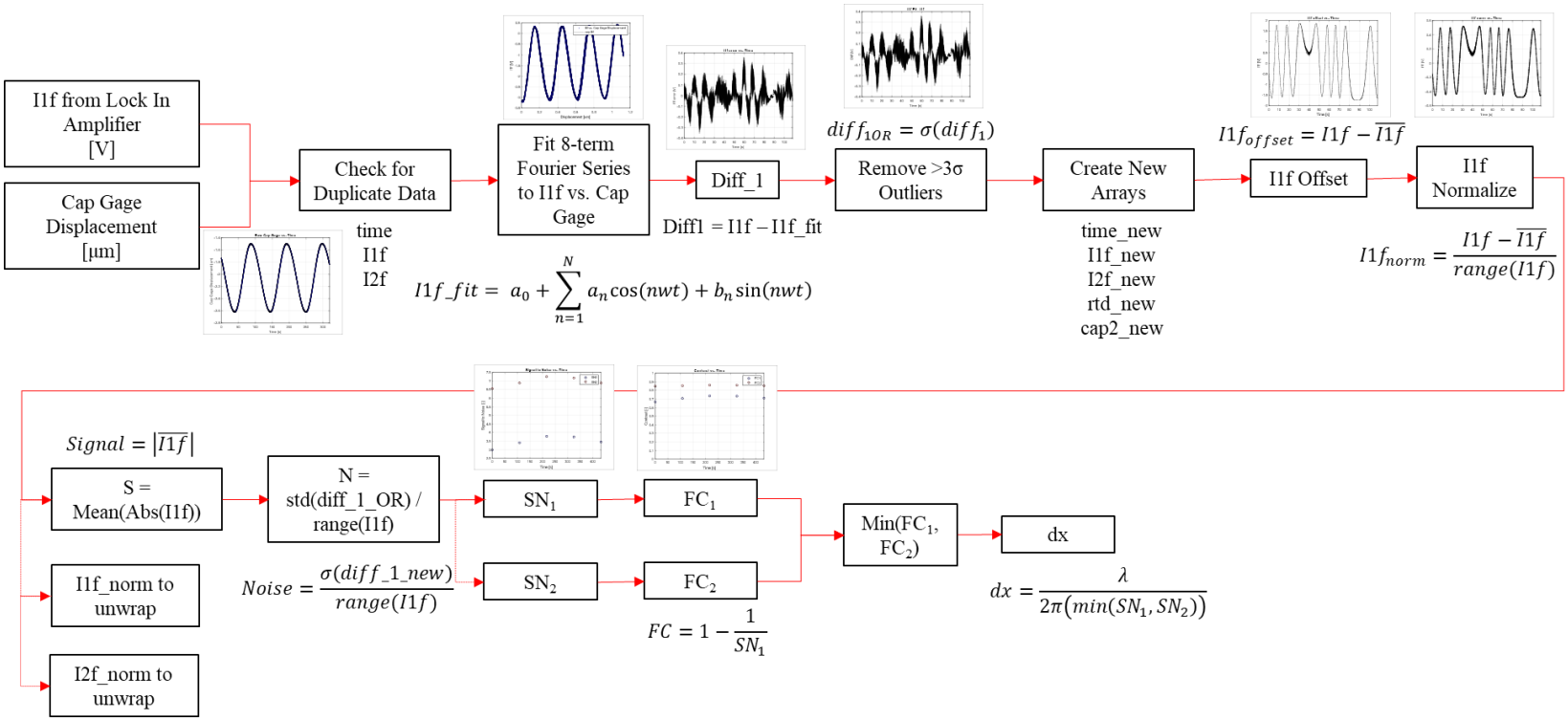

Figure 64. Flow chart for signal to noise, contrast, and displacement resolution

After the signal to noise, fringe contrast, and displacement resolution were determined, the phase unwrapping and displacement calibration routines were performed. Two approaches were used for the calibration:

- A constant velocity of the DUT arm using a triangular wave drive signal (ramp) and position measurement of the DUT arm using a calibrated capacitance gage, and
- A sinusoidal drive signal to the DUT arm with the same calibrated capacitance gage being used as a reference.

These two approaches are unique in that the first technique utilizes a constant velocity in one direction for the HQLI to follow. Since the experiments were following the path of a PZT actuator, the hysteresis in the retract direction of the PZT needed to be ignored. For these experiments, the forward stroke of the PZT was the calibration direction and the retract stroke of the PZT was removed. The sinusoidal drive signal was chosen to evaluate the bandwidth of the system. This sinusoidal signal eliminated the complexity introduced by the need for the infinite bandwidth at the sudden directional change at each end of the constant velocity scanning cycles.

Figure 65 below shows the outline for the phase unwrapping and calibration. The I1f and I2f signals from the lock-in amplifier are reviewed for duplicate data, using the same procedure for the signal to noise ratio calculations above. The wrapped displacement was then calculated using Equation 26.

The wrapped displacement is then unwrapped by counting the number of 2π jumps in the unwrapped displacement. Each 2π jump is added to the previous value to create a smooth and continuous function that can be evaluated later. The coding that is used to unwrap the phase is included in Appendix 12. MATLAB® Program for Evaluating HQLI. The unwrapped displacement (or phase) versus the capacitance gage displacement is shown below in the bold red

box in Figure 65 below. A sample calibration plot of the HQLI displacement versus the capacitance gage displacement is also shown in Appendix 6. Sample Calibration Plot for HQLI Displacement vs. Capacitance Gage Measurement.

The capacitance gage and the unwrapped phase are then shifted to be symmetric about the x-axis using the same equation that was used in the signal to noise calculation (Equation 37) but with the capacitance gage and the unwrapped phase values. The difference between the capacitance gage and the unwrapped phase was then calculated using Equation 44.

$$Diff_1 = HQLI_2 - CAP_2$$ *Equation 44*

where:

$Diff_1$ = difference in the unwrapped phase value and the capacitance gage measurement [μm],

$HQLI_2$ = measured value of the unwrapped phase [μm], and

CAP_2 = measured value of the reference capacitance gage [μm].

The outliers were then removed from $Diff_1$ and new arrays were calculated. An eight term Fourier series was fitted to the $HQLI_2$ versus time using the same fitting equation as Equation 35. This new $HQLI_3$ was plotted against the reference capacitance gage. If there is perfect agreement, the slope of the fitted line should be one. At this point in the analysis, two methodologies can be followed.

The first evaluation is used to determine overall system accuracy. This takes into account the above-mentioned hysteresis in the PZT actuator and does not discard the retract path. The difference between the capacitance gage and $HQLI_2$ is plotted on the y-axis and the capacitance gage is plotted on the x-axis. The result in this plot is a rotated difference plot showing the

overall system accuracy. A linear fit, $(y = mx + b)$, is performed, the difference plot is rotated, and the overall range of the difference in the rotated data is the system accuracy.

The second evaluation is to determine the best estimate of the repeatability of the system if all parameters are considered. Following the fitting of the Fourier series to $HQLI_2$, the top 20% of the displacement values are removed due to the infinite bandwidth that occurs at the sudden directional change when using the triangular drive signal (ramp). The rising slope of the new arrays are chosen and a linear fit $(y = mx + b)$ is performed to the displacement values. The difference plot following this step produces a polynomial type residual. A third order polynomial equation, see Equation 45, is then fitted to the second difference plot for both the $HQLI_3$ and the CAP_3.

$$y = p_1x^3 + p_2x^2 + p_3x + p_4 \qquad \textit{Equation 45}$$

The difference between the new HQLI and CAP signal is then determined ($Diff_4$). At this point, corresponding to the completion of all steps shown in Figure 65, there should be a largely random scattering of residuals. The cumulative differences are compiled into a new array across the complete evaluation period. Again, these complete periods range from 5 min to over 48 hrs. The resulting standard deviation of the cumulative difference is the best estimate of the measurement error.

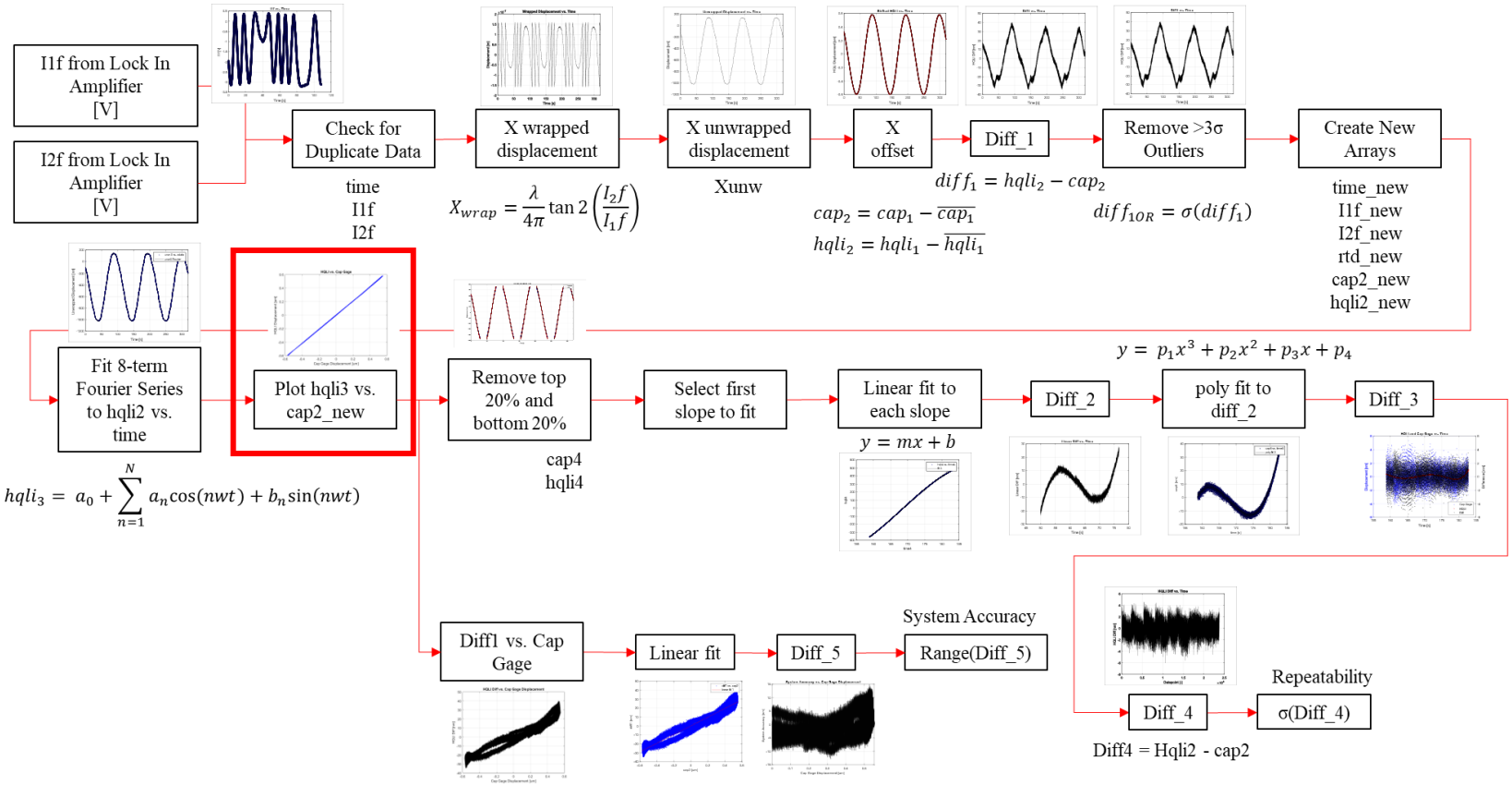

Figure 65. Flow chart of the displacement algorithm

3.1.9. HQLI RESULTS

The test results presented in this section are broken down into five categories: stability, accuracy, repeatability, overall measurement range, and bandwidth. Numerous tests (more than thirty-seven in total) have been conducted and evaluated to determine the parameters for these results.

- Stability refers to the amount of time the HQLI maintains a fringe contrast greater than 0.60 and can thus reliably unwrap phase during a specified testing period.
- Accuracy (potential) refers to the RMS deviation of the final calibration across a specified set of measured data against a calibrated capacitance gage.
- Repeatability refers to the current best estimate of the positional deviation of the unwrapped and fitted displacement measurement during a specified testing period.
- The overall measurement range is the minimum to maximum distance between the end face of the fiber and the surface of the DUT mirror while maintaining contrast.
- Bandwidth is the maximum fringe (displacement) velocity the system can measure and maintain acceptable fringe contrast, better than 0.60.

There is currently a standard in draft form, ASME B5.64 – Methods for the Performance Evaluation of Single Axis Linear Positioning Systems, that will help define the characteristics of these types of stages and displacements later. At the time of this writing, only committee members have access to the draft version.

The overall stability of the HQLI is an important parameter that will help define the ease of integration and use as a metrology system. If an HQLI system has poor stability, the measurement uncertainties will be outside of specified performances if there are extended time periods involved in the testing. Typically, stability is used to determine the time period between re-calibrations. This must extend beyond the relatively long times dictated by the time constants

of the thermal actuator. Typically, the millimeter size thermal actuator bandwidth is low (as compared to voice coil drives, servo motors, etc.) and the actuation time could be several minutes depending on the total required displacement. In the current literature (Elezov 2018) reported 200 s as the limit for phase stability. For these reasons, the HQLI has a target fringe contrast stability of greater than 300 s.

During the stability tests, the DUT drive signal is a sine wave with an amplitude of approximately 1 μm (2 μm total displacement) and a frequency of 0.009 Hz (a little less than a 2 min time period). The MOD drive signal is the 2.5 kHz signal from the lock-in amplifier with the controller running in open loop and an offset of zero, thus resulting in the lock-in signal being the only component of the drive signal. The depth of the modulation is approximately 150 nm. The average temperature of the laboratory during the experiments was 21.3°C with a typical total range of 0.05°C over a two-hour evaluation period.

The minimum fringe contrast during the two-hour evaluation was 0.755 and can be seen below in Figure 66, and the HQLI was able to maintain this contrast stability for the complete two-hour evaluation period.

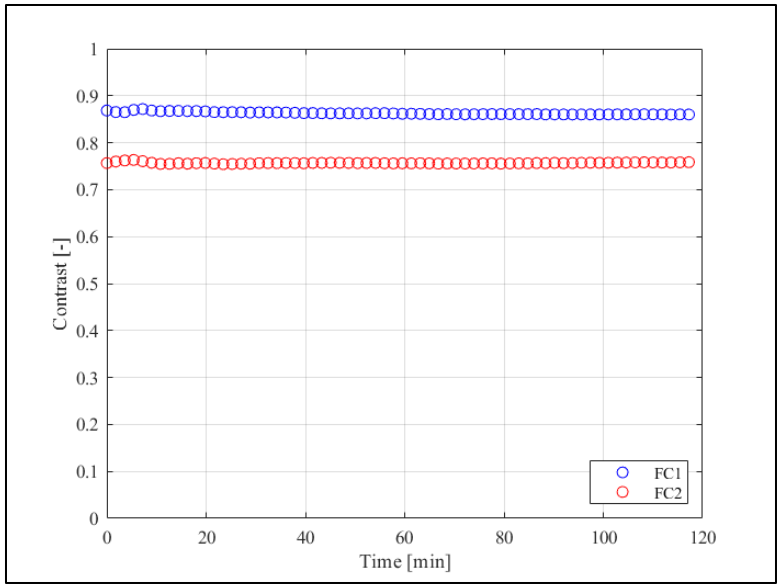

Figure 66. Contrast vs. time for stability test 402

The normalized Lissajous figure for the I1f and I2f during this same period is also plotted below in Figure 67. From this view, the width of the normalized Lissajous shows the noise of the I1f and I2f signals over the two-hour evaluation time. The average radius in the x-axis and the y-axis shows the normalized I1f and I2f signals over the same two-hour evaluation time. To create the chart in Figure 66, data similar to Figure 67 was collected for each cycle (0.009 Hz) and integrated over the complete evaluation period.

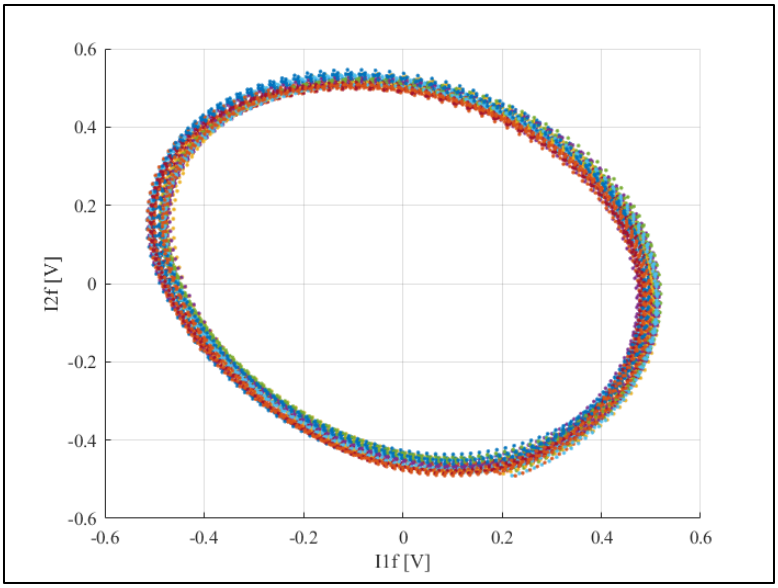

Figure 67. Lissajous of I1f and I2f for stability test 402

Using Figure 67, the displacement resolution can be determined using Equation 43 above in Section 3.1.8. Each of the colors shown in the graph correspond to a different loop, ten loops in total for the graphs shown. Table 4 below shows the displacement resolution results for seventeen tests. The main difference in the tests is the drive signal for the DUT arm. Seven tests are performed with a triangular wave and ten tests are performed with a sinusoidal wave. The triangular wave drive signal had an amplitude of 1 μm and a drive frequency of 0.009 Hz, just like the sine wave signal. Overall, the system has an approximate 30 nm displacement resolution, independent of the DUT arm PZT drive shape.

Table 4. Average displacement resolution results

Drive Signal Wave Type	Number of Tests	Average Displacement Resolution [nm]
Triangular	7	25
Sinusoidal	10	30
Combined	17	28

A so-called 3-D tornado plot that uses Figure 67 and plots it against time can be useful in showing the behavior of the system over time. Figure 68 below shows I1f on the x-axis, I2f on

the y-axis, and time on the z-axis. If the system is stable, the tornado will look like a perfect cylinder. If there is instability in the system, there could be either lateral excursions in the x-axis or y-axis or a change in the radius of the I1f or I2f. Either of these would indicate some level of instability in the system that should be addressed.

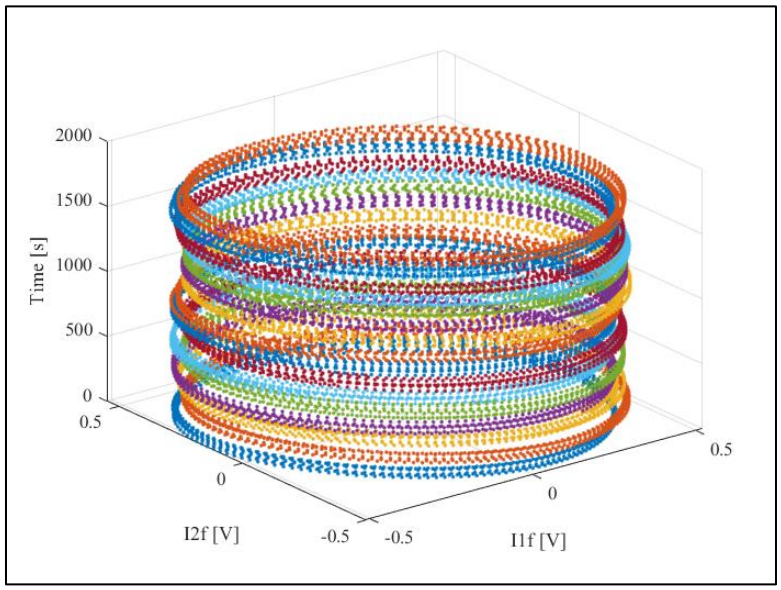

Figure 68. Tornado plot of above figure

Six additional stability tests were conducted with an evaluation time of 30 min. The average minimum fringe contrast during these six tests was 0.755. An example of the data for one specific test can be seen below in Figure 69, Figure 70, and Figure 71.

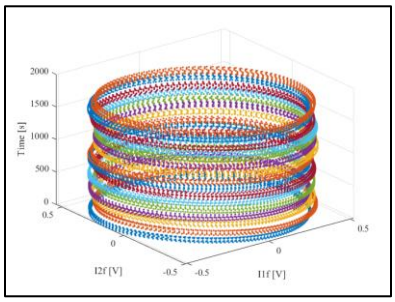

Figure 69. Tornado plot of 30 min. stability test

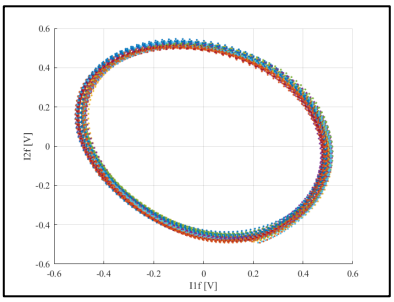

Figure 70. Top down view of tornado plot for 30 min. stability test

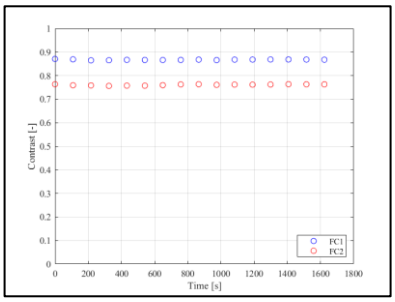

Figure 71. Contrast vs. time plot for 30 min. stability test

One additional long term stability test was performed and the fringe contrast vs. time plot can be seen below in Figure 72. Following the initial drop in stability, the system was stable for approximately 16 hrs. A second test for this length of time was not undertaken.

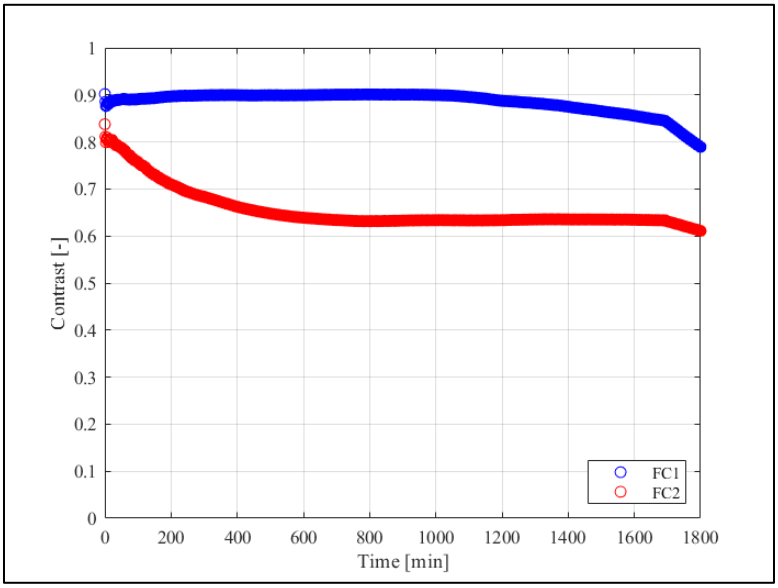

Figure 72. Contrast vs. time for 30 hour stability test

As was mentioned in the Algorithms section above, the overall system accuracy of the HQLI comprises the interferometer, the hysteresis of the PZT actuators, and the environmental impacts of the laboratory. Taking these parameters into account, the overall system accuracy can be determined from the measurement data. Seventeen tests were performed to determine the overall system accuracy (the same tests that were outlined previously in the displacement resolution section). Seven tests were completed with a triangular drive signal on the DUT arm PZT and ten tests were completed with a sinusoidal drive signal on the DUT arm PZT. Table 5 below outlines the results of these tests. The results using the triangular drive signal are worse than the sinusoidal drive signal possibly due to the sharp change in direction of the PZT and the bandwidth limitations of the HQLI at that specific moment, see Figure 73 below. Note from the Algorithms section, the explanation of dropping the top and bottom twenty percent of the

measurement data to evaluate the large deviations observed in Figure 73 below. The sinusoidal drive signal provides a more smooth, continuous change in direction for the PZT actuator and improved accuracy, see Figure 74 below.

Table 5. Average system accuracy results

Drive Signal Wave Type	Number of Tests	Average System Accuracy [nm]
Triangular	7	228
Sinusoidal	10	87
Combined	17	145

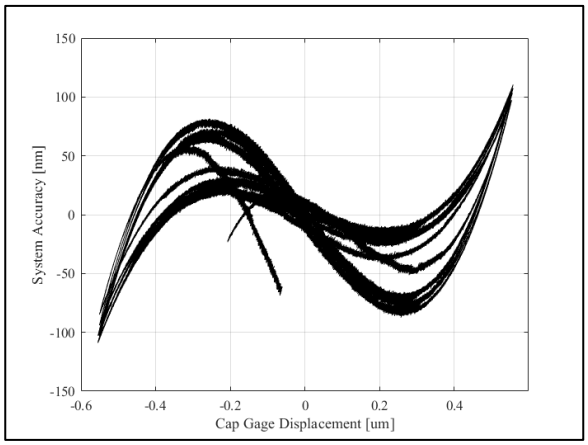

Figure 73. Triangular wave system accuracy plot

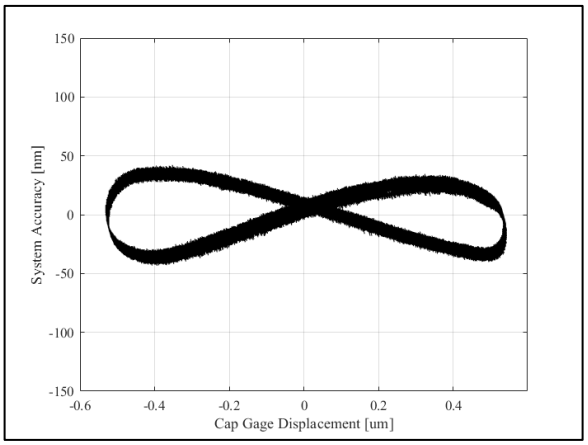

Figure 74. Sinusoidal wave system accuracy plot

The repeatability of the HQLI is the best estimate of the measurement error. In these results, this is the final RMS value of the cumulative noise after all calibration steps have been calculated at the end of the complete evaluation period. This cumulative noise is used to represent the average system repeatability. The same seventeen tests are used to evaluate the drive signals as was performed in the system accuracy tests. The results in Table 6 show the triangular drive signal having a slightly worse system repeatability than the sinusoidal drive signal.

Table 6. Average system repeatability results

Drive Signal Wave Type	Number of Tests	Average System Repeatability [nm]
Triangular	7	2.9
Sinusoidal	10	1.3
Combined	17	2.0

Figure 75 and Figure 76 show the final cumulative noise plot for the test with the triangular wave and the sinusoidal wave. The overall system repeatability is approximately 3 nm independent of the type of input signal driving the DUT arm PZT actuator.

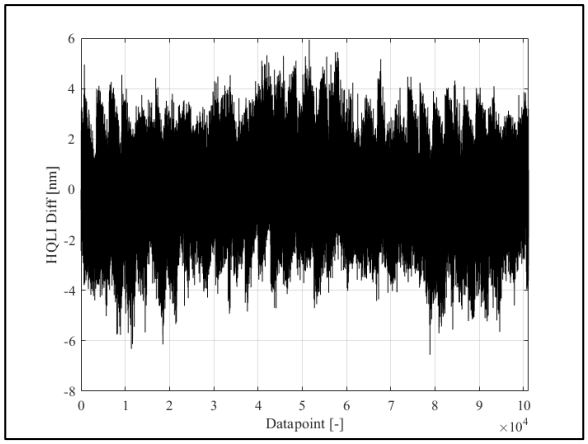

Figure 75. Triangular wave system repeatability plot

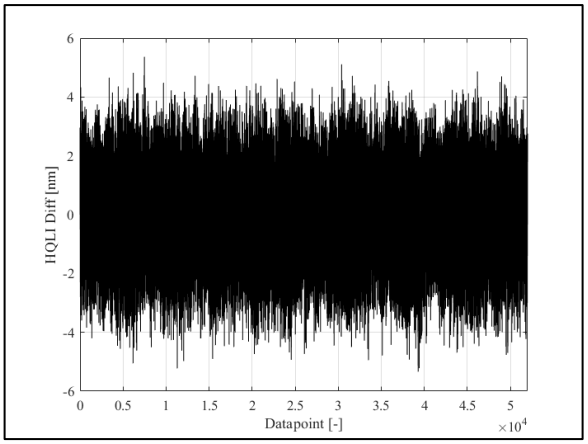

Figure 76. Sinusoidal wave system repeatability plot

The overall operating range of the HQLI was also evaluated. The fiber end face was moved from its closest position to the mirror (2.89 mm) to the position where the fringe contrast was lost. The total operating range of the HQLI was tested from 2.89 mm to 3.05 mm away from the mirror. Figure 77 below shows the results of the range testing. After 3.05 mm, the fringe contrast drops and there is no observable quadrature. This could be due to the poor coupling of the reflected beam coming back to the fiber as was discussed in the 2.1.1. Modeling The Coupling Efficiency of Bare Fiber section. The two dots on the left side show the return to approximately the same fringe contrast at the end of the evaluation period. Note, there was an

operator present during the complete time during this test. The average value of the fringe contrast at 3.05 mm is consistent with the average fringe contrast during the other seventeen accuracy, repeatability, and resolution tests – 0.745 vs. 0.728.

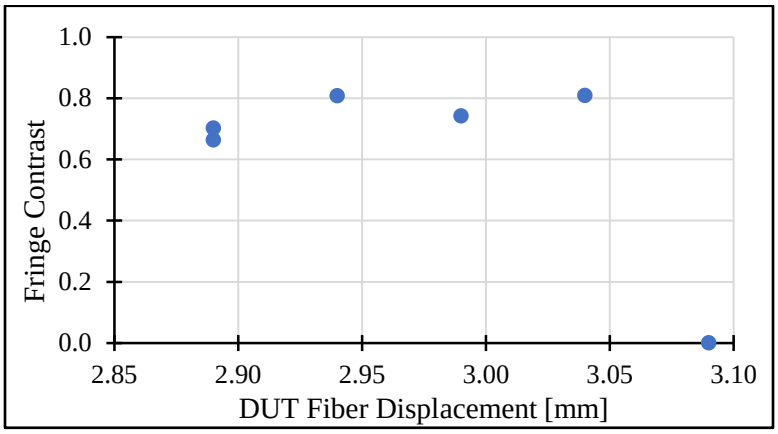

Figure 77. Fringe Contrast vs. DUT fiber displacement

The last series of tests performed were to evaluate the bandwidth of the HQLI. The bandwidth is the maximum fringe velocity that the system can measure. A minimum of ten data points per fringe is considered a minimum for characterization of a single fringe. Three different fringe velocities were evaluated- 0.25 fringe·sec^{-1}, 0.63 fringe·sec^{-1}, and 1.26 fringe·sec^{-1}. These fringe velocities relate to the DUT arm PZT actuator's peak to peak drive amplitude, 2 µm, 5 µm, and 10 µm, with a drive frequency of 0.009 Hz for all amplitudes.

Table 7. Bandwidth testing results

Fringe Velocity [fringe·sec^{-1}]	DUT arm PZT Displacement [µm]	Minimum Fringe Contrast [-]	Displacement Resolution [nm]	System Accuracy [nm]
0.25	2	0.728	28	145
0.63	5	0.460	55	200
1.26	10	Not observable	N/A	N/A

Table 7 above shows the results for the bandwidth testing. The displacement resolution does get worse as the fringe velocity increases. The limitation of the system is dominated by the time

constant of the lock-in amplifier (currently set at 50 ms for 2 μm and 5 μm displacement, and 10 ms for 10 μm displacement). One additional factor that can contribute to this is the data saving feature in the LabVIEW® program. The program loop can run faster, but the data being saved to the USB drive causes a delay. This delay is a technological issue, not an optical issue, and will not be present when the system is operating fully with LabVIEW® and may result in the bandwidth of the system being increased.

3.2. THERMAL ACTUATOR

3.2.1. OPEN LOOP TESTING

Open loop testing of the thermal actuator was completed using the smaller ZVS induction heater circuit and a 120 W power supply (12 V, 10 A). Figure 78 below shows the clamp on oscilloscope probe around one leg of the induction coil and the voltage probe across the induction coil. Figure 79 shows the complete electrical setup for the open loop testing which includes a myRio, motor controller board, smaller ZVS circuit board, and the 120 W power supply.

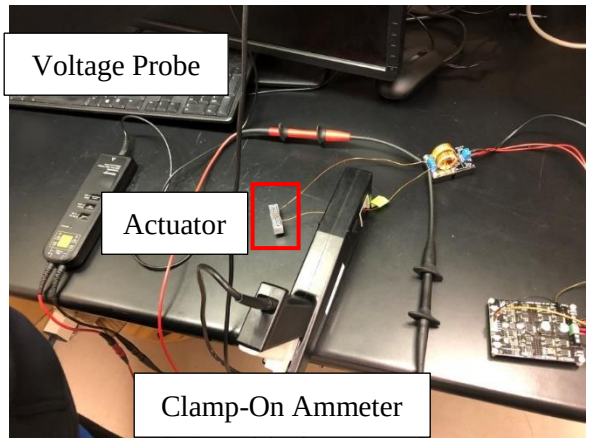

Figure 78. Open loop testing of the compact thermal actuator, oscilloscope setup

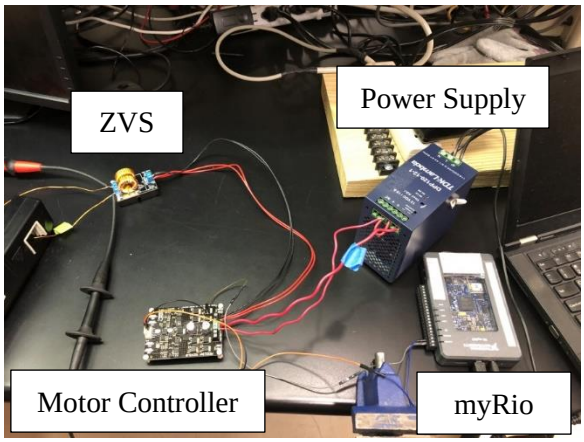

Figure 79. Open loop testing of the compact thermal actuator, electrical setup

The myRio is used to provide a PWM signal to the motor controller board. The motor controller board controls the ZVS circuit that is connected to the thermal actuator (enclosed in the red box

in Figure 78). Figure 80 shows the screen of the oscilloscope (Tektronix MDO3024) during one of the testing runs. The top yellow and cyan plots show the captured signals during the entire test. The bottom yellow and cyan plots show the detail in the region of interest (ROI) selected by the brackets in the top plot. Thus, the yellow line represents the current probe and the cyan line represents the voltage probe close to the end of the testing period. From these measurements, the measured current was 68 A, the voltage across the coil was approximately 63 V, and the operating frequency of the output of the ZVS circuit was 205 kHz.

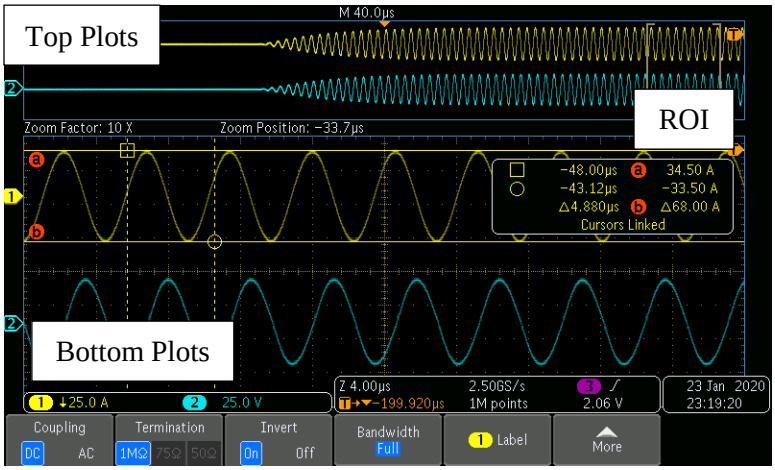

Figure 80. Oscilloscope screen during open loop testing, upper two plots show the voltage and current for the complete testing period and the bottom two plots show the voltage and current for the region of interest.

A series of open loop tests were performed by varying the PWM duty cycle from 25% up to 95%. By varying the PWM duty cycle, the amount of heat input by the induction coil can be regulated. Figure 81 shows the results of these tests. Thermal time constants were estimated from Figure 81 and the results are shown below in Table 8. The single 120 W power supply does appear to be limited in its current capacity when the duty cycle is above 50%.

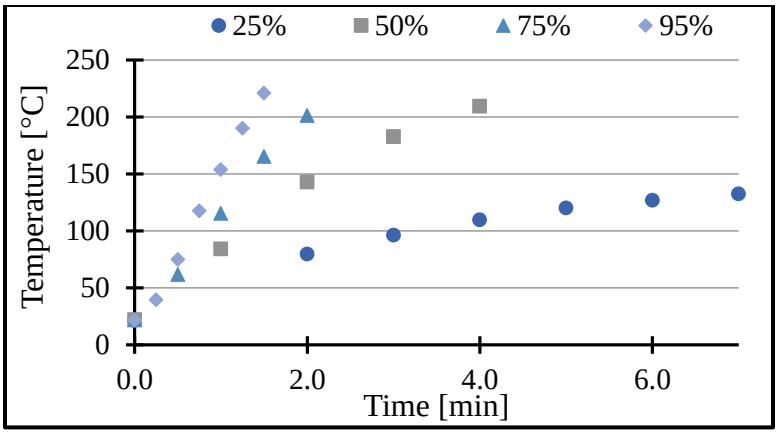

Figure 81. Open loop testing results using 120 W power supply

Table 8. Tabulated results from open loop testing

PWM Duty Cycle [%]	Estimated Maximum Temperature [°C]	Thermal Time Constant [s]
25	125	192
50	225	149
75	325	175

The coil is manufactured from a solid copper wire with insulation around the outside diameter of the wire (Section 3.2.2 outlines additional details about the induction coils). When operating at 75% and higher duty cycle, thermal degradation of the induction coil was observed as the outer insulative layer on the coils (often referred to as the lacquer coating) began to disintegrate (turn black), see Figure 82 below.

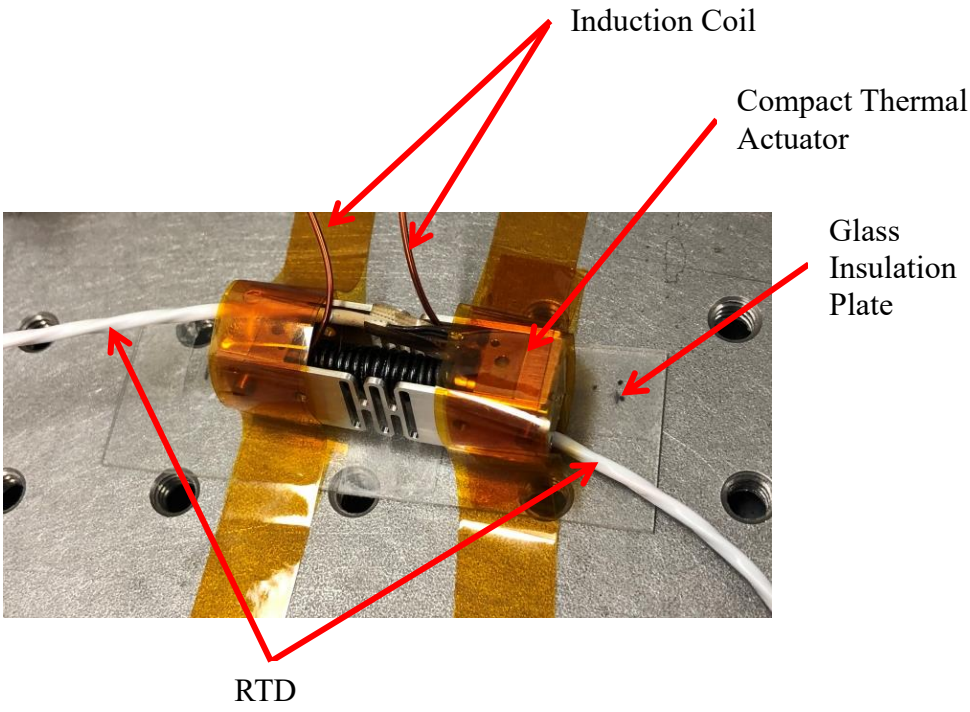

Figure 82. Compact thermal actuator after open loop testing

Following the observations of the thermal degradation of the solid copper wire, it was decided to integrate Litz wire into the design. Telephone discussions with MWS wire (Wire), a distributor of Litz wire, resulted in a recommendation of trying to use a Litz wire with 1050 strands of 44 gauge wire using single nylon serve insulation. According to literature discussing conventional and Litz wires (Wire) (Litz Wire), one of the advantages of using Litz wire is the number of strands reduces the skin effect resulting in a more uniform current distribution in the individual copper wires. With a single conductor wire, the current is concentrated at the outer periphery of the conductor. As the frequency increases, the current migrates to the outside diameter of the wire. With the 1050 strands, each strand would evenly distribute the 68 A to each strand, reducing the current each strand is carrying to 65 mA, assuming the wire is terminated correctly. With these lower currents, there is the possibility of having a reduced coil operating temperature and changing the operational characteristics of the device.

Considering termination techniques, Miller-Stephenson MS-111 was recommended as the chemical stripping agent and utilization of a solder pot for soldering the lead wires following the chemical stripping. Due to cost constraints, only a small section of this wire was able to be sourced. The Litz wire has not been tested at this point.

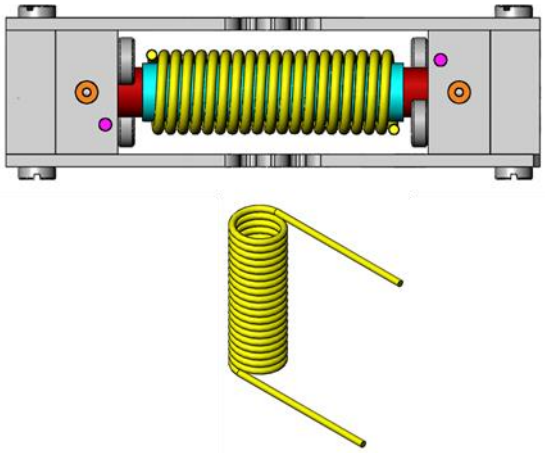

Figure 83. Thermal actuator CAD model with solid copper wire induction coil

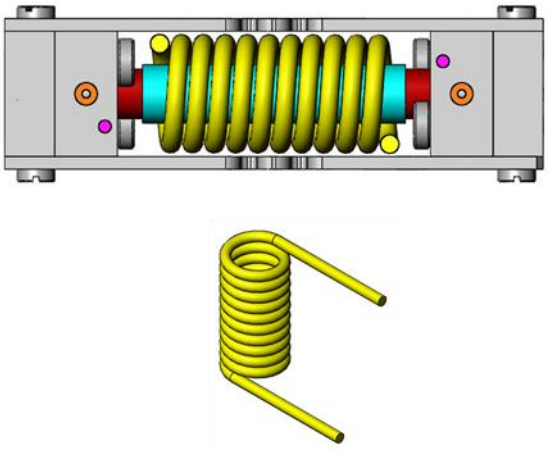

Figure 84. Thermal actuator CAD model with Litz wire induction coil

Figure 83 and Figure 84 above show the size difference in the solid copper induction coil and the Litz wire coil. Based on the space constraints, the Litz wire should work inside the thermal actuator.

3.2.2. INDUCTION COILS AND OPERATING CURRENT

Six induction coils were made from 20 gauge (outside diameter = 0.83 mm) solid copper motor winding wire. Dimensions were taken for the overall length, number of turns, inside and outside diameter of the coil, and the electrical resistance of each coil. The theoretical resistance is given by Equation 46. The calculated design resistance and the experimental measurements of each induction coil is shown in Table 9 below.

$$R_{calc} = \frac{4\rho\left(n\pi D_{coil} + l_{leg1} + l_{leg2}\right)}{\pi d_0^2} \qquad \textit{Equation 46}$$

where:

R_{calc} = calculated resistance of the induction coil [Ω],

ρ = electrical resistivity of the coil material [Ω·cm],

n = number of turns in the induction coil,

D_{coil} = mean diameter of the induction coil [cm],

l_{leg1} = length of leg one of the induction coil [cm],

l_{leg2} = length of leg two of the induction coil [cm], and

d_0 = wire diameter [cm].

Table 9. Resistance values of solid core induction coils

Coil ID	Inside Diameter [mm]	Outside Diameter [mm]	Leg 1 Overall Length [mm]	Leg 2 Overall Length [mm]	Number of Turns	Calculated Resistance [mΩ]	Measured Resistance [mΩ]
1	4.9	6.8	231	232	23.5	28.28	29.11
2	5.0	6.9	207	205	20.5	25.14	25.83
3	5.0	6.9	248	239	16.5	25.14	25.88
4	5.0	6.8	227	231	21.5	27.02	27.79
5	5.1	6.9	232	230	16.5	24.51	24.95
6	4.9	6.8	224	227	20.5	26.08	26.95

The average deviation between the calculated resistance and the measured resistance is 2.8%.

Sensing the drive current is advantageous for the thermal actuator. Current sensing was implemented by using a shunt resistor (Vishay WSBS8518L2500JK) that is in series with the induction coil when it is connected to the ZVS circuit, see red box in Figure 85 below.

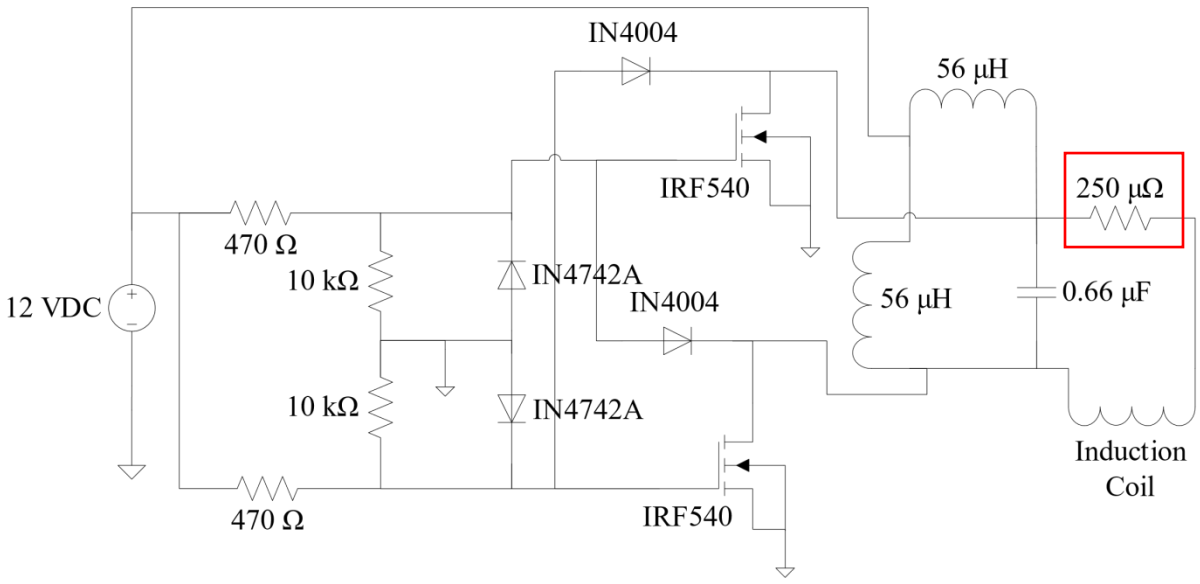

Figure 85. ZVS circuit with shunt resistor shown in line with the induction coil

To minimize the impact to the operation of the coil, a shunt resistor should be chosen that has no more than 1/100th the impedance of the coil it is measuring (Leibson). Speaking to direct current mode, the shunt resistance should be less than 270 µΩ. When operating in alternating current mode (such as the thermal actuator in final operation), the inductance of the shunt resistor has an influence as well as the ohmic resistance at high operating frequencies. The average measured inductance of the coils is 803 nH. The shunt resistor that was ultimately chosen has a resistance of 250 µΩ and an inductance of less than 5 nH, altogether providing less than 1/100th (0.0063) of the total coil impedance at the measured drive frequency.

The shunt resistor is connected with a Kelvin type connection. Two leads are connected for the source side (high power side where the main power enters and exits the resistor) and two leads for the sense side (measurement side). When testing these coils for open loop response, the current during operation ranged from 49.5 A to a maximum of 68 A. Using the 68 A current and the impedance of the shunt resistor, the estimated voltage drop across the shunt resistor is

approximately 0.5 V. Depending on which data acquisition device is used, a gain amplifier may be required to measure this signal with sufficient resolution.

3.2.3. LOAD CELL

A load cell has been implemented into the system to verify the applied load to the actuator. The large load (1000 N) compared to the small size of the actuator was a primary concern for failure, so verification of the loading was necessary. The load cell (Omega LC307-250, strain gauge type) has an operational slope of 0.0067 $mV \cdot N^{-1}$. For a load of 1000 N, the measured voltage should be approximately 6.7 mV. Figure 19 above shows the mechanical setup of the frame apparatus that houses the screw adjustment handle, compression spring, device stage, and thermal actuator.

At the time of this writing, the thermal actuator had been under a 1000 N constant load for over two months (installed April 2021). The load cell was not intended to be monitored during testing of the actuator at room temperature, but it could be if desired. At the elevated temperature, the load cell should be removed per the manufacturer's recommendations. Due to the low output voltage, an amplifier may be necessary depending on the data acquisition device selected. Additional details of the load cell are discussed in Section 5.2.

CHAPTER 4: CONCLUSIONS

This chapter details the observations and results from testing and evaluation of the HQLI and the compact thermal actuator.

4.1. HOMODYNE QUADRATURE LASER INTERFEROMETER

This thesis presents the design, construction, algorithms, and initial test results for an all-fiber homodyne quadrature laser interferometer. This system was constructed using a commercially available, fiber coupled, 635 nm laser diode as the source, a two input by two output fiber splitter, frequency modulated quadrature detection, two dielectric mirrors, and one photodetector. Novel features of this all-fiber interferometer include:

- The system has shown stability in fringe contrast with time periods of minutes up to 16 hours or more.
- Displacement resolution of approximately 30 nm with a repeatability of 3 nm.
- Operating range of 3.0 mm and a bandwidth of 0.63 fringe·sec^{-1}.
- This design is not limited to equal arm lengths for the measurement of displacement interference fringes.
- The interference measurement can be monitored from the signal from a single photodetector and the system does not require polarization maintaining fiber nor polarization splitting optics.

Special consideration has been given to the operational requirements of the system including the environmental conditions, required enclosures for thermal stability of the modulating source, and signal conditioning electronics for enhancing signal to noise in the instrumentation.

Interestingly, the displacement resolution of the system (around 30 nm) is very similar in magnitude to the thermal displacement deviation of the MOD arm mirror (30 nm due to a

temperature deviation of 0.05°C). This phenomenon should be investigated to determine if there is correlation to the MOD arm's positional deviation as a contributor to the overall displacement resolution.

4.2. THERMAL ACTUATOR

The design, construction, and limited initial testing is presented for a compact thermal actuator. This actuator can operate with a 1000 N load, operate in environments with temperatures greater than 150°C, and utilizes an integrated all-fiber homodyne quadrature laser interferometer. Because of the compact size and operating temperature requirements, it has been necessary to implement new design features not present with the early thermal actuator design. These new features are:

- Displacement measuring interferometer (HQLI).
- Litz wire to reduce overheating of the induction coils.
- High temperature compressed air cooling.
- Increased power of the induction coil drivers.

CHAPTER 5: FUTURE WORK

This chapter outlines the possible future works to the HQLI and the compact thermal actuator. Improvements in all aspects of the design, operation, and evaluation are discussed.

5.1. HOMODYNE QUADRATURE LASER INTERFEROMETER

Future work on the HQLI can cover many topics including electronics, optics, hardware, and software. From the electronics side, there is needed improvement in the overall circuit design/optimization and construction (moving from proto-boards to more final circuit boards with hardened connections), elimination of the lock-in amplifier with a digital solution (such as a LabVIEW® programmed solution), and elimination of the current photodetector amplifier with a transimpedance amplifier circuit that is not bandwidth limited.

Regarding optics, the possible use of a GRIN lens for extending the operating range by producing a collimated output at the DUT fiber has not been pursued. The addition of a fiber circulator or Faraday isolator for added stability has also not been explored at this time due to costs and availability of these components for visible light applications. Additional work into using different types of mirrors for the DUT and MOD arms to improve performance could also be investigated. With regards to the fiber coupled laser diode source, a more formal investigation into the exact wavelength of the laser source could be conducted at standard operating conditions and over long periods of operation.

With the current modulation depth, the output Lissajous figure is an elliptical shape, not circular. This is due to the Bessel function solutions where J_1 is not the same amplitude as J_2. A study should be conducted to try and achieve equal magnitudes of the J_1 and J_2 as is shown in Figure 6 in Section 2.1.2. MOD Arm Mirror by changing the depth of the modulation.

Improvements to the software can be realized almost immediately. All data is currently processed offline using MATLAB®. Given the current performance of the system, new LabVIEW® programs can be written to process the displacement data in-situ, and eliminate the save data feature currently being used. This should provide an immediate increase to the system's bandwidth.

Regarding system integration, additional testing needs to be performed with the HQLI in a controlled flow environment such that would be used in the thermal actuator application (for example, using compressed air flowing across the air gap in the DUT arm). This would provide insight into the operating characteristics of the system and future work that is required. More work is required to further develop the coating process for the glass reflection rod.

One last area that needs to be addressed is the difference in the metrology loops for the MOD arm and the DUT arm. With each of these arms being at different temperatures, there could be additional influences that are not currently observed. One possible solution is to re-work the actuator to allow a separate cooling loop inside of the actuator tube that would be able to maintain the DUT fiber and reflection rod temperature to that of approximately the same as the MOD arm. The current design may also facilitate this type of cooling, but in order to achieve a return to room temperature (20°C), the cooling media's bulk temperature will need to be lower than the 20°C. In this situation, the temperature of the MOD arm may need to be changed from 20°C to a temperature that ultimately matches the cooling media. One last consideration is the addition of a quartz crystal inside of the actuator environment. The main advantage of the quartz crystal is it is not temperature restricted like the PZT actuators. This type of quartz crystal actuator is currently being investigated in the instrument development laboratory.

5.2. THERMAL ACTUATOR

Future work of the thermal actuator will include further development of the system hardware, software, electronics, and data collection. Beginning with the hardware, there are two types of induction coils that have been discussed, solid core coils and multi-strand Litz wire coils. Limited progress has been made on the Litz wire coils. Materials and techniques have been tested for the soldering pot technique, but not tested on an actual sample. To pursue this development, more funds are required for purchasing of additional Litz wire.

The glass reflection rod will need to be ground to its overall length, polished, and coated with a high reflectivity coating. Now that the operating range of the HQLI has been determined, this work can continue. Opposite of the glass reflection rod is the fiber end face. The SM fiber will need to be terminated into the top platen of the thermal actuator using a heat cure epoxy due to the required operating temperatures. The end face of the fiber will need to be polished following the termination. No fixture designs have been initiated for this work.

Regarding software, the starting point of integrating the thermal actuator to either the knife edge sensor or the HQLI has not been completed.

Regarding electronics, the ZVS circuit has been tested on the previous thermal actuator design, but not with the compact unit. Additional power supplies may be required to optimize operation of the ZVS with the compact thermal actuator.

There are multiple sensors available for characterizing the system (load cell, temperature, fluid flow, fluid pressure) and the design and operation of those sensors will need to be evaluated. The load cell will need to be updated if loads in excess of 1000 N are to be tested.

Lastly, there is a pneumatic directional control valve that has been integrated into the system for active cooling. The operation of the pneumatics will need to be developed and

investigations will be required to determine the operational characteristics of the unit (i.e., operating at room temperature or at elevated temperatures will require different methodologies). A thermal heat sink for the compressed air cooling media may be required if operating at room temperature.

REFERENCES

Beater, Peter. *Pneumatic Drives*. Verlag: Springer, 2007. Book.

Chan, H.Y., Li, W.J. "A Thermally Actuated Polymer Micro Robotic Gripper for Manipulation of Biological Cells." *IEEE International Conference on Robotics and Automation* (2003). Document.

Dodd, C.V., Deeds, W.E. "Analytical Solutions to Eddy Current Probe Coil Problems." *Journal of Applied Physics* (1968). Document.

—. "Solutions to Electromagnetic Induction Problems." Oak Ridge, June 1967. Document.

Elezov, M.S., Scherbatenko, M.L., Sych, D.V., Goltsman, G.N. "Active and passive phase stabilization for the all-fiber Michelson Inteferometer." *Journal of Physics* (2018). Document.

Ellis, J.D. *Field Guide to Displacement Measuring Interferometry*. Bellingham: SPIE, 2014. Field Guide.

Fan, C., Hastings, D.J., Smith, S.T., Tarbutton, J.A. "Aspects of Design and Performance of a thermally actuated linear translation stage." *American Society for Precision Engineering Conference 71*. 2019. 371-374. Document.

—. "Design and control of a thermal actuation system." *American Society of Precision Engineering, Spring Topical Meeting, Volume 72*. 2020. 73-76. Document.

—. "Design and Performance of a Thermal Actuator Driving a Preloaded Linear Translation Stage." *Precision Engineering* (2021): 187-199. Document.

Fan, C., Smith, S.T., Tarbutton, J.A. "A linear positioning stage using a thermal actuator." *American Society of Precision Engineering*. 2018. Document.

Hickey, R., Sameoto, D., Hubbard, T., Kujath, M. "Time and Frequency Response of Two-Arm Micromachined Thermal Actuators." *Journal of Micromechanics and Microengineering* (2003). Document.

Hobbs, P.C.D. "Ultrasensitive Laser Measurements without Tears." *Applied Optics* (1997). Document.

Huber, J.E., Fleck, N.A., Ashby, M.F. "The Selection of Mechanical Actuators Based on Performance Indices." *Proceedings of the Royal Society of London* (1997). Document.

Juvinall, R.C., Marshek, K.M. *Fundamentals of Machine Component Design*. 4th. Hoboken: John Wiley and Sons, Inc., 2005. Book.

Lawall, J., Kessler, E. "Michelson Interferometry with 10 pm Accuracy." *Review of Scientific Instruments* (2000). Document.

Leibson, S. *Fundamentals of Current Measurement*. 09 10 2018. Document. 30 06 2021. <https://www.digikey.com/en/articles/fundamentals-of-current-measurement-part-1-current-sense-resistors>.

Li, L., Uttamchandani, D. "Dynamic Response Modelling and Characterization of a Vertical Electrothermal Actuator." *Journal of Micromechanics and Microengineering* (2009). Document.

Lin, F., Smith, S.T., Ghazanfar, H. "Optical fiber displacement sensor and its application to tuning fork response measurement." *Precision Engineering, 36h Edition*. 2012. 620-628. Document.

Litz Wire. n.d. Website. 30 06 2021. <https://www.newenglandwire.com/service/litz-wire/>.

Liu, Z., Zhong, Q., Yu, X., Wang, Q.J., Zhang, Y. "High-resolution Fiber Profilometer for Hard-to-Access Areas." *Applied Optics* (2015). Document.

Lu, C., Zhou, K. "A Low Cost All Digital Demodulation Method for Fiber Optics Interferometric Sensors." *Measurement Science and Technology* (2018). Document.
McGivern, K.G. *When to Use Litz Wire*. n.d. Website. 28 06 2021.
Nowakowski, B.K., Smith, D.T., Smith, S.T. "Highly Compact Fiber Fabry-Perot Interferometer: A New Instrument Design." *Review of Scientific Instruments* (2016). Document.
Optics, Edmund. *Gaussian Beam Propagation*. 2021. Website. 29 06 2021.
Pratt, P.R., Wilkinson, J.R. "Analytical Model for Low Finesse, External Cavity, Fiber Fabry-Perot Interferometers Including Multiple Reflections and Angular Misalignment." *Applied Optics* (2011). Document.
Smith, S.T., Seugling, R.M. "Sensor and actuator considerations for precision, small machines." *Precision Engineering, 30* (2006): 245-64. Document.
Synder, J.J. "Accurate, Inexpensive, Thermal Expansion Microtranslator." *Review of Scientific Instruments* (1993). Document.
Thorlabs. *https://www.thorlabs.com/newgrouppage9.cfm?objectgroup_id=949&pn=SM600*. 2021. Website. 30 06 2021.
Wire, MWS. *Litz Wire*. n.d. Website. 30 06 2021. <https://mwswire.com/specialty-wire/litz-wire/>.

APPENDIX 1. GRINDING GLASS PLATES AND REFLECTION RODS

The need to grind the reflection rods to an accurate overall length necessitated the need to learn how to creep feed grind glass materials using a manual surface grinder outfitted with flood coolant and an approximately 1 mm thick diamond wheel with special spacers for mounting the wheel to an arbor for the particular surface grinder. A technique called "waxing in" was used to secure the substrate to be ground to a sacrificial piece of float glass.

The equipment used in these tests included an Okamoto surface grinder, Norton diamond wheels, various arbor spacers, optical wax, and various pieces of glass for fixturing and testing. The Okamoto surface grinder was outfitted with flood coolant, Walker electromagnetic chuck, maximum 8 inch diameter by maximum 1 inch thick wheel, and rotated at 8000 sfpm. Two Norton diamond wheels were tested, a resin bonded wheel (69014192099) and the other a metal bonded wheel (K0545909). Both wheels were approximately 1.00 mm thick, 100 grit, and have an inside arbor diameter of 1.25 in. Various thickness spacers were also used to adapt the diamond wheels to the arbors of the surface grinder. The dimensions of the arbors are shown below in Table 10.

Table 10. Arbor spacer dimensions for use with the diamond wheels

Spacer ID	Inside Diameter [mm]	Outside Diameter [mm]	Thickness [mm]
1	31.87	61.7	12.50
2	31.78	61.8	12.80
3	31.78	61.8	12.18
4	32.68	62.7	1.29

Using the arbor for the surface grinder, the spacers above, one of the diamond wheels were assembled and prepared for use on the surface grinder, Figure 86 and Figure 87 below.

Figure 86. Top view of metal bonded diamond wheel mounted in arbor.

Figure 87. Front view of metal bonded diamond wheel mounted in arbor.

South Bay Technologies MWM070 optical wax was used to secure the substrate microscope slides to a sacrificial piece of float glass underneath. There are different types of waxes for different applications, soft wax, hard wax, low melting temperature, high melting temperature, etc. Some manufacturers and different types of optical wax are:

- Crystalbond 509 - https://www.2spi.com/item/z05110/
- South Bay Technology - http://www.southbaytech.com/consum2.shtml#mw
- Reed Wax - http://www.reedwax.com/waxcom.htm
- Ted Pella - https://www.tedpella.com/Material-Sciences_html/PELCO-Mounting-Waxes.htm

A hot plate is used to preheat the materials to approximately 100°C in order to apply the wax between them. A 1-2-3 block is used to align the edges of the float glass to the microscope slide (Figure 88) during application of the wax.

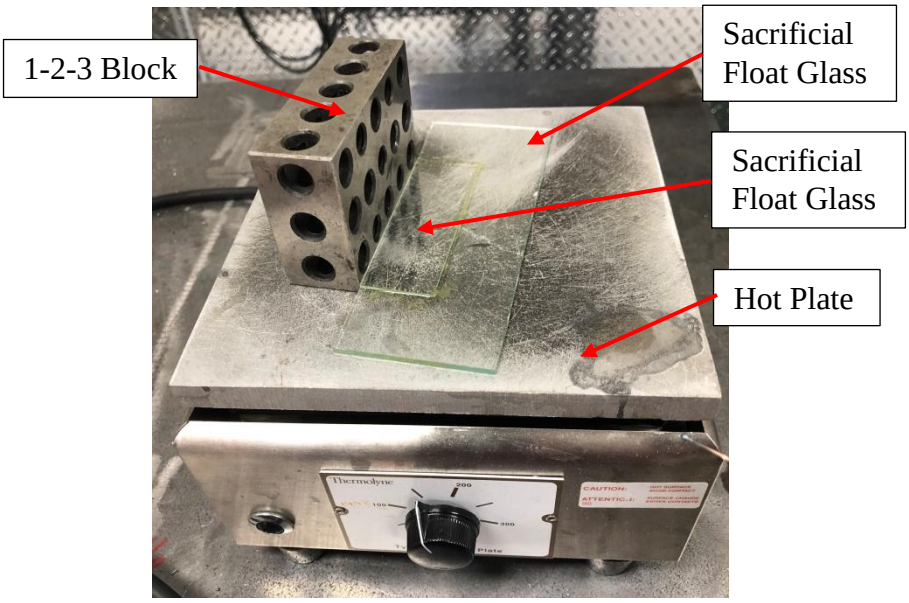

Figure 88. Hot plate with float glass underneath and microscope slide on top.

The float glass and microscope slide were then waxed down to a steel base plate using the same procedure as above with the hot plate and 1-2-3 block. The steel base plate was required to hold the complete assembly in place on the electromagnetic chuck. Figure 89 below shows the different materials setup on the magnetic chuck.

Figure 89. Steel block, float glass, and microscope slide waxed down on magnetic chuck, ready for creep feed grinding.

Flood coolant was used to cover both sides of the grinding wheel during operation (see Figure 90 and Figure 91 below). The wheel was dialed in to maximum depth (maximum depth was obtained by touching off on just the top surface of the float glass and then adding approximately 0.1 mm past that touch off) and was hand fed into the microscope slide at a consistent, slow, feed rate. The required time to dice the full width of the float glass and the microscope slide was approximately 5-6 min per cut. Given the width of the float glass being ~45 mm, the average velocity for cutting across the width of the glass was 8 $mm \cdot min^{-1}$. The audible sound produced during the cut was used as feedback to the grinder operator to monitor the operation. The metal bonded wheel had a higher volume of feedback in this normal operation mode than the resin bonded wheel.

Figure 90. Flood coolant during operation, front view.

Figure 91. Flood coolant in operation, rear view

After the grinding wheel was fully traversed across the microscope slide, it was returned to the original starting position and positioned for another cut. Figure 92 below show the sample after being removed from the magnetic chuck. After the steel block and glass materials are finished grinding, the assembly is removed from the surface grinder and the coolant is cleaned from the assembly. The assembly is then placed back on the hot plate (temperature set at 100°C) and the components are separated once the wax reaches the 70°C. Figure 93 shows the sample after the

wax is removed, the individual component is removed from the float glass, and then the edges of the component are ready for deburring using a diamond file (if needed). Either isopropyl alcohol or acetone can be used as a cleaning agent once the individual parts are separated.

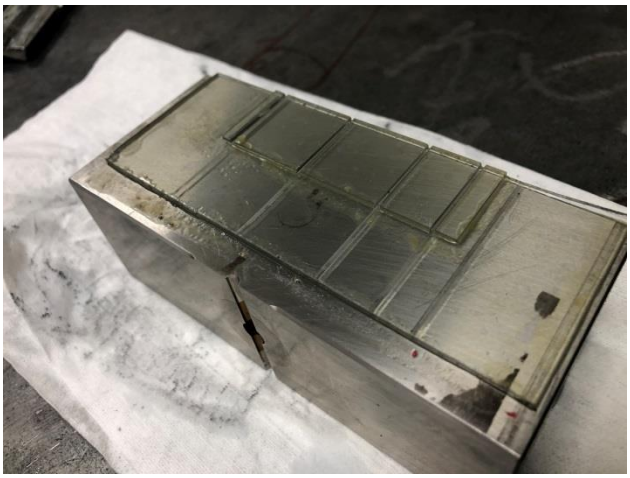

Figure 92. Workpiece after grinding multiple times and before wax is removed.

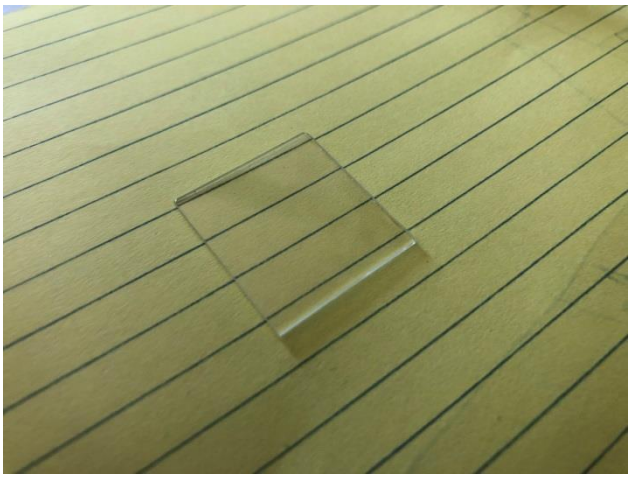

Figure 93. Single microscope slide after grinding and wax removed.

The edge quality of each type of wheel was viewed at 100X magnification without using a diamond file for deburring. Figure 94 and Figure 95 below show the results from each wheel.

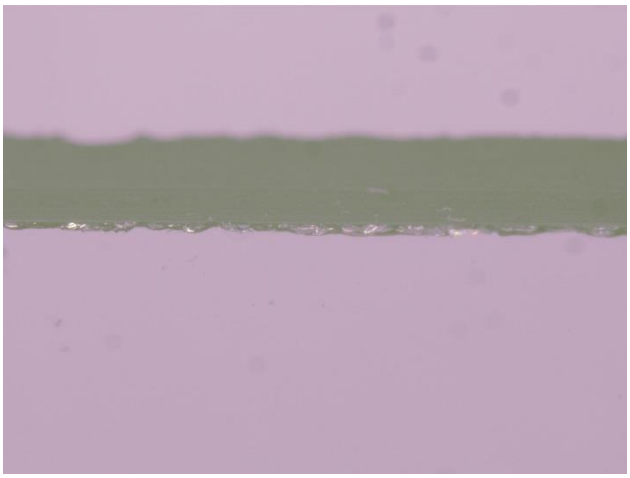

Figure 94. Edge quality of metal bonded wheel, 100X magnification

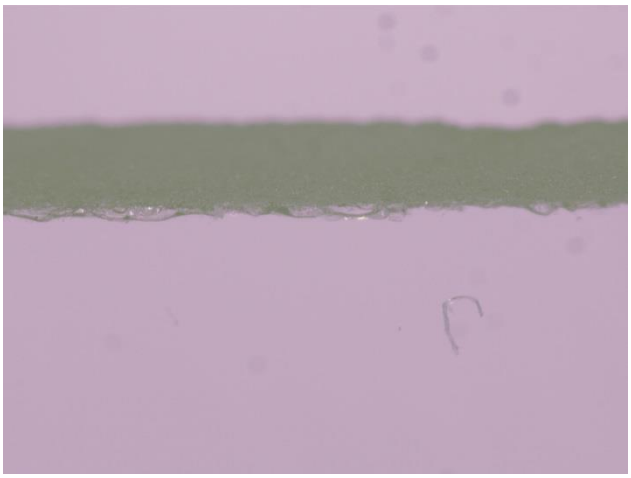

Figure 95. Edge quality of resin bonded wheel, 100X magnification

The need to grind a Ø1.000 mm diameter glass rod to an overall length of approximately 34.40 mm (the nominal overall length is 33.800 mm but the extra length allows for polishing the end

face of the reflection rod and then a subsequent dielectric high reflectivity coating to be applied) is the purpose of the above experiment. The fixturing for grinding the glass reflection rods was then designed and implemented. Figure 96 shows the CAD design with the microscope slide shown in magenta, the reflection rod in cyan, the float glass in gray, and the steel block in blue. A standard microscope slide was ground along its length with two slots, as can be seen in Figure 97. The width of the slot will accommodate the outside diameter of the reflection rod without needing a second pass. The reflection rod will be placed into the slots in Figure 97 and waxed down using the techniques from above. The steel block will then be fixtured on the magnetic chuck with its short axis perpendicular to the direction of motion.

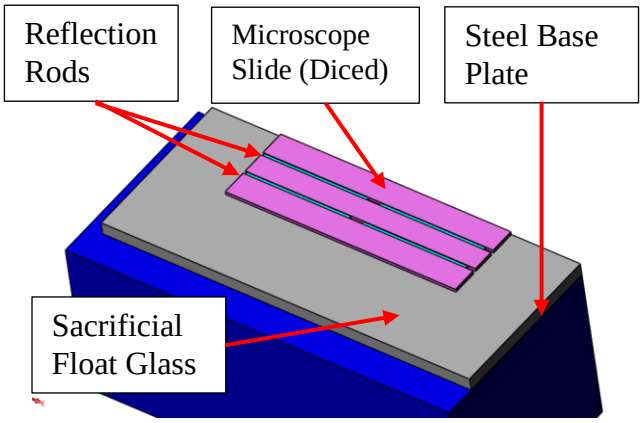

Figure 96. CAD design of grinding fixture for reflection rods.

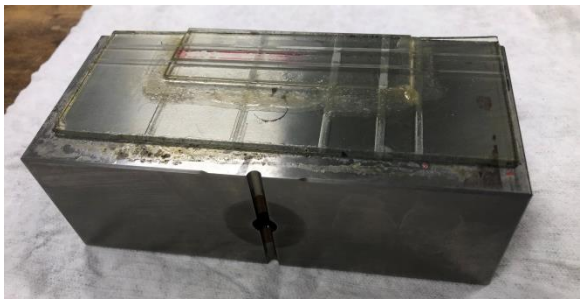

Figure 97. Implementation of grinding fixture for reflection rods.

Using the pervious experiment with the microscope slides, the thickness of the two diamond wheels was determined to be approximately 1.000 mm. Four reflection rods can be machined at one time using this technique. At the time of this writing, the final grinding of the reflection rods had not been completed.

APPENDIX 2. ELECTRICAL SCHEMATIC FOR SIGNAL CONDITIONING ELECTRONICS

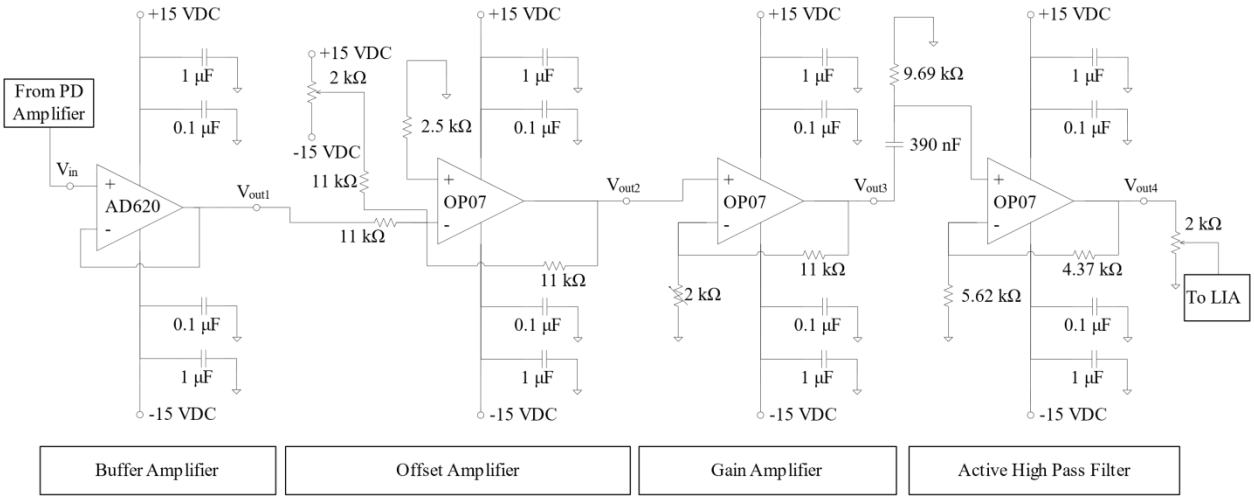

Figure 98. Electrical schematic for signal conditioning electronics

Initially, the signal from the PD amplifier is sent to the AD620 instrumentation amplifier connected in a buffer configuration. The output voltage from the PD amplifier can be between 0-10 V. The power supply rails of the amplifiers will all need to be above this value to maximize the final output voltage. Since the AD620 is connected as a buffer, the input voltage from the PD amplifier, V_{in}, will be the same as the output voltage of the buffer, V_{out1}, ideally. V_{out1} is then fed into the offset amplifier.

The purpose of the offset amplifier is to remove the high DC offset voltage that is present in the signal from the PD amplifier. The DC offset from the PD amplifier can range from 2 V up to 10 V. The output voltage, V_{out2}, can be set by adjusting the 2 kΩ potentiometer that is connected to the ± 15 V power supply. The offset amplifier is built essentially as a summing amplifier. The equation for the output voltage of the offset amplifier is the summation of the voltage from the 2 kΩ potentiometer plus the V_{out2} since all three resistors are equal (11 kΩ).

Following the offset amplifier is the gain stage. The gain stage multiplies the output from the offset amplifier, V_{out2}, by a gain factor, G. In the current configuration, the gain is adjustable via a 2 kΩ potentiometer in the bottom left corner of the gain stage, enabling the output voltage to be maximized to almost the full rail range, ±15 V. The equation for the gain of the gain amplifier is:

$$G = 1 + \frac{11k\Omega}{R_{2k\Omega\_Pot}} \qquad \textit{Equation 47}$$

where:

G = Gain of the amplifier [$\Omega \cdot \Omega^{-1}$],

$11k\Omega$ = Resistance of the feedback resistor [Ω], and

$R_{2k\Omega\_Pot}$ = Resistance of the potentiometer [Ω].

The last stage is a first order, buffered, active high pass filter. The purpose of this filter is to remove any remaining DC offset and only allow signals with a frequency content of greater than 42 Hz to pass through with an attenuation of -3 dB. The gain of this stage is approximately 1.78 and follows the same equation as Equation 47, but with different resistor values:

$$G_{HPF} = 1 + \frac{4.37k\Omega}{5.62k\Omega} \qquad \textit{Equation 48}$$

The frequency response of this type of high pass filter is the same as a passive high pass filter. The cutoff frequency of the filter was chosen such that:

$$f_c = \frac{1}{2\pi RC} \qquad \textit{Equation 49}$$

where:

f_c = 42 Hz

R = 9.69 kΩ, and

C = 390 nF.

Due to the active high pass filter having gain, the typical voltage drop that is observed in a passive high pass filter is not seen in the output voltage of the active high pass filter. This is an important consideration for the signal conditioning electronics such that the voltage being supplied to the lock-in amplifier can be maintained at a higher amplitude than was originally observed in the PD amplifier.

Following the high pass filter is a potentiometer that is configured as a voltage divider to decrease the output voltage of the high pass filter to a level the lock-in amplifier can accept without being overloaded. The output voltage of the high pass filter is connected to one of the fixed legs of the potentiometer and the second fixed leg of the potentiometer is tied to the 0 V reference. The armature of the potentiometer is connected to the lock-in amplifier and is able to be adjusted such that the input voltage can be maximized to the lock-in amplifier.

APPENDIX 3. LOCK-IN AMPLIFIER SETTINGS

Table 11 below shows the settings for the Ametek 7270 DSP Lock-In Amplifier that were used to obtain the results shown in Section 3.1.9. HQLI Results. At the time of this writing, the operating manual for this instrument was available at the following: http://www.sunnytek.net/admin/xiazaifiles/201011316817265.pdf.

Table 11. Menu settings for the Ametek 7270 DSP Lock-in amplifier

Parameter	Setting		Parameter	Setting
AC Gain	0 dB		Input Coupling	DC
Dynamic Reserve, DR	6		Input Shell	Ground
Input Limit	2.8 V_{pk}		Input Mode	Voltage
Time Constant 1	50 ms		Input Connector	A
Slope 1	12 dB/Oct		Ref Source	INT
Sync Time Constant	On		Harmonic 1	1st
Time Constant Mode	Normal		Harmonic 1 Phase	0.000°
Time Constant 2	50 ms		Harmonic 2	2nd
Slope 2	12 dB/Oct		Harmonic 2 Phase	0.000°
X1 Offset	0.00%		Oscillator Frequency	2500.000 Hz
Y1 Offset	0.00%		Oscillator Amplitude	1.000000 V_{rms}
Offset Status	X & Y1		DAC1 Setup	X1% (2.5 V fs)
X2 Offset	0.00%		DAC3 Setup	X2% (2.5 V fs)
Y2 Offset	0.00%			
Offset Status	X & Y2			
Input Device	Bipolar			
Line Notch Filter	60			
Auto AC Gain	Off			
DEMOD2 Source	SIGADC			

APPENDIX 4. ELECTRICAL SCHEMATIC FOR OPEN LOOP CONTROL OF MOD ARM MIRROR

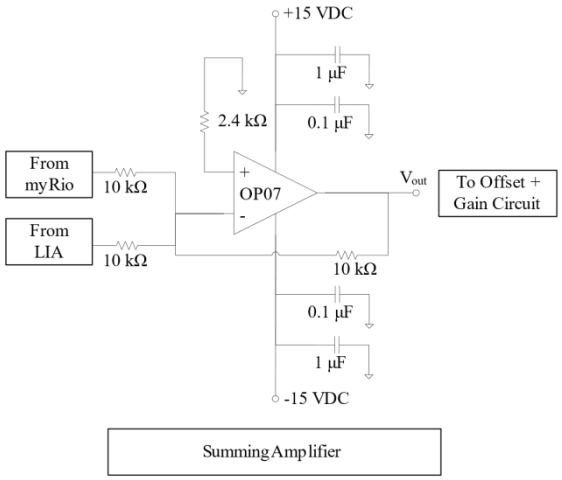

Figure 99. Electrical schematic for MOD arm summing amplifier

Figure 99 shows the electrical schematic for the MOD arm summing amplifier. This amplifier is designed to add the reference voltage from the lock-in amplifier (f = 2.5 kHz, amplitude = 1.00 V_{rms}) to an input voltage from the LabVIEW® GUI's manual offset input box (Figure 107). The output of this amplifier is then sent to an offset and gain circuit similar to those in Figure 98 that will drive the MOD arm PZT actuator. The offset of the output voltage is set such that the minimum voltage of the MOD arm PZT will drive slightly above 0 V, around 0.1 V for the minimum, and the maximum drive voltage is adjusted in the gain amplifier until a maximum displacement of the MOD arm mirror of 150 nm is achieved. The modulation depth is verified using a capacitive gage.

APPENDIX 5. ELECTRICAL SCHEMATIC FOR MOD ARM RTD CIRCUIT

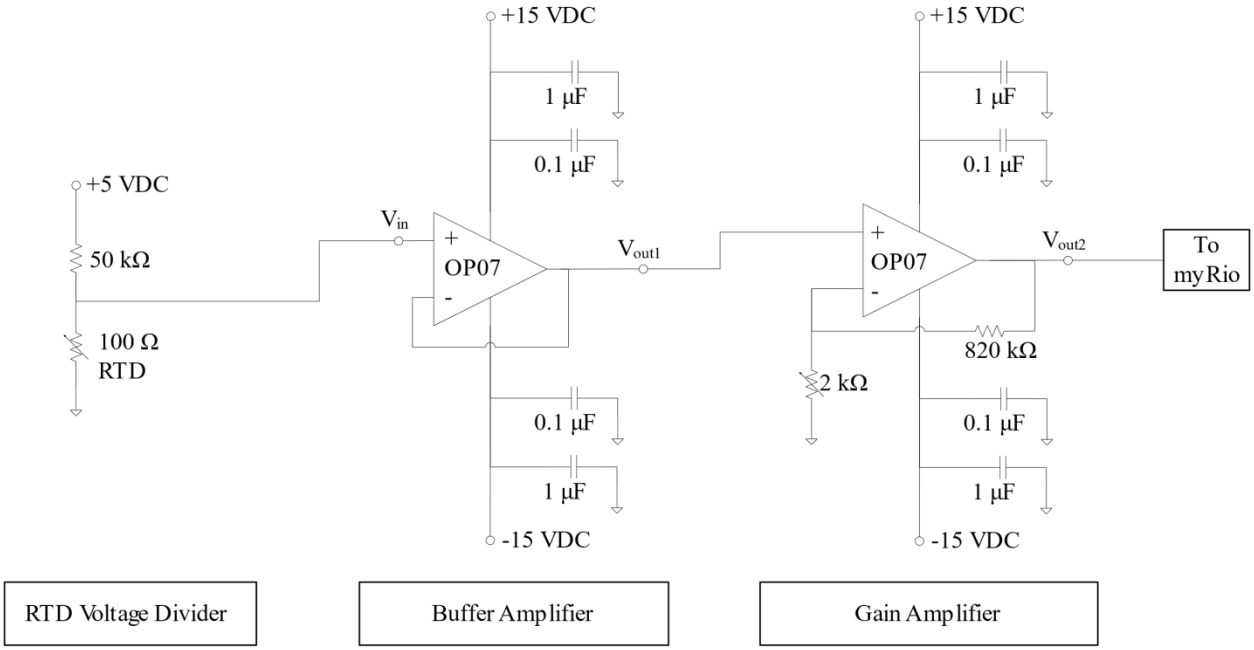

Figure 100. Electrical schematic for RTD temperature measuring circuit

Figure 100 shows the electrical schematic for the RTD temperature measuring circuit that is attached to the MOD arm PZT flexure. The RTD is configured in a voltage divider configuration with the RTD connected on the 0 V reference of the voltage divider. The 50 kΩ resistor is chosen to limit the current flowing through the RTD, thus reducing the i^2R heating of the RTD. Using the values given in the schematic, the drive current through the RTD is approximately 100 µA, and a heating input of approximately 1000 nW.

The output voltage across the RTD is then fed into a buffer amplifier to limit the current draw of the gain amplifier that is next in line. The gain amplifier is set to have an output voltage of approximately 4.5 V when the RTD is measuring 20°C. This voltage is then fed into the myRio which has an input range of 0 to 5 VDC. The myRio has a 12-bit A/D converter and a resolution of 1.22 mV.

Using the Callendar-Van Dusen equation, Equation 50, the approximate output voltage of the RTD can be calculated at 20°C – approximately 10 mV.

$$R(T) = R_0(1 + AT + BT^2)$$ *Equation 50*

where:

R(T) = resistance of the RTD as a function of temperature [Ω],

T = measured temperature [°C] and

A, B = calibration coefficients for each specific RTD [$\Omega \cdot °C^{-1}$].

The gain of the amplifier would then need to be set such that a large temperature excursion would not over-saturate the A/D converter on the myRio, although there is some allowance. The gain of the amplifier was set to be approximately 411 so the system would output approximately 4.5 VDC to the myRio at 20°C.

Due to the fact that the *A* and *B* coefficients that are provided by the manufacturer aren't exact, a two step / two temperature calibration was performed using a calibrated Fluke 1523 temperature probe. An offset was determined between the measured value of the Fluke 1523 and the measured voltage at the output of the gain amplifier. The offset value was determined to be -4.684°C.

The final temperature resolution can be calculated using the gain and the input resolution of the myRio. The approximate temperature resolution of the system is ±0.006°C plus the resolution of the calibration step. The total resolution of the system is approximately ±0.016°C (k =1).

The final output temperature equation is below:

$$T = \frac{-AR_0 + \sqrt{(AR_0)^2 - 4(BR_0)\left[R_0 - \frac{\left(\frac{V_{out2}}{G}\right)R}{V_A - \left(\frac{V_{out2}}{G}\right)}\right]}}{2BR_0} + T_{offset}$$ *Equation 51*

where:

T = final measured temperature [°C],

A, B = calibration coefficient provided by suppliers [$\Omega \cdot °C^{-1}$],

R_0 = Initial resistance at 20°C [Ω],

R = 50 kΩ resistor value [Ω],

V_{out2} = final output voltage [V],

G = gain of amplifier stage [-],

V_A = input power supply voltage [V], and

T_{offset} = calibration offset value [°C].

APPENDIX 6. SAMPLE CALIBRATION PLOT FOR HQLI DISPLACEMENT VS. CAPACITANCE GAGE MEASUREMENT

A sample calibration plot of the displacement of the HQLI versus the measured displacement of the capacitance gage is shown below in Figure 101. This sample plot shown has 123,000 data points. A linear best fit was applied to the data and the results are shown in the top right hand corner of the plot.

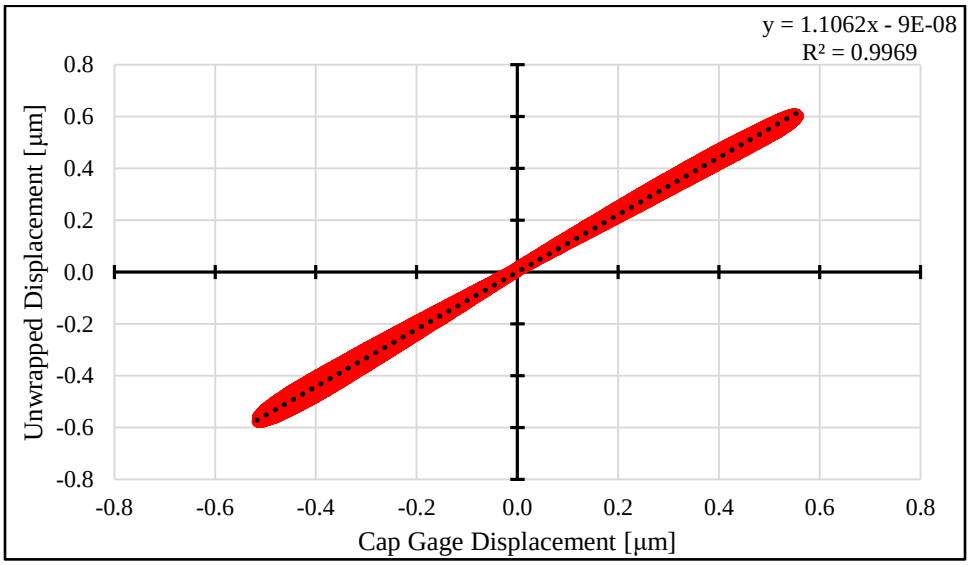

Figure 101. Sample calibration plot for the HQLI displacement vs. the capacitance gage measurement

APPENDIX 7. PNEUMATIC AND ELECTRICAL SCHEMATIC FOR DCVS

The electrical schematic for controlling the directional control valves via a DAQ device is shown below in Figure 102.

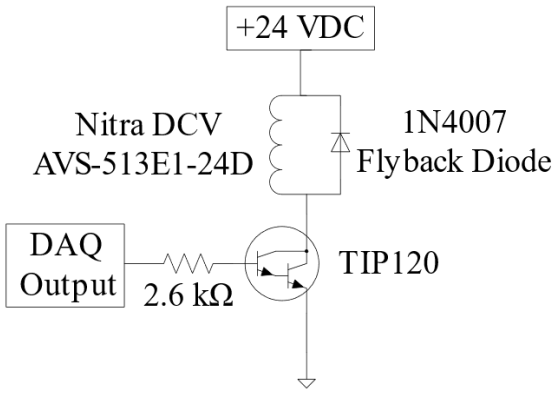

Figure 102. Electrical schematic for DCV connection to DAQ

The actual implementation of the schematic above is shown below in Figure 103. TIP120 NPN Darlington pair transistors are used to power the solenoids on the DCVs. Their base current is limited via the output of the DAQ device and a 2.6 kΩ resistor. A flyback diode is provided across the terminals of the DCVs to prevent unwanted reverse voltage spikes from going back to the TIP120s. For the actuation of the DCVs, they only require 104 mA of current to operate. This results in a power dissipation of 73 mW, which doesn't require an external heat sink.

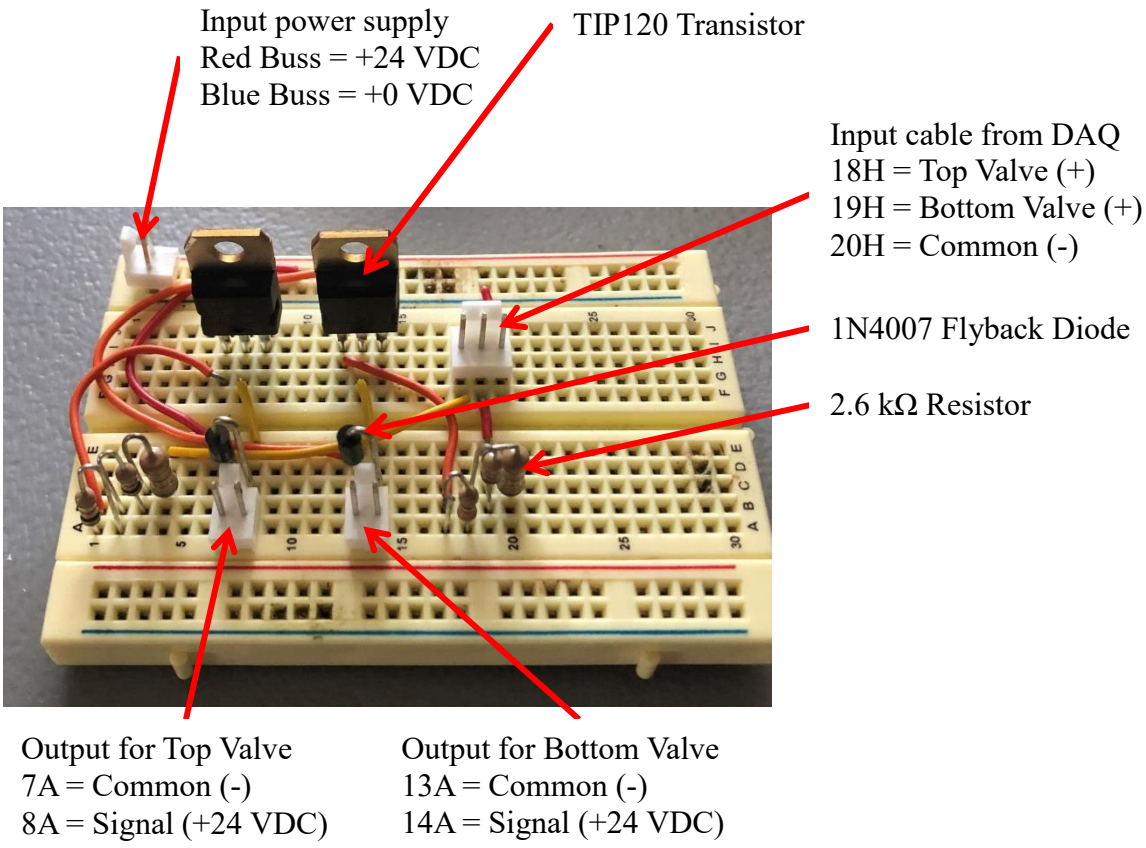

Figure 103. Actual implementation of DCV control via DAQ device

The schematic for the pneumatic cooling configuration is shown below in Figure 104. The thermal actuator is modeled as a heat exchanger in the diagram. Optimization for the parameters discussed below has not been completed as of this writing. The inlet compressed air pressure is regulated via a manual pressure regulator. The custom fittings in the thermal actuator have been tested with 100 psi of compressed air and have not experienced failures. A 5/2 solenoid controlled directional control valve is used to provide the appropriate type of cooling to the actuator, either mist cooling or compressed air only. The DAQ device will determine the type of cooling required whether the actuator is in extension mode (compressed air only) or contraction mode (mist cooling). Separate flow controllers on the mist side and the compressed air side regulate the flow for each type of cooling. On the inlet to the actuator, there are sensors to

measure the incoming compressed air pressure, compressed air temperature, and the flow rate of the compressed air. At the outlet, there are sensors to measure the outgoing compressed air pressure and temperature. These parameters will help determine the overall heat transfer and efficiency of thermal actuator.

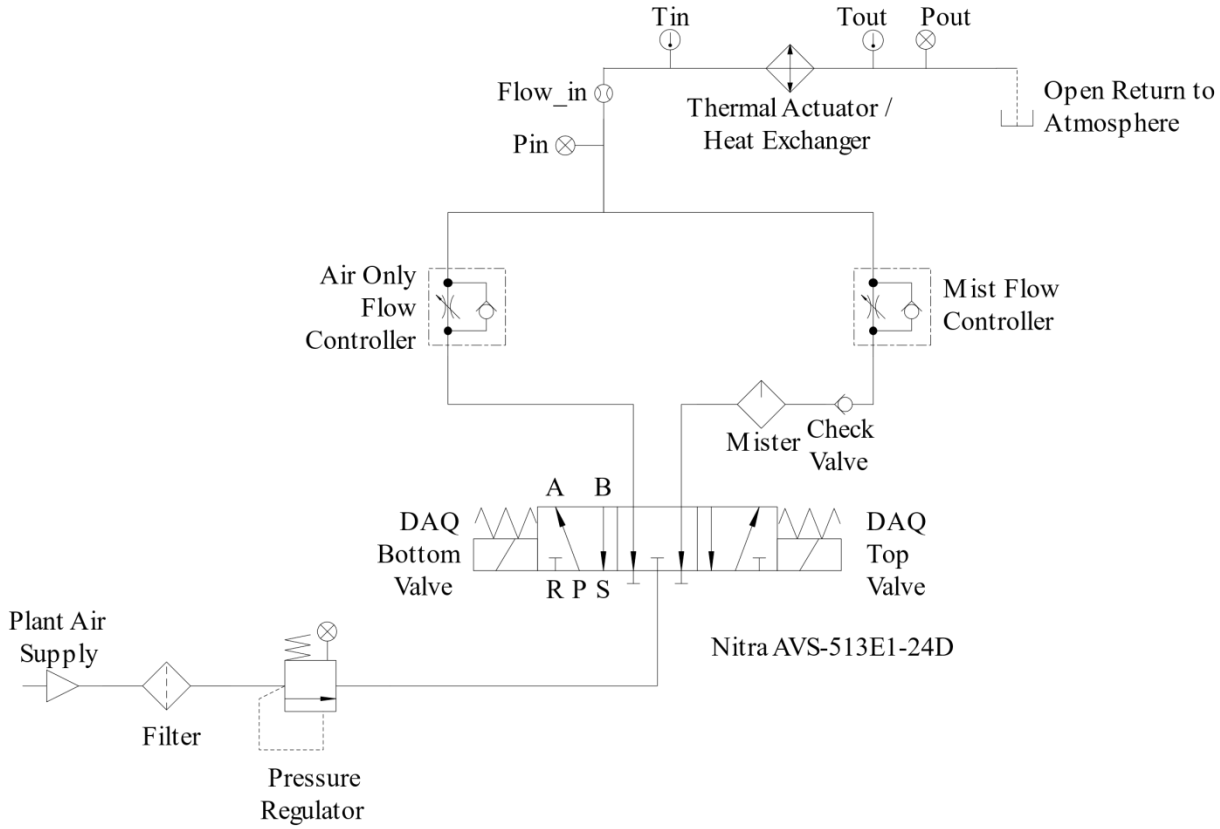

Figure 104. Schematic for pneumatic cooling of thermal actuator

APPENDIX 8. ELECTRICAL SCHEMATIC FOR RTD ON THERMAL ACTUATOR CIRCUIT BOARD

The RTD circuits that are mounted on the thermal actuator board are configured in a full bridge configuration using a three wire, 100 Ω RTD, see Figure 105 below. If these are to be utilized with a myRio, they will need to be re-configured to use a schematic similar to what is shown in Appendix 5. Electrical Schematic for MOD Arm RTD Circuit that has a gain amplifier. Depending on the ambient temperature and the temperature rise that can be expected, the gain may need to be adjusted to not saturate the input to the DAQ device.

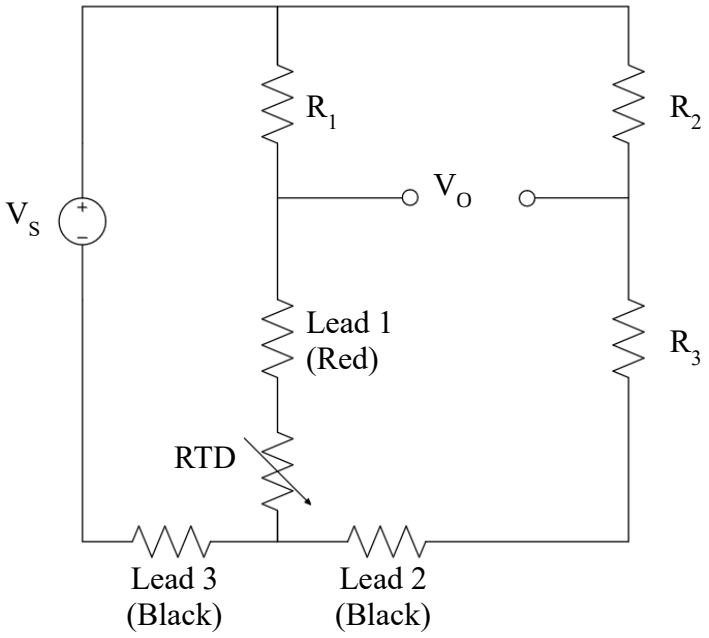

Figure 105. RTD Circuit on thermal actuator board

APPENDIX 9. ELECTRICAL SCHEMATIC FOR THE ZVS CIRCUIT

The electrical schematic for the ZVS circuit is shown below in Figure 106. When operating this circuit at high duty cycles, a cooling fan should be used to keep the heat sinks for the MOSFETs cool during operation. There is no current shunt resistor shown in this schematic. In this schematic, the IN4742A diodes are shown as standard diodes and these diodes are actually zener diodes. The IN4742A is the correct part number, the representation on the schematic is incorrect.

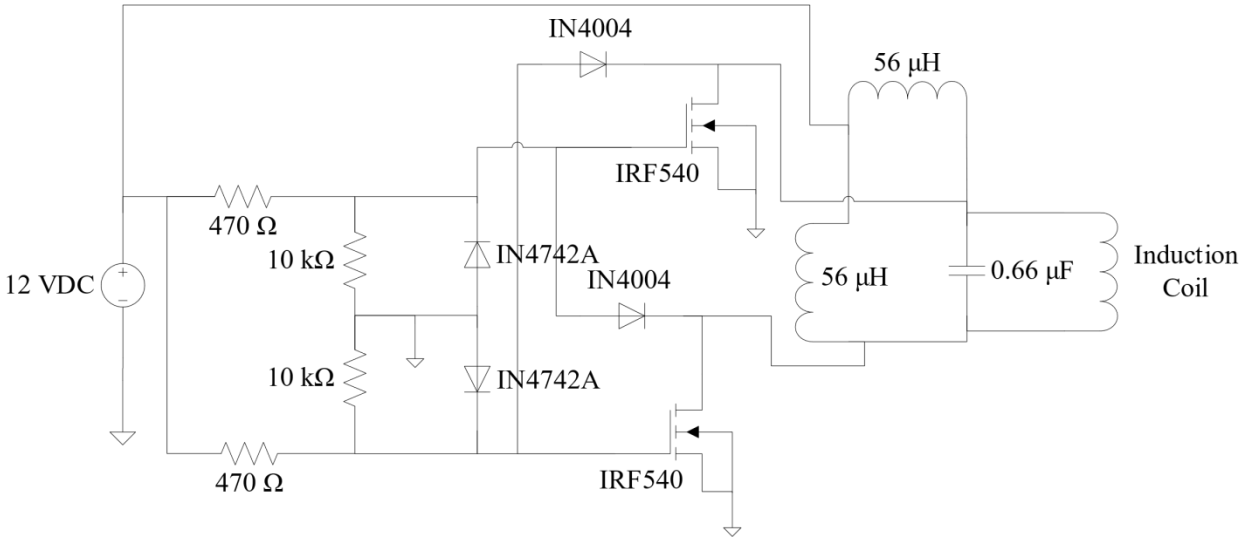

Figure 106. Electrical schematic for ZVS circuit

APPENDIX 10. CAD FILE STRUCTURE

The CAD file (3D models and drawings) structure for the thermal actuator and HQLI is shown below. Below those headings are the subsystems of each system.

10.1. HQLI FILE FOLDERS

1. Coaxial Tip Tilt
2. Coaxial Tip Tilt Translate
3. Collimating Lens Adapter
4. Differential Screw Test
5. FC Fiber Clamp
6. Free Space Design
7. Grinding Glass Reflection Rods
8. MT Hand Polisher
9. PZT Motion
10. Range Test
11. Single Crystal
12. Tip Tilt Fixture
13. VLM Adapter

10.2. THERMAL ACTUATOR FILE FOLDERS

1. Actuator Assembly Fixture
2. Actuator
3. Cooling Tubes
4. Flowmeter, Pressure, and Temperature Sensor Plates
5. Frame

6. Induction Heater Spacer
7. Leaf Flexure Machining Fixture
8. Litz Wire Coil
9. MDD10A Spacer
10. Optical Knife Edge Sensor
11. Shunt Resistor Mount

APPENDIX 11. LABVIEW® PROGRAM FOR OPEN LOOP CONTROL OF MOD ARM

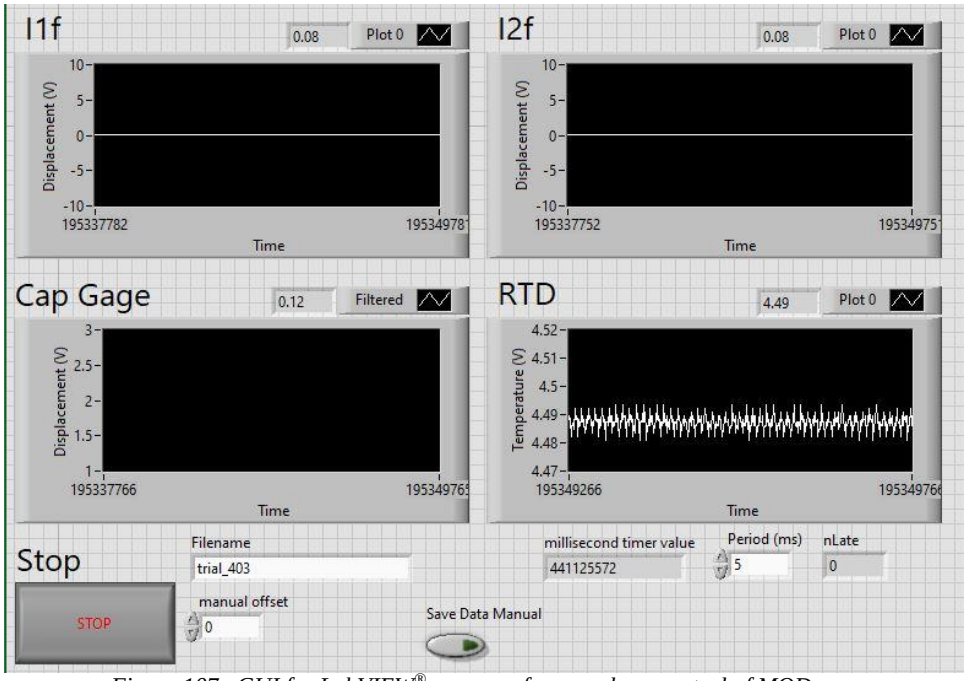

Figure 107. GUI for LabVIEW® program for open loop control of MOD arm

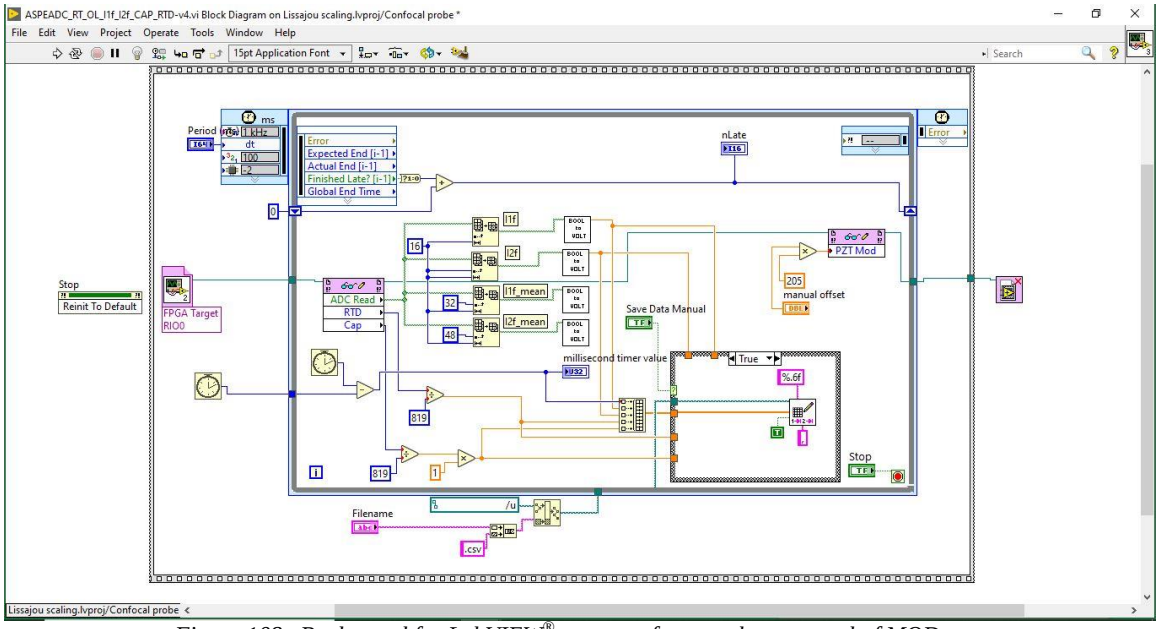

Figure 108. Back panel for LabVIEW® program for open loop control of MOD arm

APPENDIX 12. MATLAB® PROGRAM FOR EVALUATING HQLI

```
%  File for complete HQLI characterization
%
%   Script file : HQLI_v1
%-------------------------------------------------------------
%   Purpose:
%       To characterize the HQLI's parameters:
%       Signal to noise
%       lateral (dx) resolution
%       best estimate of the calibration error
%-------------------------------------------------------------
%   Record of revisions
%       Date            Programmer          Description of change
%       ====            ==========          =====================
%       06/12/2021      DJ Hastings         Initial
%
%-------------------------------------------------------------
%Setting environment

clc
clear all
close all
format compact
format long

%-------------------------------------------------------------
% load measurement data
% measurement data needs to be formatted with no headers and data in
% columns like this:
% first column = time [ms]
% second column = I1f [V]
% third column = I2f [V]
% fourth column = RTD [V]
% fifth column = CAP [V]

% files to load
%num = load('trial_100.csv'); % f = 0.00924 Hz; fit3 = 0.0074; xfit = 600
%num = load('trial_108.csv'); % f = 0.00924 Hz; fit3 = 0.0074; xfit = 600
%num = load('trial_109.csv'); % f = 0.00924 Hz; fit3 = 0.0074; xfit = 600
%num = load('trial_110.csv'); % f = 0.00924 Hz; fit3 = 0.0074; xfit = 600
%num = load('trial_111.csv'); % f = 0.00924 Hz; fit3 = 0.0074; xfit = 600
%num = load('trial_112.csv'); % f = 0.00924 Hz; fit3 = 0.0074; xfit = 600
%num = load('trial_113.csv'); % f = 0.00924 Hz; fit3 = 0.0074; xfit = 600
%num = load('trial_114.csv'); % f = 0.00924 Hz; fit3 = 0.0074; xfit = 600
%num = load('trial_115.csv'); % f = 0.00924 Hz; fit3 = 0.0074; xfit = 600
%num = load('trial_116.csv'); % f = 0.00924 Hz; fit3 = 0.0074; xfit = 600
%num = load('trial_117.csv'); % f = 0.00924 Hz; fit3 = 0.0074; xfit = 600
%num = load('trial_118.csv'); % f = 0.00924 Hz; fit3 = 0.0074; xfit = 600
%num = load('trial_119.csv'); % f = 0.00924 Hz; fit3 = 0.0074; xfit = 600
%num = load('trial_120.csv'); % f = 0.00924 Hz; fit3 = 0.0074; xfit = 600
%num = load('trial121b.csv'); % f = 0.00924 Hz; fit3 = 0.0074; xfit = 600
%num = load('trial_122.csv'); % f = 0.00924 Hz; fit3 = 0.0074; xfit = 600
%num = load('trial_123.csv'); % f = 0.00924 Hz; fit3 = 0.0074; xfit = 600
%num = load('trial_124.csv'); % f = 0.00924 Hz; fit3 = 0.0074; xfit = 600
%num = load('trial_125.csv'); % f = 0.00924 Hz; fit3 = 0.0074; xfit = 600
```

```
%num = load('trial_200.csv'); % f = 0.00924 Hz; fit3 = 0.0074; xfit = 600
%num = load('trial_201.csv'); % f = 0.00924 Hz; fit3 = 0.0074; xfit = 600
%num = load('trial_202.csv'); % f = 0.00924 Hz; fit3 = 0.0074; xfit = 600
%num = load('trial_203.csv'); % f = 0.00924 Hz; fit3 = 0.0074; xfit = 600
%num = load('trial_204.csv'); % f = 0.00924 Hz; fit3 = 0.0074; xfit = 600
%num = load('trial_205.csv'); % f = 0.00924 Hz; fit3 = 0.0074; xfit = 600
%num = load('trial_206.csv'); % f = 0.00924 Hz; fit3 = 0.0074; xfit = 600
%num = load('trial_207.csv'); % f = 0.00924 Hz; fit3 = 0.0074; xfit = 600
%num = load('trial_208.csv'); % f = 0.00924 Hz; fit3 = 0.0074; xfit = 600
%num = load('trial_300.csv'); % f = 0.00924 Hz; fit3 = 0.0074; xfit = 600
%num = load('trial_301.csv'); % f = 0.00924 Hz; fit3 = 0.0074; xfit = 600
%num = load('trial_302.csv'); % f = 0.00924 Hz; fit3 = 0.0074; xfit = 600
%num = load('trial_303.csv'); % f = 0.00924 Hz; fit3 = 0.0074; xfit = 600
%num = load('trial_304.csv'); % f = 0.00924 Hz; fit3 = 0.0074; xfit = 600
%num = load('trial_305.csv');
%num = load('trial_306.csv');
%num = load('trial_307.csv');
%num = load('trial_308.csv');
%num = load('trial_309.csv');
%num = load('trial_310.csv');
%num = load('trial_400.csv');
%num = load('trial_401.csv');
num = load('trial_402.csv');
%num = load('trial_402b.csv'); % condensed version of 402

%-------------------------------------------------------------
% input these parameters for each set of data
prompt = {'Enter estimated DUT frequency:', 'Enter estimate for fit1:',
'Enter estimate for fit3:'};
dlgtitle = 'Input';
dims = [1 35];
definput = {'0.00924', '4.689', '0.0074'};
answer1 = inputdlg(prompt,dlgtitle,dims,definput);
f_DUT = str2num(answer1{1});
fit1 = str2num(answer1{2});
fit3 = str2num(answer1{3});

% values we don't ask the operator for
xfit = 1/f_DUT * 6; % x-scale size
offset = 0.2; % this is the amount of data to exclude at the top and
              % bottom of the curves (eliminates the sudden positional
              % changes in the triangle waves)


% ask to save data
prompt2 = {'Save data: 1 = yes, 0 = no'};
dlgtitle2 = 'Input';
dims = [1 35];
definput2 = {'0'};
answer2 = inputdlg(prompt2,dlgtitle2,dims,definput2);
savedata = str2num(answer2{1});

% ask if time is in seconds or ms
prompt3 = {'Time is seconds or ms: 1 = s, 0 = ms'};
dlgtitle3 = 'Input';
dims = [1 35];
definput3 = {'0'};
```

```
answer3 = inputdlg(prompt3,dlgtitle3,dims,definput3);
timedt = str2num(answer3{1});

% ask if need to flip cap data
prompt4 = {'Flip cap gage data: 1 = yes, 0 = no'};
dlgtitle4 = 'Input';
dims = [1 35];
definput4 = {'0'};
answer4 = inputdlg(prompt4,dlgtitle4,dims,definput4);
capflip = str2num(answer4{1});


% if yes to savedata, then this is the filename
if( savedata == 1)

prompt3 = {'Enter filename'};
dlgtitle3 = 'Input';
dims = [1 30];
definput3 = {'trial127b.csv'};
answer3 = inputdlg(prompt3,dlgtitle3,dims,definput3);
filename = answer3{1};

else

end

%-------------------------------------------------------------
% initialize all data

xdata = num(:,1);   %time
ydata1 = num(:,2);   %I1f
ydata2 = num(:,3);   %I2f
rtd = num(:,4);  %temperature in V
cap = num(:,5); %cap gage displacement in V

% if yes to flip cap gage data
if( capflip == 1)
cap = -cap;

else
cap = cap;

end


if (timedt == 0)
%-----------------------------------
% shift time to 0 and convert to ms (if needed)
xdata = xdata/1000;
xdata = (xdata-min(xdata));

else
%-----------------------------------
% shift time to 0 and convert to ms (if needed)
xdata = xdata-min(xdata);
```

```
end


%-------------------------------------------------------------
% find and remove duplicate I1f measurements
i = 1;
total = length(xdata);

for i = 1:total-2

   if(ydata1(i) == ydata1(i+1))
    xdata(i) = NaN;
    ydata1(i) = NaN;
    ydata2(i) = NaN;
    rtd(i) = NaN;
    cap(i) = NaN;
   else
    ydata1 = ydata1;
   end
end

% remove NaN from time, I1f, I2f, RTD, and cap
time = rmmissing(xdata);
ydata1 = rmmissing(ydata1);
ydata2 = rmmissing(ydata2);
rtd = rmmissing(rtd);
cap = rmmissing(cap);




%-----------------------------------
% shift cap gage to 0 and convert from V to um
cap_sens = 1.76; % cap gage sensitivity in um / V
cap = cap*cap_sens; % convert from V to um
capoff = cap - min(cap);

%-----------------------------------
% find total number of cycles

T_DUT = 1/f_DUT; % period of DUT arm in s

l = length(time);  % how many total data points, was xdata

total = max(time/T_DUT);  % how many cycles, was xdata

xmax = max(time); % max time, was xdata

%-----------------------------------
% find each cycle's data

if total > 1  % need to determine more than one visibility term

n = 1; %reset for loop

for n = 1:total-1
%create new x, y1, and y2 array for each n
```

```
x_min = T_DUT*n - T_DUT;
x_max = T_DUT*n;

% create an index of 0 or 1 for xdata's between x_min and x_max
x_index = find(time <= x_max & time >= x_min);

x_new = time(x_index); %was xdata
y1_new = ydata1(x_index);
y2_new = ydata2(x_index);
t_new = rtd(x_index);
cap_new = capoff(x_index);

% Temperature conversion
% mean temperature during one cycle
R0 = 100;
A = 3.9083E-3;
B = -5.775E-7;
R1 = 50888;
V_A = 4.953;
G = 419.935;
T_offset = -4.684;
RTD = ((t_new/G)*R1) ./ (V_A-(t_new/G));
T = (-A*R0+sqrt((A*R0)^2-(4*B*R0*(R0-RTD))))/(2*B*R0) + T_offset;
T_mean(n) = mean(T);

% %-----------------------------------
% % plot I1f vs. time
% figure(1)
% plot(x_new, y1_new, 'ob');
% xlabel 'Time [s]'
% ylabel 'I1f [V]'
% title(['I1f vs. Time'])
% %xlim([0 max(ydata1)])
% grid on
% hold on

%-----------------------------------
% fit Fourier series to I1f

[xData1, yData1] = prepareCurveData( cap_new, y1_new );

% Set up fittype and options
ft1 = fittype( 'fourier8' );
opts1 = fitoptions( 'Method', 'NonlinearLeastSquares' );
opts1.Display = 'Off';
opts1.StartPoint = [0 0 0 0 0 0 0 0 0 0 0 0 0 0 0 0 0 fit1];

% Fit model to data
[fitresult1, gof] = fit( xData1, yData1, ft1, opts1 );

% % Plot fit with data
% figure(2);
% h = plot( fitresult1, xData1, yData1 );
% legend( h, 'I1f vs. Cap Gage Displacement', 'cap I1f', 'Location',
'NorthEast', 'Interpreter', 'none' );
% xlabel 'Displacement [um]';
% ylabel 'I1f [V]';
```

```
% grid on
% hold on

% generate fit curve
%  y =  a0 + a1*cos(x*w) + b1*sin(x*w) +
%               a2*cos(2*x*w) + b2*sin(2*x*w) + a3*cos(3*x*w) + b3*sin(3*x*w)
+
%               a4*cos(4*x*w) + b4*sin(4*x*w) + a5*cos(5*x*w) + b5*sin(5*x*w)
+
%               a6*cos(6*x*w) + b6*sin(6*x*w) + a7*cos(7*x*w) + b7*sin(7*x*w)
+
%               a8*cos(8*x*w) + b8*sin(8*x*w)

a0_1 = fitresult1.a0;
a1_1 = fitresult1.a1;
b1_1 = fitresult1.b1;
a2_1 = fitresult1.a2;
b2_1 = fitresult1.b2;
a3_1 = fitresult1.a3;
b3_1 = fitresult1.b3;
a4_1 = fitresult1.a4;
b4_1 = fitresult1.b4;
a5_1 = fitresult1.a5;
b5_1 = fitresult1.b5;
a6_1 = fitresult1.a6;
b6_1 = fitresult1.b6;
a7_1 = fitresult1.a7;
b7_1 = fitresult1.b7;
a8_1 = fitresult1.a8;
b8_1 = fitresult1.b8;
w_1 = fitresult1.w;

% Plot I1f using fit coefficients
I1f_fit = a0_1 + a1_1*cos(cap_new*w_1) + b1_1*sin(cap_new*w_1) +
a2_1*cos(2*cap_new*w_1) + b2_1*sin(2*cap_new*w_1) + a3_1*cos(3*cap_new*w_1) +
b3_1*sin(3*cap_new*w_1) + a4_1*cos(4*cap_new*w_1) + b4_1*sin(4*cap_new*w_1) +
a5_1*cos(5*cap_new*w_1) + b5_1*sin(5*cap_new*w_1) + a6_1*cos(6*cap_new*w_1) +
b6_1*sin(6*cap_new*w_1) + a7_1*cos(7*cap_new*w_1) + b7_1*sin(7*cap_new*w_1) +
a8_1*cos(8*cap_new*w_1) + b8_1*sin(8*cap_new*w_1);
% a0 + a1*cos(capoff*w) + b1*sin(capoff*w) + ...;

% % Plot I1f_fit with original data
% figure(2);
% plot( x_new, I1f_fit, x_new, y1_new );
% title('I1f vs. Time');
% xlabel 'Time [s]';
% ylabel 'I1f [V]';
% legend('I1f Fit', 'I1f Meas', 'Location', 'NorthEast');
% grid on
% hold on

% Error of fit
I1f_diff = y1_new - I1f_fit;

% Remove outliers from fit

j = 1;
```

```
total2 = length(I1f_diff);

for j = 1:total2

I1f_rms = std(I1f_fit);

if(abs(I1f_diff)> 3*I1f_rms)
    NaN;
else
    I1f_diff = I1f_diff;
end

end

I1f_rms_OR(n) = std(I1f_diff); % I1f noise with outliers removed

% % plot I1f error vs. time
% figure(3)
% plot(x_new, I1f_diff, 'b');
% xlabel 'Time [s]'
% ylabel 'I1f error [V]'
% title(['I1f error vs. Time'])
% xlim([0 max(x_new)])
% grid on
% hold on

% %-------------------------------------
% % plot I2f vs. time
% figure(4)
% plot(time, ydata2, 'or');
% xlabel 'Time [s]'
% ylabel 'I2f [V]'
% title(['I2f vs. Time'])
% %xlim([0 max(ydata2)])
% grid on
% hold on

%-------------------------------------
% fit Fourier series to I2f

[xData2, yData2] = prepareCurveData( cap_new, y2_new );

% Set up fittype and options
ft2 = fittype( 'fourier8' );
opts2 = fitoptions( 'Method', 'NonlinearLeastSquares' );
opts2.Display = 'Off';
opts2.StartPoint = [0 0 0 0 0 0 0 0 0 0 0 0 0 0 0 0 0 fit1];

% Fit model to data
[fitresult2, gof] = fit( xData2, yData2, ft2, opts2 );

% % Plot fit with data
% figure(5)
% j = plot( fitresult2, xData2, yData2 );
% legend( j, 'I2f vs. cap gage displacement', 'cap I2f', 'Location',
'NorthEast', 'Interpreter', 'none' );
% xlabel 'Cap Gage Displacement [um]';
```

```
% ylabel 'I2f [V]';
% grid on
% hold on

a0_2 = fitresult2.a0;
a1_2 = fitresult2.a1;
b1_2 = fitresult2.b1;
a2_2 = fitresult2.a2;
b2_2 = fitresult2.b2;
a3_2 = fitresult2.a3;
b3_2 = fitresult2.b3;
a4_2 = fitresult2.a4;
b4_2 = fitresult2.b4;
a5_2 = fitresult2.a5;
b5_2 = fitresult2.b5;
a6_2 = fitresult2.a6;
b6_2 = fitresult2.b6;
a7_2 = fitresult2.a7;
b7_2 = fitresult2.b7;
a8_2 = fitresult2.a8;
b8_2 = fitresult2.b8;
w_2 = fitresult2.w;

% Plot I2f using fit coefficients
I2f_fit = a0_2 + a1_2*cos(cap_new*w_2) + b1_2*sin(cap_new*w_2) +
a2_2*cos(2*cap_new*w_2) + b2_2*sin(2*cap_new*w_2) + a3_2*cos(3*cap_new*w_2) +
b3_2*sin(3*cap_new*w_2) + a4_2*cos(4*cap_new*w_2) + b4_2*sin(4*cap_new*w_2) +
a5_2*cos(5*cap_new*w_2) + b5_2*sin(5*cap_new*w_2) + a6_2*cos(6*cap_new*w_2) +
b6_2*sin(6*cap_new*w_2) + a7_2*cos(7*cap_new*w_2) + b7_2*sin(7*cap_new*w_2) +
a8_2*cos(8*cap_new*w_2) + b8_2*sin(8*cap_new*w_2);
% a0 + a1*cos(capoff*w) + b1*sin(capoff*w) + ...;

% % Plot I2f_fit with original data
% figure(5);
% plot( x_new, I2f_fit, x_new, y2_new );
% title('I2f vs. Time');
% xlabel 'Time [s]';
% ylabel 'I2f [V]';
% legend('I2f Fit', 'I2f Meas', 'Location', 'NorthEast');
% grid on
% hold on

% Error of fit
I2f_diff = y2_new - I2f_fit;

% Remove outliers from fit

k = 1;
total3 = length(I2f_diff);

for k = 1:total3

I2f_rms = std(I2f_fit);

if(abs(I2f_diff)> 3*I2f_rms)
    NaN;
else
```

```
    I2f_diff = I2f_diff;
end

end

I2f_rms_OR(n) = std(I2f_diff);  % I2f noise with outliers removed

% % plot I2f error vs. time
% figure(6)
% plot(x_new, I2f_diff, 'b');
% xlabel 'Time [s]'
% ylabel 'I2f error [V]'
% title(['I2f error vs. Time'])
% xlim([0 max(xdata)])
% grid on
% hold on


% % plot I2f vs. I1f, fitted curves
% figure(7)
% plot(I1f_fit, I2f_fit, 'b');
% xlabel 'I1f [V]'
% ylabel 'I2f [V]'
% title(['I2f vs. I1f, fit'])
% grid on
% hold on

%************************************************************
%************************************************************

%-----------------------------------
% start unwrapping phase using the fitted I1f and I2f, calculate the S-N
% and contrast

%-----------------------------------
% wavelength of laser
lambda=636.7e-9; % WL in nm

%-----------------------------------
% Remove the Lissajou offset
% use I1f_fit, I2f_fit
I1f_offsetrem=(I1f_fit-mean(I1f_fit));
I2f_offsetrem=(I2f_fit-mean(I2f_fit));

%-----------------------------------
% Normalize the Lissajous
% use I1f_fit, I2f_fit
I1f=((I1f_fit-mean(I1f_fit))/(max(I1f_offsetrem)-min(I1f_offsetrem)));
I2f=((I2f_fit-mean(I2f_fit))/(max(I2f_offsetrem)-min(I2f_offsetrem)));

if(total < 25) % don't plot 3d plot if there is a lot of data

% Plot I1f vs. I2f, fitted curves, normalized
figure(8)
plot3(I1f, I2f, x_new, '.');
xlabel 'I1f [V]'
ylabel 'I2f [V]'
```

```
zlabel 'Time [s]'
title(['I2f-norm vs. I1f-norm vs. Time'])
grid on
hold on

else

end



%-----------------------------------
% Calculate signal to noise for I1f

I1f_mean(n) = mean(abs(I1f));
I2f_mean(n) = mean(abs(I2f));

SN_1(n) = I1f_mean / I1f_rms_OR;  % S-N for I1f
SN_2(n) = I2f_mean / I2f_rms_OR;  % S-N for I2f

FC_1(n) = 1- 1 / SN_1(n);  % contrast for I1f
FC_2(n) = 1- 1 / SN_2(n);  % contrast for I2f

x_plot(n) = x_new(1);


end

elseif total == 1

x_plot = x_new;

I1f_mean = mean(abs(I1f));
I2f_mean = mean(abs(I2f));

SN_1 = I1f_mean / I1f_rms_OR;  % S-N for I1f
SN_2 = I2f_mean / I2f_rms_OR;  % S-N for I2f

FC_1 = 1- 1 / SN_1;  % contrast for I1f
FC_2 = 1- 1 / SN_2;  % contrast for I2f

end
% End of loop

% % Using values obtained during for loop:
% % Plot S-N vs. time
% figure(9)
% plot(x_plot, SN_1, 'ob', x_plot, SN_2, 'or');
% xlabel 'Time [s]'
% ylabel 'Signal to Noise [-]'
% title(['Signal to Noise vs. Time'])
% xlim([0 max(time)])
% legend('SN1', 'SN2')
% grid on
% hold on

% Plot FC vs. time
```

```
figure(10)
plot(x_plot, FC_1, 'ob', x_plot, FC_2, 'or');
xlabel 'Time [s]'
ylabel 'Contrast [-]'
title(['Contrast vs. Time'])
%xlim([0 max(x_plot)]) % was xdata
ylim([0 1])
legend('FC1', 'FC2', 'location', 'southeast')
grid on
hold on

%-----------------------------------
% Using all measured values, not just the for loop values

% Recalculate the offset and normalize I1f and I2f
I1f_off=(ydata1-mean(ydata1));
I2f_off=(ydata2-mean(ydata2));
I1f_all=((ydata1-mean(ydata1))/(max(I1f_off)-min(I1f_off)));
I2f_all=((ydata2-mean(ydata2))/(max(I2f_off)-min(I2f_off)));

% % Plot I1f vs. I2f, original curves, normalized
% figure(11)
% plot(I1f_all, I2f_all, '.b');
% xlabel 'I1f [V]'
% ylabel 'I2f [V]'
% title(['I2f-meas vs. I1f-meas'])
% axis equal
% grid on
% hold on

% Calculate wrapped displacement
X=(lambda/2)*atan2(I2f_all,I1f_all)/(2*pi);

% % Plot wrapped displacement vs. time
% figure(12)
% plot(time, X, 'k'); % was xdata
% xlabel 'Time [s]'
% ylabel 'Displacement [m]'
% title(['Wrapped Displacement vs. Time'])
% xlim([0 max(time)])
% grid on
% hold on

%-----------------------------------
% Unwrapping the displacement
add=0;
for ii=1:length(X)-1

    diff(ii)=X(ii+1)-X(ii);

    if abs(diff(ii))>100e-9
        add=add-diff(ii);
    end
    add;
    unw_X(ii+1)=(X(ii+1)+add)*1E9;
end
```

```
% % Plot unwrapped displacement vs. time
% figure(13)
% plot(time, unw_X, 'k'); % was xdata
% xlabel 'Time [s]'
% ylabel 'Displacement [nm]'
% title(['Unwrapped Displacement vs. Time'])
% xlim([0 max(time)])
% grid on
% hold on

%-----------------------------------
% Fit Fourier Series to unwrapped displacement

unw_X = unw_X.'; % transpose unwrapped displacement

[xData3, yData3] = prepareCurveData( time, unw_X );

% Set up fittype and options
ft3 = fittype( 'fourier8' );
opts3 = fitoptions( 'Method', 'NonlinearLeastSquares' );
opts3.Display = 'Off';
opts3.StartPoint = [0 0 0 0 0 0 0 0 0 0 0 0 0 0 0 0 0 fit3];

% Fit model to data
[fitresult3, gof3] = fit( xData3, yData3, ft3, opts3 );

% % Plot fit with data
% figure(14)
% k = plot( fitresult3, xData3, yData3 );
% legend( k, 'unw X vs. xdata', 'unwX Fourier', 'Location', 'NorthEast',
'Interpreter', 'none' );
% xlabel 'Time [s]'
% ylabel 'Unwrapped Displacement [nm]'
% xlim([0 max(time)])
% hold on
% grid on

a0_3 = fitresult3.a0;
a1_3 = fitresult3.a1;
b1_3 = fitresult3.b1;
a2_3 = fitresult3.a2;
b2_3 = fitresult3.b2;
a3_3 = fitresult3.a3;
b3_3 = fitresult3.b3;
a4_3 = fitresult3.a4;
b4_3 = fitresult3.b4;
a5_3 = fitresult3.a5;
b5_3 = fitresult3.b5;
a6_3 = fitresult3.a6;
b6_3 = fitresult3.b6;
a7_3 = fitresult3.a7;
b7_3 = fitresult3.b7;
a8_3 = fitresult3.a8;
b8_3 = fitresult3.b8;
w_3 = fitresult3.w;

% Plot unwrapped displacement using fit coefficients
```

```
unwX_fit = a0_3 + a1_3*cos(time*w_3) + b1_3*sin(time*w_3) +
a2_3*cos(2*time*w_3) + b2_3*sin(2*time*w_3) + a3_3*cos(3*time*w_3) +
b3_3*sin(3*time*w_3) + a4_3*cos(4*time*w_3) + b4_3*sin(4*time*w_3) +
a5_3*cos(5*time*w_3) + b5_3*sin(5*time*w_3) + a6_3*cos(6*time*w_3) +
b6_3*sin(6*time*w_3) + a7_3*cos(7*time*w_3) + b7_3*sin(7*time*w_3) +
a8_3*cos(8*time*w_3) + b8_3*sin(8*time*w_3);
% a0 + a1*cos(capoff*w) + b1*sin(capoff*w) + ...;


% Error of displacement fit
unwX_fit_diff = unw_X - unwX_fit;

% Remove outliers from displacement fit
unwX_rms = std(unwX_fit_diff);

l = 1;
for l = 1:length(time);

if(abs(unwX_fit_diff)> 3*unwX_rms)
    NaN;
else
    unwX_fit_diff = unwX_fit_diff;
end

end

unwX_rms_OR = std(unwX_fit_diff);  % unwrapped displacement noise with
outliers removed


% % plot unwrapped displacement error vs. time
% figure(15)
% plot(time, unwX_fit_diff, 'b'); % was xdata
% xlabel 'Time [s]'
% ylabel 'Unwrapped Disp. error [nm]'
% title(['Unwrapped Displacement Error vs. Time'])
% xlim([0 xfit])
% grid on
% hold on

%-----------------------------------
% convert cap gage data from um to nm and compare to HQLI

capnm = cap*1000; % convert from um to nm
capavg = mean(capnm); % calculate avg cap offset
capnm = -(capnm - capavg); % shift cap gage displacement to 0.  Negative
% sign is due to the phase difference between the placement of the cap
% gage and the fiber (they are 180 deg out of phase with each other)

unwX_fit_avg = mean(unwX_fit); % calculate avg HQLI offset
unwX_fit = unwX_fit - unwX_fit_avg; % shift unwrapped displacement to 0

% Error between cap gage and HQLI
diff2 = unwX_fit - capnm;

% Remove outliers from fit
diff2_rms = std(diff2);
```

```
m = 1;
for m = 1: length(time);

if(abs(diff2)> 3*diff2_rms)
    NaN;
else
    diff2 = diff2;
end

end

diff2_rms_OR = std(diff2);  % outliers removed from cap gage data

%----------------------------------
% plot temperature vs. time
figure()
plot(x_plot, T_mean, 'ob');
xlabel 'Time [s]'
ylabel 'Temp [°C]'
title(['Temp vs. Time'])
xlim([0 max(x_plot)])
ylim([21 21.5])
grid on
hold on

% % Plot unwrapped displacement fit vs. time with cap gage
% figure(16)
% plot(time, unwX_fit, 'k', time, capnm, 'b', time, diff2, 'r'); % was
% xdata
% xlabel 'Time [s]'
% ylabel 'Displacement [nm]'
% title(['Unwrapped Displacement vs. Time'])
% xlim ([0 xfit])
% legend('HQLI', 'Cap', 'Diff')
% grid on
% hold on

% % Plot error in unwrapped displacement vs. cap gage
% figure(17)
% plot(time, diff2, 'k'); % was xdata
% xlabel 'Time [s]'
% ylabel 'Error [nm]'
% title(['Error vs. Time'])
% xlim([0 xfit])
% grid on
% hold on

% Calculate minimum S-N
SN_min1 = min(SN_1);
SN_min2 = min(SN_2);
SN_min = min(SN_min1, SN_min2)

% Calculate minimum fringe contrast
FC_min1 = min(FC_1);
FC_min2 = min(FC_2);
FC_min = min(FC_min1, FC_min2)
```

```
% Calculate resolution
dx = lambda/(2*pi*SN_min)*1000000000 % in nm

% % Plot unwrapped displacement vs. time with cap gage
% figure(18)
% plot(time, unw_X, 'k', time, capnm, 'b'); % was xdata
% xlabel 'Time [s]'
% ylabel 'Displacement [nm]'
% title(['Unwrapped Displacement vs. Time'])
% xlim ([0 xfit])
% legend('HQLI', 'Cap')
% grid on
% hold on

%*********************************************************
%*********************************************************


cap1 = -cap; %convert cap gage to 180 deg offset
hqli1 = unwX_fit / 1000; %convert hqli1 from nm to um

% %-----------------------------------
% % plot raw cap gage displacement vs time
% figure(19)
% plot(time, cap1, '.b');
% xlabel 'Time [s]'
% ylabel 'Cap Gage Displacement [um]'
% title(['Raw Cap Gage vs. Time'])
% xlim([0 max(time)])
% grid on
% hold on

% %-----------------------------------
% % plot raw hqli displacement vs time
% figure(20)
% plot(time, hqli1, '.r');
% xlabel 'Time [s]'
% ylabel 'HQLI Displacement [um]'
% title(['Raw HQLI vs. Time'])
% xlim([0 max(time)])
% grid on
% hold on

%-----------------------------------
% shift cap gage and hqli to center around 0
cap2 = cap1 - mean(cap1);
hqli2 = hqli1 - mean(hqli1);

% %-----------------------------------
% % plot shifted gage displacement vs time
% figure(21)
% plot(time, cap2, '.b');
% xlabel 'Time [s]'
% ylabel 'Cap Gage Displacement [um]'
% title(['Shifted Cap Gage vs. Time'])
% xlim([0 max(time)])
```

```
% grid on
% hold on

% %-----------------------------------
% % plot shifted hqli displacement vs time
% figure(22)
% plot(time, hqli2, '.r');
% xlabel 'Time [s]'
% ylabel 'HQLI Displacement [um]'
% title(['Shifted HQLI vs. Time'])
% xlim([0 max(time)])
% grid on
% hold on

% %-----------------------------------
% % plot shifted hqli displacement vs shifted cap gage displacement
% figure(23)
% plot(cap2, hqli2, 'b');
% xlabel 'Cap Gage Displacement [um]'
% ylabel 'HQLI Displacement [um]'
% title(['HQLI vs. Cap Gage'])
% %xlim([0 max(time)])
% grid on
% hold on

%-----------------------------------
% calculate difference betwenn cap gage and hqli
diff1 = (hqli2 - cap2)*1000; % HQLI error in nm

% Remove outliers from fit
diff1_rms = std(diff1);

j = 1;
total2 = length(diff1);
time2 = time;

for j = 1:total2

if(abs(diff1(j)) > 3*diff1_rms)
    diff1(j) = NaN;
    time2(j) = NaN;
else
   diff1(j) = diff1(j);
   time2(j) = time(j);
end

end

% remove NaN from time2 and diff1
time2 = rmmissing(time2);
diff1 = rmmissing(diff1);

diff1_rms_OR = std(diff1)  % fit noise with outliers removed

% %-----------------------------------
% % plot error vs time, complete signal
% % this is the beginning step for calculating the current system accuracy
```

```
% figure(24)
% plot(cap2, diff1, 'k'); %was time2
% xlabel 'Cap Gage Displacement [um]'
% ylabel 'HQLI Diff [nm]'
% title(['HQLI Diff vs. Cap Gage Displacement'])
% %xlim([0 max(time)])
% grid on
% hold on

% linear fit to rotate diff plot
[xData6, yData6] = prepareCurveData( cap2, diff1 );

% Set up fittype and options
ft6 = fittype( {'x', '1'}, 'independent', 'x', 'dependent', 'y',
'coefficients', {'a', 'b'} );

% Fit model to data
[fitresult6, gof] = fit( xData6, yData6, ft6 );

% % Plot fit with data
% figure(900);
% z = plot( fitresult6, xData6, yData6 );
% legend( z, 'diff1 vs. cap2', 'linear fit 1', 'Location', 'NorthEast',
'Interpreter', 'none' );
% xlabel ( 'cap2 [um]' );
% ylabel( 'diff1 [nm]' );
% grid on
% hold on

a_6 = fitresult6.a;
b_6 = fitresult6.b;

acc_fit = a_6*cap2 + b_6; %fit

sys_acc = diff1 - acc_fit;

%-----------------------------------
% plot system accuracy vs displacement
figure(1000)
plot(cap2, sys_acc, 'k');
xlabel 'Cap Gage Displacement [um]'
ylabel 'System Accuracy [nm]'
title(['System Accuracy vs. Cap Gage Displacement'])
xlim([-1 1])
grid on
hold on

%sys_acc = 3 * std(sys_acc) % system accuracy

sys_acc = max(sys_acc) - min(sys_acc) % system accuracy

%-----------------------------------
% Fit Fourier Series to hqli3 data

t_plot = 4*1/f_DUT;

[xData3, yData3] = prepareCurveData( time, hqli2 );
```

```
% Set up fittype and options
ft3 = fittype( 'fourier8' );
opts3 = fitoptions( 'Method', 'NonlinearLeastSquares' );
opts3.Display = 'Off';
opts3.StartPoint = [0 0 0 0 0 0 0 0 0 0 0 0 0 0 0 0 0 fit3];

% Fit model to data
[fitresult3, gof3] = fit( xData3, yData3, ft3, opts3 );

rsquare_3 = gof3.rsquare

% % Plot fit with data
% figure(25)
% k = plot( fitresult3, 'k', xData3, yData3, 'r' );
% legend( k, 'hqli2 vs. time', 'Fourier fit', 'Location', 'NorthEast');
% xlabel 'Time [s]'
% ylabel 'HQLI [um]'
% xlim([0 max(time)])
% hold on
% grid on

a0_3 = fitresult3.a0;
a1_3 = fitresult3.a1;
b1_3 = fitresult3.b1;
a2_3 = fitresult3.a2;
b2_3 = fitresult3.b2;
a3_3 = fitresult3.a3;
b3_3 = fitresult3.b3;
a4_3 = fitresult3.a4;
b4_3 = fitresult3.b4;
a5_3 = fitresult3.a5;
b5_3 = fitresult3.b5;
a6_3 = fitresult3.a6;
b6_3 = fitresult3.b6;
a7_3 = fitresult3.a7;
b7_3 = fitresult3.b7;
a8_3 = fitresult3.a8;
b8_3 = fitresult3.b8;
w_3 = fitresult3.w;

% Plot hqli3_fit displacement using fit coefficients
hqli2_fit = a0_3 + a1_3*cos(time*w_3) + b1_3*sin(time*w_3) +
a2_3*cos(2*time*w_3) + b2_3*sin(2*time*w_3) + a3_3*cos(3*time*w_3) +
b3_3*sin(3*time*w_3) + a4_3*cos(4*time*w_3) + b4_3*sin(4*time*w_3) +
a5_3*cos(5*time*w_3) + b5_3*sin(5*time*w_3) + a6_3*cos(6*time*w_3) +
b6_3*sin(6*time*w_3) + a7_3*cos(7*time*w_3) + b7_3*sin(7*time*w_3) +
a8_3*cos(8*time*w_3) + b8_3*sin(8*time*w_3);
% a0 + a1*cos(capoff*w) + b1*sin(capoff*w) + ...;

%-----------------------------------
% find cap gage 2 min and max

cap2_min = min(cap2);
cap2_max = max(cap2);

cap2_min_offset = cap2_min - offset*cap2_min;
```

```
cap2_max_offset = cap2_max - offset*cap2_max;

% search for values between min and max
cap2_index = find(cap2 <= cap2_max_offset & cap2 >= cap2_min_offset);

time3 = time(cap2_index);
cap3 = cap2(cap2_index)*1000;
hqli3 = hqli2_fit(cap2_index)*1000;


%-----------------------------------
% plot hqli vs time, cap gage vs time, select signal

figure(26)
f = plot(time3, cap3, '.b', time3, hqli3, '.r');
xlabel 'Time [s]'
ylabel 'Displacement [nm]'
title(['HQLI and Cap Gage vs. Time'])
xlim([0 xfit])
set(gcf, 'Position', get(0, 'Screensize'));
legend('Cap Gage', 'HQLI', 'Location', 'NorthEast');
grid on
hold on

% use Figure 9 to select the starting point for the up slope
%prompt = 'What is the starting time to select? ';
waitfor(msgbox('Select the starting point and stopping point on the first up
slope using the mouse'));
[x,y] = ginput(2);
t_start = x(1);
t_stop = x(2);

% Java code to minimize Figure
% https://undocumentedmatlab.com/matlab/wp-
content/cache/all/articles/minimize-maximize-figure-window/index.html
jFrame = get(handle(gcf),'JavaFrame');
jFrame.setMinimized(true);

T_DUT = 1/f_DUT; % period of wavelength
total3 = max(time3/T_DUT); % number of cycles

k = 1;
t_start = t_start;
t_stop = t_stop;
diff4 = [0];

for k = 1:total3

% values between t_start and t_stop
g1_index = find(time3 <= t_stop & time3 >= t_start);

time4 = time3(g1_index);
cap4 = cap3(g1_index);
hqli4 = hqli3(g1_index);

%-----------------------------------
% cap4 linear fit to subtract rotation
```

```
[xData2, yData2] = prepareCurveData( time4, cap4 );

% Set up fittype and options
ft2 = fittype( {'x', '1'}, 'independent', 'x', 'dependent', 'y',
'coefficients', {'a', 'b'} );

% Fit model to cap4
[fitresult2, gof] = fit( xData2, yData2, ft2 );

% % Plot fit with data
% figure(100 +(k-1));
% plot( fitresult2, xData2, yData2 );
% legend( 'cap4 vs. time4', 'fit 2', 'Location', 'NorthEast');
% xlabel 'time4';
% ylabel 'cap4';
% grid on
% hold on

a_2 = fitresult2.a;
b_2 = fitresult2.b;

cap4_fit = a_2*time4 + b_2; %fit of cap4

cap5 = cap4_fit - cap4;

% %-----------------------------------
% % plot difference vs time, complete dataset
% figure(800+k)
% plot(time4, cap5, 'k');
% xlabel 'Time [s]'
% ylabel 'Linear Diff [nm]'
% title(['Linear Diff vs. Time'])
% grid on
% hold on

%-----------------------------------
% hqli4 linear fit to subtract rotation
[xData3, yData3] = prepareCurveData( time4, hqli4 );

% Set up fittype and options
ft3 = fittype( {'x', '1'}, 'independent', 'x', 'dependent', 'y',
'coefficients', {'a', 'b'} );

% Fit model to cap4
[fitresult3, gof] = fit( xData3, yData3, ft3 );

% % Plot fit with data
% figure(200 + (k-1));
% plot( fitresult3, xData3, yData3 );
% legend( 'hqli4 vs. time4', 'fit 3', 'Location', 'NorthEast');
% xlabel 'time4';
% ylabel 'hqli4';
% grid on
% hold on

a_3 = fitresult3.a;
b_3 = fitresult3.b;
```

```
hqli4_fit = a_3*time4 + b_3; %fit of hqli4

hqli5 = hqli4_fit - hqli4;

diff2 = hqli5 - cap5; % error in the upslope

%*************************************************************
%*************************************************************

%-----------------------------------
% hqli5 polynomial fit to subtract u shape
[xData4, yData4] = prepareCurveData( time4, hqli5 );

% Set up fittype and options
ft4 = fittype( 'poly3' );

% Fit model to data
[fitresult4, gof] = fit( xData4, yData4, ft4);

% % Plot fit with data
% figure( 300 +(k-1) );
% h4 = plot( fitresult4, xData4, yData4 );
% legend( h4, 'hqli5 vs. time4', 'poly fit 3', 'Location', 'NorthEast',
'Interpreter', 'none' );
% xlabel 'time [s]';
% ylabel 'hqli5 [nm]';
% grid on
% hold on

p1_4 = fitresult4.p1;
p2_4 = fitresult4.p2;
p3_4 = fitresult4.p3;
p4_4 = fitresult4.p4;

% f(x) = p1*x^3 + p2*x^2 + p3*x + p4
% Plot hqli3_fit displacement using fit coefficients
hqli5_fit = p1_4*time4.^3 + p2_4*time4.^2 + p3_4*time4 + p4_4;

hqli6 = hqli5_fit - hqli5;

%-----------------------------------
% cap5 polynomial fit to subtract u shape
[xData5, yData5] = prepareCurveData( time4, cap5 );

% Set up fittype and options
ft5 = fittype( 'poly3' );

% Fit model to data
[fitresult5, gof] = fit( xData5, yData5, ft5);

% % Plot fit with data
% figure( 400 +(k-1) );
% h5 = plot( fitresult5, xData5, yData5 );
% legend( h5, 'cap5 vs. time4', 'poly fit 3', 'Location', 'NorthEast',
'Interpreter', 'none' );
% xlabel 'time [s]';
```

```
% ylabel 'cap5 [nm]';
% grid on
% hold on

p1_5 = fitresult5.p1;
p2_5 = fitresult5.p2;
p3_5 = fitresult5.p3;
p4_5 = fitresult5.p4;

% f(x) = p1*x^3 + p2*x^2 + p3*x + p4
% Plot cap5_fit displacement using fit coefficients
cap5_fit = p1_5*time4.^3 + p2_5*time4.^2 + p3_5*time4 + p4_5;

cap6 = cap5_fit - cap5;

diff3 = hqli6 - cap6; % error in the polynomial

%*********************************************************
%*********************************************************

if(total3 <= 10)  % this limits the number of graphs that will be shown

% %-----------------------------------
% % plot hqli vs time, cap gage vs time, select signal
% figure( 500 +(k-1))
% yyaxis left
% plot(time4, cap6, '.b', time4, hqli6, '.r');
% xlabel 'Time [s]'
% ylabel 'Displacement [nm]'
% set(gca,'ycolor','b')
% title(['HQLI and Cap Gage vs. Time'])
% yyaxis right
% plot(time4, diff3, '.k');
% ylabel 'Difference [nm]'
% set(gca,'ycolor','k')
% legend('Cap Gage', 'HQLI', 'Diff', 'Location', 'Southeast')
% grid on
% hold on

else

end

diff4 = [diff4 , diff3']; % total displacement error on all k's

t_start = t_start + T_DUT;
t_stop = t_stop + T_DUT;

end

diff4_rms = std(diff4) % rms deviation between cap gage and HQLI

%-----------------------------------
% plot difference vs time, complete dataset
figure(600+k)
plot(diff4, 'k');
xlabel 'Datapoint [-]'
```

```
ylabel 'HQLI Diff [nm]'
title(['HQLI Diff vs. Time'])
xlim([0 length(diff4)])
grid on
hold on

% %-----------------------------------
% % plot difference vs time, complete dataset
% figure(700+k)
% plot(time, diff1, 'k');
% xlabel 'Time [s]'
% ylabel 'HQLI Diff [nm]'
% title(['Diff1 vs. Time'])
% xlim([0 max(time)])
% grid on
% hold on



% important calculated system values
SN_min
FC_min
dx
diff4_rms %best estimate of error in system
sys_acc % current system accuracy

% % use these value for range testing
% SN_1
% SN_2
% FC_1
% FC_2

% write output csv file

if(savedata == 1)

output = ([time4, cap6, hqli6, diff4]);
%writematrix(output, filename);
csvwrite(filename, output);
else

end



msgbox('DATA ANALYSIS IS COMPLETE!');
```